Application of picosecond laser ablation to the production of colloidal gold nanoparticles

September 26, 2007

"Die Neigung des Menschen, kleine Dinge wichtig zu nehmen, hat sehr Großes hervorgebracht."

(The human tendency to regard little things as important has produced very many great things.)

Georg Christoph Lichtenberg (1742-1799)

Contents

Chapter 1

Introduction

1.1 Overview

> *"I would like to describe a field, in which little has been done, but in which an enormous amount can be done in principle. This field [...] is more like solid-state physics in the sense that it might tell us much of great interest about the strange phenomena that occur in complex situations. Furthermore, a point that is most important is that it would have an enormous number of technical applications."*
>
> Richard Phillips Feynman

These are the words that opened the speech of Richard P. Feynman on December 29th 1959 at the annual meeting of the American Physical Society at the California Institute of Technology (Caltech).

Nowadays, *nanotechnology, nanoscience, nanostructures, nanoparticles,* etc. are some of the most widely used terms in material science literature, nanotechnology representing a field of applied science and technology covering a broad range of topics. The main unifying theme is the control of matter on a scale smaller than 1 micrometer, normally approximately 1 to 100 nanometers, as well as the fabrication of devices of this size. It is a highly multidisciplinary field, drawing from fields such as applied physics, materials science, colloidal science, device physics, supramolecular chemistry, and even mechanical and electrical engineering. Nanotechnology can be seen as an extension of existing sciences into the nanoscale, or as a recasting of existing sciences using a newer, more modern term.

Among all nanomaterials, the nanoparticles are very attractive due to their physical and chemical properties and to their applications in a wide range of fields. In nature, nanoparticles are present almost everywhere and can be found as solids (all crystals are "nanocrystal" in their early existence), liquids (droplets) or gases (gas bubbles in nanoporous materials). Metal nanoparticles are of great interest because of their size- and shape-dependent properties. Among those, the nanoparticles made of noble metals like gold and silver started to be intensively studied in the last decades, because of their unique properties which make

a)  b) 

Figure 1.1: Lycurgus Cup (4th century AD) view: a) in reflected light, b) in transmitted light.

them useful for applications in several rapidly developing fields like photonics, information technology, cancer treatment and *in vivo* Ramam spectroscopy [1]. The unique optical properties of small metallic particles are exploited in the manufacturing of optical filters, labels for bio-macromolecules, in reversible photosensitive monochromatic glasses, for optical switching based on their large, ultrafast nonlinear optical response, and for optical trapping due to their high polarizability.

For the beauty and resilience of their color, since the time of the Romans, the metal nanoparticles (at that time known as gold powder) are used as decorative pigments. Maybe the most interesting and precious evidence of this use of the metal nanoparticles is the Lycurgus Cup[1] (Fig.1.1), famous for its unique feature of changing color depending on the light in which is viewed. The glass analysis reveled that it contains a small amount of $\sim 70nm$ metal crystals containing Ag and Au in a molar ratio of 14:1.

Even if their were used in stained glasses very early, the first systematic study of the synthesis and colors of colloidal gold was done only in 1857 by Michael Faraday[2]. He attributed the beautiful reds, burgundy, or purples colors of the stained-glasses to the presence of "very finely divided dispersed gold" (known today as gold nanoparticles). Since then thousands of scientific papers have been published on the synthesis, modification, properties, and assembly of metal nanoparticles, all this leading not only to reliable procedures for the preparation of metal nanoparticles of any desired size and shape, but also to the understanding of many of their physico-chemical features.

Modifying the size or shape of the nanoparticles results in a change of their color. This effect is due to the occurrence of the surface plasmon resonance [96, 4], the frequency at which conduction electrons oscillate in response to the alternating electric field of incident electromagnetic radiation. The plasmon resonance in the visible part of the spectrum is the reason for the intense color of noble and alkali metals; gold nanospheres have a

[1] In present at the British Museum, London, England.

characteristic red color, while silver nanospheres are yellow, differing from the characteristic colors of these metals in bulk form. This is a first evidence that the properties of the nanoscale materials are different from those of the bulk.

The surface plasmon resonance was first calculated by G. Mie [93] solving the Maxwell's equations for small spheres interacting with an electromagnetic field. Later, R. Gans [6] extended this theory to ellipsoidal geometries, and now modern methods using discrete dipol approximations allow one to calculate the surface plasmon resonance absorption for arbitrary geometries [7].

Many different techniques have been developed for the synthesis of metal nanoparticles, the most widely used being based on chemical reactions in solutions that yield colloids of metal nanoparticles. These techniques usually employ a chemical agent to stop the growth of the particles at the nanoscale, and capping materials, such as surfactants, polymers or dendrimers, are used to prevent aggregation and precipitation of the metal nanoparticles.

The size and shape of the nanoparticles is determined by the choice of the reduction technique, time, and capping material. In this way, spheres, rods, cubes, disks, wires, tubes, branched, triangular prisms, and tetrahedral nanoparticles have been synthesized in gold, silver and platinum.

Spherical colloidal gold nanoparticles are commonly produced by citrate reduction method[9], reported by Turkevitch in 1951, in which gold salt and citrate are stirred in water while the temperature, the ratio of gold to citrate, and the order of addition of the reagents control the size distribution of generated gold nanospheres. Other popular methods are the seeding technique, which produces large spherical and non-spherical nanoparticles, the two-phase reaction and the inverse micelle technique, both using surfactants to produce small size nanoparticles with narrow dispersity.

The volumes of synthesis are typically small and the resulting particles are slightly different at every run. Chemically produced gold and silver nanoparticles are commercially available preconjugated and conjugated with popular analytes, but the samples vary from batch to batch and could be contaminated from chemicals used in the synthetic procedure. Moreover, the choice of the solvent and surface chemistry often reduces the number of possible synthetic techniques for the process under study.

The above listed difficulties are the reasons that determined the efforts of scientists to search for an alternative method to produce colloidal nanoparticles free from by-products (impurities) of chemical reactions. The use of pulsed laser ablation could be such an alternative method since it has a great flexibility in the use of materials and solvents, it is less time consuming, and above all has the advantage of producing nanoparticles free from by-products of chemical reactions.

The aqueous colloidal solution of nanoparticles has many advantages like:

- the possibility of easily varying the mean cluster size between 1 and more than 100nm;
- the possibility of changing the positions of clusters by evaporation;

- it can be produced quantities of cluster matter up to the gram scale;
- these systems can be easily stabilized;
- percolation structures can be created by coagulation and/or coalescence;
- the liquid samples can be transformed into solid;
- the cluster surfaces can be manipulated chemically and cluster-shell particles can be produced.

At present, the research in the field of nanotechnology, specially for chemistry and physics of nanoscale materials need aqueous solutions of colloidal nanoparticles with high purity, precise shapes, size and narrow size-distribution, and size-selected nanoparticles with diameters less than 10nm in solution.

1.2 Previous and related works

Nanosized particles have been subjected to extensive research since the 1980s and ten years later the laser ablation started to be employed for the preparation of colloidal nanoparticles by ablation of thin metal films or of suspended micrometer-sized particles in a solvent [10]. In the following is presented a short review of the activity and the results of the more active groups.

In the early works of Henglein [11] and Cotton et al.[12] is presented the production of nickel, carbon and noble metal nanoparticles in water and solvents like propanol and hexane. The lasers employed in the target ablation were respectively a millisecond pulsed ruby laser at 694nm and a nanosecond Nd:YAG laser at 1064nm.

Their work on producing "chemically pure" metallic colloids was continued by Stepanek et al. (1997-1998). They demonstrated the size reduction effect induced by the presence of the ion Cl^- [13], and by the use of picosecond laser pulses [15]. Moreover, they remarked the absorption of incident laser light by the colloidal particles (self-absorption) and its effect on the size of large colloidal nanoparticles, the self-absorption being found to be the key for optimization of particles size-distribution.

Furthermore the researchers investigated the influence of laser parameters to control the size and shape of the nanoparticles. Kondow et al.[20, 21] studied the use of a laser wavelength resonant with the nanoparticles plasmon band for their size reduction and reshaping, and the growth of gold clusters into nanoparticles following laser-induced fragmentation [22].

In the attempt to ascertain the mechanism of colloids formation by laser ablation, thus far, some researchers have investigated the influence of the ablation parameters on the ablation efficiency and the size of the nanoparticles. Among them, Tsuji et al. investigated on the laser wavelength influence on the particle size [17] and on the ablation efficiency [16].

Mafune et al.[18] reported the colloid formation mechanism in aqueous solution of sodium dodecylsulfate (SDS), the influence of the laser fluence and of the number of laser shots [19] on the ablation efficiency and on the particle size, together with the effect of SDS on the colloids growing process.

Lately, Meunier et al. investigate on the nanoparticles production using femtosecond laser radiation and they succeeded in synthesizing in aqueous solution of cyclodextrines, nanoparticles with mean diameters of 3.5nm and 2.5nm. They mentioned on the influence of the solvent pH on the size of the nanoparticles.

Due to the fact that laser ablation in organic solvents seems to overtake at least in part the problems of chemical reduction, and due to the need of organic solvents for the one step functionalization of the gold nanoparticles to be used in biomedical applications, the interest in producing nanoparticles in organic solvents is increasing. Lately, Amendola et al.[25] reported the production of spherical gold nanoparticles by laser ablation in dimethylsulfoxide, tetrahydrofuran, and acetonitrile, solvents largely used in organic chemistry, and also reported the production of core-shell (gold-graphite) nanoparticles by laser ablation of a gold target in toluene [26].

Compagnini et al. initiated the laser ablation synthesis of gold nanoparticles in liquids different from water (alkanes and thiol-alkanes solutions). They showed the laser induced reactivity features of some of these liquids (specially chlorinated liquids) leading to the formation of compounds [23], and the size reduction effect of the thiols molecules [24].

Bio-compatible nanomaterials are presently of great interest as well as metal-organic nanomaterials. In the last years, due to their biocompatibility and tailor-made properties the use of dendrimers as templates for nanoparticles formation was, and continue to be, extensively investigated [27, 28]. Some results have been already reported by Esumi et al. which synthesized, by chemical reduction, metal-dendrimer nanocomposites for gold, platinum and silver [30]. They have shown the effective protective action of poly(amidoamine) dendrimers for the preparation of the nanoparticles [29], and demonstrated the dendrimer concentration, necessary for an effective protection of the nanoparticles, to depend on the interaction between the metal particles and the external functional groups of the dendrimer. Balog et al. [32] emphasized the role of the gold nanocomposites in cells imaging owing to their well defined size and shape, and to their increased contrast which give them a great potential for biomedical applications [31].

1.3 Objectives and results of this thesis

The increasing interest for colloidal nanoparticles and metal-organic nanomaterials, and the advantages that the production of nanoparticles by laser ablation has on the chemical reduction methods (especially in organic solvents), stimulated us to investigate the production of gold nanoparticles by laser ablation of a solid gold taget in different liquids.

Since the previous works have observed a dependence of the ablation mechanism on the length of the laser pulse, and only a few works [15] report results obtained by using

picosecond laser ablation, our first purpose was to investigate the production of colloidal nanoparticles by picosecond laser ablation in water.

The first experiments, done in doubly deionized water, served as guide experiments to give us the first insights in the laser ablation of a solid target in liquid environment and in the formation mechanism and stability of gold nanoparticles produced in water. They confirmed the instability of the free gold nanoparticles in water and their tendency to form large aggregates with dendritic structures (especially when the 532nm is used). Also, the first indications of a different ablation mechanism of 532nm and 1064nm laser wavelengths were obtained.

The second purpose was to investigate the production of nanoparticles in the presence of a stabilizer. First we used the sodium dodecyl sulfate (SDS) and then the biocompatible generation five poly(amidoamine) dendrimer (PAMAM G5).

The used of sodium dodecyl sulfate (SDS) as surfactant, allowed us to obtain stable gold nanoparticles having a mean diameter of only 2.6nm and a narrow size distribution. The measurements of on-line transmission at 514.5nm for the laser ablation in aqueous solution of SDS confirmed the existence of two different mechanisms for the production of the nanoparticles depending on the laser wavelength, and revealed the temperature influence on the process of nanoparticles production.

Stable gold nanoparticles were produced and metal-dendrimer nanocomposites (DNC) were found to be formed by laser ablation of a solid gold target in aqueous solutions of PAMAM G5.

The ablation mechanism and the subsequent formation of gold nanoparticles was found to depend on the laser wavelength. The results allowed us to state the mechanism of action for both laser wavelengths, 1064nm and 532nm. The known size reduction effect of the 532nm radiation has been investigated and it has been shown that the photo-fragmentation of PAMAM G5-capped-gold nanoparticles is due to the multiphoton absorption of the 532nm radiation and to lead to the formation of metal-dendrimer nanocomposite (DNC) between gold cations and dendrimer.

The formation of DNC allowed the use of the spectroscopic monitoring of the charged metal clusters. In this way it was possible to observed a degradation mechanism of the nanoparticles, similar to that of the 532nm, by exposing PAMAM G5 stabilized suspensions of gold nanoparticles in water to the low power UV radiation of a mercury lamp emitting at 254nm. By spectroscopic monitoring of the DNC formation we could investigate the workfunction of the PAMAM G5-capped-gold nanoparticles and to locate it below 4.6eV.

The last purpose of this thesis was to study the nanoparticles production in organic liquids. For now some important results were obtained in the case of toluene, chloroform and diethyl ether but further work is still to be done. It was also started the work to the production and functionalization of gold nanoparticles with polymer molecules in a one-step process.

1.4 Structure of the thesis

This thesis approach the production of spherical gold nanoparticles by laser ablation of a solid target in liquid environment.

Chapter 2 presents the theoretical aspects of the optics of metallic nanoparticles. Section 2.1 describes Mie's theory on the diffraction of light by a sphere. The features of plasmon resonances, as function of the nanoparticles and the environment dielectric constant, and of the shape, size and size-distribution of the nanoparticles are described in Section 2.2.

Chapter 3, Section 3.1, describes the pulsed laser ablation process and its characteristics determined by laser parameters and by the properties of the environment. The formation mechanism and the growth of nanoparticles by the chemical reduction is presented in Section 3.2 and a short description of the nanoparticles formation during the pulsed laser ablation of a solid target in liquid environment is given in Section 3.3.

In Chapter 4 are presented the chemical and physical approaches for the size and shape control of the nanoparticles. Section 4.1 presents the action of sodium dodecyl sulphate as chemical size reduction tool in the mechanism of the nanoparticles formation and the ability of dendrimers to protect the nanoparticles from aggregation and to form dendrimer nanocomposites. In Section 4.2 is presented the mechanism of size reduction of the nanoparticles using the laser light.

Chapter 5 describes our experiments and the results obtained until now. Sections 5.2 and 5.3 describe the results in the production of gold nanoparticles by picosecond laser ablation in water and SDS respectively and the preliminary features of the ablation mechanism. A detailed description of the ablation mechanism, together with the results on the DNC formation, is given in Section 5.4, that presents our results for the production of nanoparticles in aqueous solution of PAMAM G5. Finally, in Section 5.5 are presented the preliminary results obtained for the production of nanoparticles in three organic solvents.

The last chapter provides a summary of the conclusions reached in these studies, together with suggestions for further studies on the addressed problems.

Chapter 2

Optics of Metallic Nanoparticles

2.1 Diffraction of light by a sphere - Mie's theory

The study of aqueous colloidal solutions of gold particles initiated with Faraday (1857), who studied the changes of the color of the colloidal solution depending on the state of polarization of the gold matter.

Some of the optical features of metallic particles were explained by Maxwell Garnet (1904), who studied the propagation of light through a dielectric medium containing many small metallic spheres in a volume whose linear dimensions was that of a wavelength. He showed that such an assembly is equivalent to a medium of a certain complex refraction index $\hat{n} = n'(1 - ik')$ and found formulas for n' and k' in terms of the indices n and k that characterize the metallic spheres.

A rigorous solution for the diffraction of a plane monochromatic wave by a homogeneous sphere of arbitrary diameter and composition situated in a homogeneous medium was obtained in 1908 by G. Mie [93] using the electromagnetic theory. Shortly afterwards, an equivalent solution for the same problem was published by P. Debye in a paper concerned with light pressure on a conducting sphere.

The work of Mie was later extended to be applied to other shapes which better correspond to the shapes of real particles. One of these extensions was developed by R.Gans (1915) for the diffraction of light on prolate and oblate ellipsoids.

The Mie solution is derived for diffraction by a single sphere but it can be also applied to diffraction by any number of spheres which all have the same diameter and composition, are randomly distributed and separated from each other by distances that are large compared to the wavelength.

The method employed by Mie in deriving its formulas starts with finding the solution of Maxwell's equations which describe the field of a plane monochromatic wave incident upon a spherical surface, across which the medium properties abruptly change. He used a curvilinear coordinates system in which the field is represented as the sum of two subfields. One of the subfields is such that its electric vector has no radial component while the other has the magnetic vector without radial component. Maxwell's equations, together with

the boundary conditions, separate into a set of ordinary differential equations, which are solved for the two subfields in the form of series.

2.1.1 The solution of Mie [36]

In his theory [93], Mie starts considering a plane, monochromatic and linearly polarized wave incident on a metallic sphere of radius a embedded in a nonconductor, homogeneous and isotropic medium. Both the sphere and the medium are considered non-magnetic.

Writing the Maxwell's equations :

$$curl\,\mathbf{H} - \frac{1}{c}\dot{\mathbf{D}} = \frac{4\pi}{c}\mathbf{j} \tag{2.1}$$

$$curl\,\mathbf{E} + \frac{1}{c}\dot{\mathbf{B}} = 0 \tag{2.2}$$

$$div\,\mathbf{D} = 4\pi\rho \tag{2.3}$$

$$div\,\mathbf{B} = 0 \tag{2.4}$$

(where $\mathbf{H}$ and $\mathbf{E}$ are the magnetic and respectively the electric vector, $\mathbf{D}$ is the electric displacement, $\mathbf{B}$is the magnetic induction, and the dot denotes the differentiation with respect to the time) and assuming the time dependence $\exp(-i\omega t)$ for the electromagnetic field, the time-independent parts of the electric and magnetic vectors, both inside and outside the sphere, will satisfy the time-independent form of Maxwell's equations:

$$curl\,\mathbf{H} = -k_1\mathbf{E} \tag{2.5}$$

$$curl\,\mathbf{E} = -k_2\mathbf{H} \tag{2.6}$$

where

$$k_1 = \frac{i\omega}{c}(\varepsilon + i\frac{4\pi\sigma}{\omega}) \tag{2.7}$$

$$k_2 = \frac{i\omega}{c} \tag{2.8}$$

$$k^2 = -k_1 k_2 \tag{2.9}$$

k being the wave number (real outside and complex inside the sphere). With a non-conducting medium outside the sphere we will have a specific conductivity $\sigma^{(I)} = 0$ (the superscript I denotes the quantities outside the sphere and II, used in the following, those inside the sphere).

The system of coordinates (see fig.2.1) has the origin at the center of the sphere, the z direction is in the direction of propagation of the wave, and the x direction is in the direction of its electric vector. If the amplitude of the electric vector of the incident wave

is normalized to the unit, i.e. $\left|\mathbf{E}^{(i)}\right| = \left|e^{ik^{(I)}z}\right| = 1$, (i denotes the incident field, s the scattered field, and w the field within the sphere) the six components of the incident field vectors are:

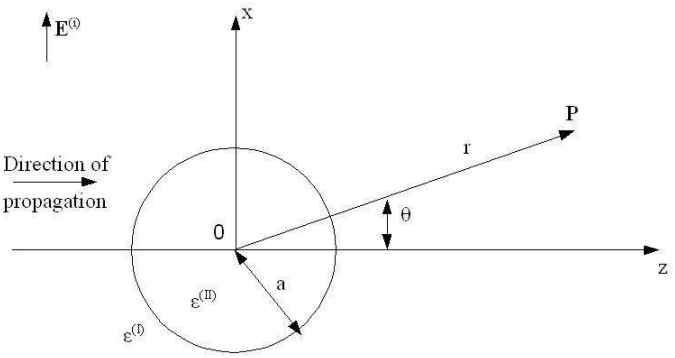

Figure 2.1: The system of coordinates.

$$E_x^{(i)} = e^{ik^{(I)}z} \tag{2.10}$$

$$H_y^{(i)} = \frac{ik^{(I)}}{k_2^{(I)}} e^{ik^{(I)}z} \tag{2.11}$$

$$E_y^{(i)} = E_z^{(i)} = H_x^{(i)} = H_z^{(i)} = 0. \tag{2.12}$$

Across the sphere surface we have a discontinuity, and then the boundary conditions impose that the tangential components of $\mathbf{E}$ and $\mathbf{H}$ shall be continuous across the sphere surface (when $r = a$):

$$\begin{cases} E_{tang}^{(I)} = E_{tang}^{(II)} \\ H_{tang}^{(I)} = H_{tang}^{(II)}. \end{cases} \tag{2.13}$$

From the boundary conditions and the Maxwell's equations, it follows that the radial components of $\varepsilon\mathbf{E}$ and $\mathbf{H}$ shall also be continuous across the sphere surface.

The total electric field outside the sphere and within the sphere is:

$$\mathbf{E} = \begin{cases} \mathbf{E}^{(I)} = \mathbf{E}^{(i)} + \mathbf{E}^{(s)} & \textit{outside the sphere}, \\ \mathbf{E}^{(II)} & \textit{within the sphere}. \end{cases} \tag{2.14}$$

There are similar expressions for the magnetic vector. The fields $\mathbf{E}^{(I)}$, $\mathbf{H}^{(I)}$ are the fields outside the sphere, $\mathbf{E}^{(i)}$, $\mathbf{H}^{(i)}$ are the incident fields, $\mathbf{E}^{(s)}$, $\mathbf{H}^{(s)}$ are the fields scattered by the sphere, and $\mathbf{E}^{(II)}$, $\mathbf{H}^{(II)}$ represent the fields within the sphere.

The most appropriate system of coordinates to solve the present problem is the system

of spherical polar coordinates (r, θ, φ):

$$\begin{cases} x = r\sin\theta\cos\varphi \\ y = r\sin\theta\sin\varphi \\ z = r\cos\theta \quad . \end{cases} \tag{2.15}$$

The field equations (2.5) and (2.6) in this system of coordinates become:

$$\begin{cases} -k_1 E_r = \frac{1}{r^2\sin\theta}\left[\frac{\partial(rH_\phi\sin\theta)}{\partial\theta} - \frac{\partial(rH_\theta)}{\partial\phi}\right] \\ -k_1 E_\theta = \frac{1}{r\sin\theta}\left[\frac{\partial H_r}{\partial\phi} - \frac{\partial(rH_\phi\sin\theta)}{\partial r}\right] \\ -k_1 E_\phi = \frac{1}{r}\left[\frac{\partial(rH_\theta)}{\partial r} - \frac{\partial H_r}{\partial\theta}\right] \quad , \end{cases} \tag{2.16}$$

$$\begin{cases} k_2 H_r = \frac{1}{r^2\sin\theta}\left[\frac{\partial(rE_\phi\sin\theta)}{\partial\theta} - \frac{\partial(rE_\theta)}{\partial\phi}\right] \\ k_2 H_\theta = \frac{1}{r\sin\theta}\left[\frac{\partial E_r}{\partial\phi} - \frac{\partial(rE_\phi\sin\theta)}{\partial r}\right] \\ k_2 H_\phi = \frac{1}{r}\left[\frac{\partial(rE_\theta)}{\partial r} - \frac{\partial E_r}{\partial\theta}\right] \quad , \end{cases} \tag{2.17}$$

and the boundary conditions (2.13) are:

$$\left.\begin{array}{ll} E_\theta^{(I)} = E_\theta^{(II)}, & E_\phi^{(I)} = E_\phi^{(II)} \\ H_\theta^{(I)} = H_\theta^{(II)}, & H_\phi^{(I)} = H_\phi^{(II)} \end{array}\right\} \quad for \quad r = a. \tag{2.18}$$

As mentioned before, the solutions of (2.16) and (2.17) with the boundary conditions specified in (2.18) are represented as the sum of two partial fields: $({}^e\mathbf{E}, {}^e\mathbf{H})$ and $({}^m\mathbf{E}, {}^m\mathbf{H})$ each satisfying (2.16) and (2.17) such that :

$${}^e\mathrm{E_r} = \mathrm{E_r}, \quad {}^eH_r = 0, \quad (the \quad electric\, wave) \quad , \tag{2.19}$$

$${}^m\mathrm{E_r} = 0, \quad {}^mH_r = H_r, \quad (the \quad magnetic\, wave). \tag{2.20}$$

From the first equation of (2.17), because ${}^eH_r = 0$, it follows that ${}^eE_\phi$ and ${}^eE_\theta$ may be represented in terms of a gradient of a scalar [36]:

$${}^eE_\phi = \frac{1}{r\sin\theta}\frac{\partial U}{\partial\phi}, \qquad {}^eE_\theta = \frac{1}{r}\frac{\partial U}{\partial\theta} \quad . \tag{2.21}$$

If U is written as:

$$U = \frac{\partial\,(r^e\Pi)}{\partial r}, \tag{2.22}$$

then

$$ {}^{e}E_{\phi} = \frac{1}{r\sin\theta}\frac{\partial^2 (r\,{}^{e}\Pi)}{\partial r \partial \phi}, \qquad {}^{e}E_{\theta} = \frac{1}{r}\frac{\partial^2 (r\,{}^{e}\Pi)}{\partial r \partial \theta}, \tag{2.23} $$

and the radial component, ${}^{e}E_r$, will be:

$$ {}^{e}E_r = \frac{\partial^2 (r\,{}^{e}\Pi)}{\partial r^2} + k^2 r\,{}^{e}\Pi. \tag{2.24} $$

The magnetic wave can be considered in a similar way and it results that the two waves, the electric wave and the magnetic wave, may each be derived from a scalar potential ${}^{e}\Pi$ and ${}^{m}\Pi$ respectively, known as Debye's potentials.

Both, ${}^{e}\Pi$ and ${}^{m}\Pi$ satisfy the wave equation:

$$ \nabla^2 \Pi + k^2 \Pi = 0. \tag{2.25} $$

The components of $({}^{e}\mathbf{E},\ {}^{e}\mathbf{H})$, derived from the ${}^{e}\Pi$ potential, may be written as:

$$ \begin{cases} {}^{e}E_r = \frac{\partial (r\,{}^{e}\Pi)}{\partial r^2} + k^2 r\,{}^{e}\Pi \\ {}^{e}E_{\theta} = \frac{1}{r}\frac{\partial^2 (r\,{}^{e}\Pi)}{\partial r \partial \theta} \\ {}^{e}E_{\phi} = \frac{1}{r\sin\theta}\frac{\partial^2 (r\,{}^{e}\Pi)}{\partial r \partial \phi} \\ {}^{e}H_r = 0 \\ {}^{e}H_{\theta} = -\frac{k_1}{r\sin\theta}\frac{\partial (r\,{}^{e}\Pi)}{\partial \phi} \\ {}^{e}H_{\phi} = \frac{k_1}{r}\frac{\partial (r\,{}^{e}\Pi}{\partial \phi} \end{cases} \tag{2.26} $$

We have similar expressions for the components of $({}^{m}\mathbf{E},\ {}^{m}\mathbf{H})$, derived from the ${}^{m}\Pi$.

The complete solution of our problem is:

$$ \begin{cases} E_r = {}^{e}E_r + {}^{m}E_r = \frac{\partial^2 (r\,{}^{e}\Pi)}{\partial r^2} + k^2 r\,{}^{e}\Pi \\ E_{\theta} = {}^{e}E_{\theta} + {}^{m}E_{\theta} = \frac{1}{r}\frac{\partial^2 (r\,{}^{e}\Pi)}{\partial r \partial \theta} + \frac{k_2}{r\sin\theta}\frac{\partial (r\,{}^{m}\Pi)}{\partial \phi} \\ E_{\phi} = {}^{e}E_{\phi} + {}^{m}E_{\phi} = \frac{1}{r\sin\theta}\frac{\partial^2 (r\,{}^{e}\Pi)}{\partial r \partial \phi} - \frac{k_2}{r}\frac{\partial (r\,{}^{m}\Pi)}{\partial \phi} \\ H_r = {}^{m}H_r + {}^{e}H_r = k^2 r\,{}^{m}\Pi + \frac{\partial^2 (r\,{}^{m}\Pi)}{\partial r^2} \\ H_{\theta} = {}^{m}H_{\theta} + {}^{e}H_{\theta} = \frac{1}{r}\frac{\partial^2 (r\,{}^{m}\Pi)}{\partial r \partial \theta} - \frac{k_1}{r\sin\theta}\frac{\partial (r\,{}^{e}\Pi)}{\partial \phi} \\ H_{\phi} = {}^{m}H_{\phi} + {}^{e}H_{\phi} = \frac{1}{r\sin\theta}\frac{\partial^2 (r\,{}^{m}\Pi)}{\partial r \partial \phi} + \frac{k_1}{r}\frac{\partial (r\,{}^{e}\Pi)}{\partial \theta} \end{cases} \tag{2.27} $$

and for the boundary conditions (2.13) to be satisfied over the spherical surface $r = a$, it will be sufficient for the quantities

$$ k_1 r\,{}^{e}\Pi, \quad k_2 r\,{}^{m}\Pi, \quad \frac{\partial}{\partial r}(r\,{}^{e}\Pi), \quad \frac{\partial}{\partial r}(r\,{}^{m}\Pi) \tag{2.28} $$

to be continuous over this surface.

The Debye's potentials are written in the form

$$\Pi = R(r)\Theta(\theta)\Phi(\phi). \tag{2.29}$$

For Π to satisfy the wave equation (2.25), R, Θ and Φ have to verify the following ordinary differential equations:

$$\begin{cases} \frac{d^2(r\mathbf{R})}{dr^2} + (k^2 - \frac{\alpha}{r^2})rR = 0 \\ \frac{1}{\sin\theta}\frac{d}{d\theta}(\sin\theta\frac{d\Theta}{d\theta}) + (\alpha - \frac{\beta}{\sin^2\theta})\Theta = 0 \\ \frac{d^2\Phi}{d\phi^2} + \beta\Phi = 0 \end{cases} \tag{2.30}$$

where α and β are integration constants.

Solving these equations, the general solution of the wave equation (2.25) will be:

$$\begin{cases} r\Pi = r\sum_{l=0}^{\infty}\sum_{m=-l}^{l}\Pi_l^{(m)} \\ \quad = \sum_{l=0}^{\infty}\sum_{m=-l}^{l}\left[c_l\Psi_l(kr) + d_l\chi_l(kr)\right]\left[P_l^{(m)}(\cos\theta)\right]\left[a_m\cos(m\phi) + b_m\sin(m\phi)\right] \end{cases} \tag{2.31}$$

where :

$a_m,\ b_m,\ c_l,\ d_l$ *are arbitrary constants*

$P_l^{(m)}(\cos\theta)$ *is the Legendre function*

$\Psi_l(kr) = \sqrt{\frac{\pi kr}{2}}J_{l+\frac{1}{2}}(kr)$

$J_{l+\frac{1}{2}}(kr)$ *is the Bessel function*

$\chi_l(kr) = -\sqrt{\frac{\pi kr}{2}}N_{l+\frac{1}{2}}(kr)$

$N_{l+\frac{1}{2}}(kr)$ *is the Neumann function*

After further mathematical calculations, the expressions of the potentials ${}^e\Pi$ and ${}^m\Pi$ become:

$$\begin{cases} r\,{}^e\Pi = \frac{1}{k^{(i)2}}\sum_{l=1}^{\infty} i^{l-1}\frac{2l+1}{l(l+1)}\Psi_l(k^{(I)}r)P_l^{(1)}(\cos\theta)\cos\phi \\ r\,{}^m\Pi^{(i)} = \frac{1}{k^{(i)2}}\sum_{l=1}^{\infty} i^{l}\frac{k^{(I)}}{k_2^{(I)}}\frac{2l+1}{l(l+1)}\Psi_l(k^{(I)}r)P_l^{(1)}(\cos\theta)\sin\phi \end{cases} \quad \textit{the incident wave,} \tag{2.32}$$

$$\begin{cases} r\,{}^{e}\Pi^{(w)} = \frac{1}{k^{(iI)2}} \sum_{l=1}^{\infty} {}^{e}A_l \Psi_l(k^{(II)}r) P_l^{(1)}(\cos\theta)\cos\phi \\ r\,{}^{m}\Pi^{(w)} = \frac{i}{k^{(iI)}k_2^{(iI)}} \sum_{l=1}^{\infty} {}^{m}A_l \Psi_l(k^{(II)}r) P_l^{(1)}(\cos\theta)\sin\phi \end{cases} \quad \textit{the wave in the sphere,} \tag{2.33}$$

$$\begin{cases} r\,{}^{e}\Pi^{(s)} = \frac{1}{k^{(i)2}} \sum_{l=1}^{\infty} {}^{e}B_l \zeta_l^{(1)}(k^{(I)}r) P_l^{(1)}(\cos\theta)\cos\phi \\ r\,{}^{m}\Pi^{(s)} = \frac{i}{k^{(i)}k_2^{(i)}} \sum_{l=1}^{\infty} {}^{m}B_l \zeta_l^{(1)}(k^{(I)}r) P_l^{(1)}(\cos\theta)\sin\phi \end{cases} \quad \textit{the scattered wave.} \tag{2.34}$$

By substituting (2.32), (2.33) and (2.34) into the boundary conditions (2.28), we obtain the linear relations between the coefficients ${}^{e}A_l$, ${}^{m}A_l$, ${}^{e}B_l$, ${}^{m}B_l$. Finding ${}^{e}B_l$, ${}^{m}B_l$ and introducing (2.34) in (2.27), the components of the field vectors of the scattered wave become[1]:

$$\begin{cases} E_r^{(s)} = \frac{1}{k^{(i)2}} \frac{\cos\phi}{r^2} \sum_{l=1}^{\infty} l(l+1)\, {}^{e}B_l \zeta_l^{(1)}(k^{(I)}r) P_l^{(1)}(\cos\theta) \\ E_\theta^{(s)} = -\frac{1}{k^{(i)}} \frac{\cos\phi}{r} \sum_{l=1}^{\infty} \Big[{}^{e}B_l \zeta_l^{(1)\prime}(k^{(I)}r) P_l^{(1)\prime}(\cos\theta)\sin\theta \\ \qquad -i\,{}^{m}B_l \zeta_l^{(1)}(k^{(I)}r) P_l^{(1)\prime}(\cos\theta)\sin\theta \Big] \\ E_\phi^{(s)} = -\frac{1}{k^{(i)}} \frac{\sin\phi}{r} \sum_{l=1}^{\infty} \Big[{}^{e}B_l \zeta_l^{(1)\prime}(k^{(I)}r) P_l^{(1)}(\cos\theta) \frac{1}{\sin\theta} \\ \qquad -i\,{}^{m}B_l \zeta_l^{(1)}(k^{(I)}r) P_l^{(1)\prime}(\cos\theta)\sin\theta \Big] \\ H_r^{(s)} = \frac{1}{k^{(I}k_2^{(i)}} \frac{\sin\phi}{r^2} \sum_{l=1}^{\infty} l(l+1)\, {}^{m}B_l \zeta_l^{(1)}(k^{(I)}r) P_l^{(1)}(\cos\theta) \\ H_\theta^{(s)} = -\frac{1}{k_2^{(i)}} \frac{\sin\phi}{r} \sum_{l=1}^{\infty} \Big[{}^{e}B_l \zeta_l^{(1)}(k^{(I)}r) P_l^{(1)}(\cos\theta) \frac{1}{\sin\theta} \\ \qquad +i\,{}^{m}B_l \zeta_l^{(1)\prime}(k^{(I)}r) P_l^{(1)\prime}(\cos\theta)\sin\theta \Big] \\ H_\phi^{(s)} = -\frac{1}{k_2^{(i)}} \frac{\cos\phi}{r} \sum_{l=1}^{\infty} \Big[{}^{e}B_l \zeta_l^{(1)}(k^{(I)}r) P_l^{(1)\prime}(\cos\theta)\sin\theta \\ \qquad +i\,{}^{m}B_l \zeta_l^{(1)\prime}(k^{(I)}r) P_l^{(1)}(\cos\theta) \frac{1}{\sin\theta} \Big] \end{cases} \tag{2.35}$$

where:

$$\left.\begin{aligned} \zeta_l^{(1)} &= (\Psi_l - i\chi_l) \\ {}^{e}B_l &= i^{l+1} \frac{2l+1}{l(l+1)} \frac{k_2^{(I)} k^{(II)} \Psi_l'(k^{(I)}a)\Psi_l(k^{(II)}a) - k_2^{(II)} k^{(I)} \Psi_l'(k^{(II)}a)\Psi_l(k^{(I)}a)}{k_2^{(I)} k^{(II)} \zeta_1^{(1)\prime}(k^{(I)}a)\Psi_l(k^{(II)}a) - k_2^{(II)} k^{(I)} \Psi_l'(k^{(II)}a)\zeta_1^{(1)}(k^{(I)}a)} \\ {}^{m}B_l &= i^{l+1} \frac{2l+1}{l(l+1)} \frac{k_2^{(I)} k^{(II)} \Psi_l(k^{(I)}a)\Psi_l'(k^{(II)}a) - k_2^{(II)} k^{(I)} \Psi_l'(k^{(I)}a)\Psi_l(k^{(II)}a)}{k_2^{(I)} k^{(II)} \zeta_1^{(1)}(k^{(I)}a)\Psi_l'(k^{(II)}a) - k_2^{(II)} k^{(I)} \zeta_l^{(1)\prime}(k^{(I)}a)\Psi_l(k^{(II)}a)} \end{aligned}\right\} \tag{2.36}$$

The wave number outside and inside the sphere will be:

[1] The addition of a prime to the functions $P_l^{(1)\prime}$, $\Psi_l'$and $\zeta_l^{(1)\prime}$ denotes differentiation with respect to their arguments.

$$k^{(I)} = \sqrt{-k_1^{(I)} k_2^{(I)}} = \frac{2\pi}{\lambda_0}\sqrt{\varepsilon^{(I)}} = \frac{2\pi}{\lambda^{(I)}} \qquad \begin{cases} k_1^{(I)} = i\frac{2\pi}{\lambda_0}\varepsilon^{(I)} \\ k_2^{(I)} = i\frac{2\pi}{\lambda_0} \\ k_1^{(II)} = i\frac{2\pi}{\lambda_0}\left(\varepsilon^{(II)} + i\frac{4\pi\sigma}{\omega}\right) \\ k_2^{(II)} = i\frac{2\pi}{\lambda_0} \end{cases}$$

$$k^{(II)} = \sqrt{-k_1^{(II)} k_2^{(II)}} = \frac{2\pi}{\lambda_0}\sqrt{\varepsilon^{(II)} + \frac{4\pi\sigma}{\omega}} \qquad (2.37)$$

where λ_0 is the wavelength of the light in vacuum, $\lambda^{(I)}$ is the wavelength in the medium surrounding the sphere, and σ is the $\sigma^{(II)}$.

The complex refraction index of the sphere, $\hat{n}$, relative to the surrounding medium will be:

$$\hat{n}^2 = \frac{\hat{n}^{(II)2}}{\hat{n}^{(I)2}} = \frac{k^{(II)2}}{k^{(I)2}} = \frac{\varepsilon^{(II)}}{\varepsilon^{(I)}} + i\frac{4\pi\sigma}{\omega\varepsilon^{(I)}} = \frac{k_1^{(II)}}{k_1^{(I)}}. \qquad (2.38)$$

2.1.2 Consequences of Mie's formula

From the Mie's formulae, (2.34), it can be seen that the amplitude of the radial components $E_r^{(s)}$and $H_r^{(s)}$ of the scattered wave fall off as the inverse square of the distance from the scattering centre (the sphere) $\frac{1}{r^2}$, whereas the amplitude of the other components fall off more slowly ($\frac{1}{r}$). Therefore, at great distances from the sphere ($r \gg \lambda$), the radial components can be neglected in comparison with the tangential ones so that in this region the scattered wave is transverse.

The formulae (2.34) also show that the scattered wave is composed by contributions of spherical harmonics of different orders (l), called *partial waves*. Their strength is determined by the absolute values of the complex coefficients ${}^eB_l$ and ${}^mB_l$ which depend on the nature of the two media and on the q parameter.

The q parameter is dimensionless and defined as:

$$q = \frac{2\pi}{\lambda^{(I)}}a, \qquad (2.39)$$

i.e. q is 2π times the ratio of the radius of the sphere to the wavelength of the light in the outer medium.

Each partial wave consists of an electric part of amplitude ${}^eB_l$ and of a magnetic part of amplitude ${}^mB_l$. The lines of magnetic force of the electric partial wave and the lines of electric force of the magnetic partial waves lie wholly on concentric spherical surfaces.

There are two important limiting cases for the relative contributions of the various partial wave to the scattered wave:

1. $q \gg 1$, the radius of the sphere is larger than the wavelength of the incident light,

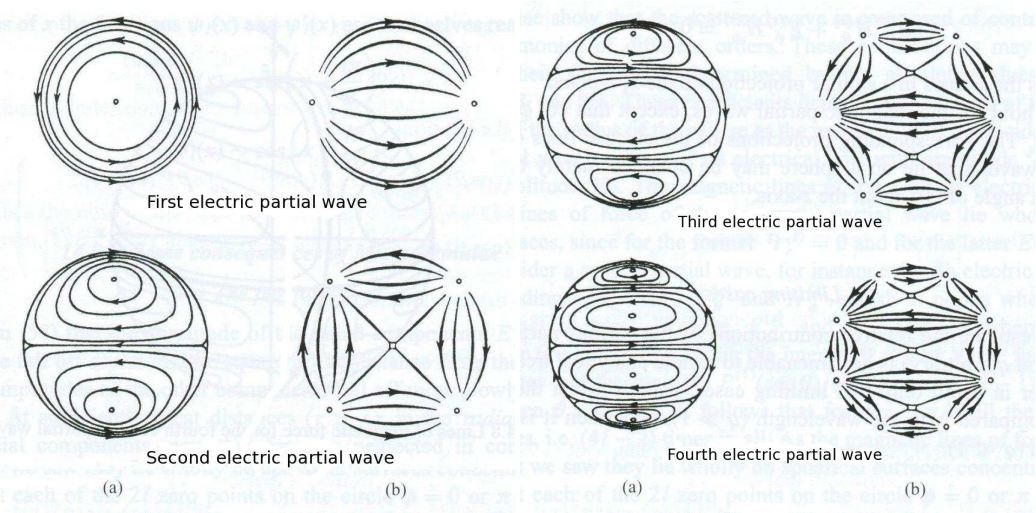

Figure 2.2: The first four partial waves: a). magnetic lines of force, b).electric lines of force.[36]

2. $q \ll 1$, the radius of the sphere is very small compared with the wavelength of the incident light.

For the first limiting case, $q \gg 1$, the Mie's solution give substantially the same results as the Huygens-Kirchhoff diffraction theory, and in the case when $q \to \infty$, the same results as geometrical optics. P.Debye [37] showed that only the first q terms need to be included in (2.35), because the amplitudes of the partial waves fall off rapidly to zero as soon as $\left(l + \frac{1}{2}\right)$ exceeds q.

The Mie's solution for $q \gg 1$ may be applied to the theory of rainbow where a is the size of the raindrops and q is of the order 10^4.

The case with $q \ll 1$ is of practical importance for micrometric and sub-micrometric particles in colloidal solutions. When the radius of the sphere is so small that q^2 may be neglected in comparation with unity, there is need to considered only the first partial wave, and its strength (and phase) will be given by the amplitude:

$$ {}^{e}B_l = iq^3 \frac{\hat{n}^2 - 1}{\hat{n}^2 + 2} = i \left(\frac{2\pi a}{\lambda^{(I)}} \right)^3 \frac{\hat{n}^2 - 1}{\hat{n}^2 + 2}. \tag{2.40} $$

The ${}^{e}B_l$ is complex so there is a phase difference between the incident field and the scattered field.

Considering now $|\hat{n}|$ finite, at large distances from the sphere ($r \gg \lambda$), the field components for the first partial electric wave will be those given in (2.41). These equations are identical with those for the field in the radiation zone ($r \gg \lambda$) of an *electric dipole situated at O, oscillating parallel to the x -axis* (Fig.2.1), i.e. parallel to the electric vector of the incident field on the sphere, and of moment $p = p_0 e^{-i\omega t}$, where $p_0 = a^3 \left| \frac{\hat{n}^2 - 1}{\hat{n}^2 + 2} \right|$.

$$\begin{cases} E_\theta^{(s)} = -\frac{i}{k^{(I)}}\cos\phi\cos\theta\, {}^eB_1\frac{e^{ik^{(I)}r}}{r} & = & \left(\frac{2\pi}{\lambda^{(I)}}\right)^2 a^3\frac{\hat{n}^2-1}{\hat{n}^2+2}\cos\phi\cos\theta\frac{e^{ik^{(I)}r}}{r} \\ E_\phi^{(s)} = \frac{i}{k^{(I)}}\sin\phi\, {}^eB_1\frac{e^{ik^{(I)}r}}{r} & = & -\left(\frac{2\pi}{\lambda^{(I)}}\right)^2 a^3\frac{\hat{n}^2-1}{\hat{n}^2+2}\sin\phi\frac{e^{ik^{(I)}r}}{r} \\ H_\theta^{(s)} = \frac{i}{k_2^{(I)}}\sin\phi\, {}^eB_1\frac{e^{ik^{(I)}r}}{r} & = & -\left(\frac{2\pi}{\lambda^{(I)}}\right)^2 a^3\frac{\hat{n}^2-1}{\hat{n}^2+2}\sin\phi\frac{e^{ik^{(I)}r}}{r} \\ H_\phi^{(s)} = \frac{i}{k_2^{(I)}}\cos\phi\cos\theta\, {}^eB_1\frac{e^{ik^{(I)}r}}{r} & = & \left(\frac{2\pi}{\lambda^{(I)}}\right)^2 \sqrt{\varepsilon^{(I)}}a^3\frac{\hat{n}^2-1}{\hat{n}^2+2}\cos\phi\cos\theta\frac{e^{ik^{(I)}r}}{r} \end{cases} \tag{2.41}$$

According to the equations (2.41) the amplitude of the scattered light is proportional with $\left(\frac{1}{\lambda^{(I)}}\right)^2$, this making the intensity of the scattered light to be proportional with $\left(\frac{1}{\lambda^{(I)}}\right)^4$. This is the so called *Rayleigh scattering*[2].

The first partial magnetic wave may be described in terms of a vibrating magnetic dipol and the partial waves of higher orders may be considered to be due to vibrating multipoles.

2.1.3 The intensity and polarization of scatter light

In the case of an incident monochromatic wave, considering the far field ($r \gg \lambda$)[3], taking as measure of the intensity of the scattered wave, the square of the real amplitude of its electric vector and setting:

$$\begin{cases} I_\parallel^{(s)} = \frac{\lambda^{(I)2}}{4\pi^2 r^2}\left|\sum_{l=1}^{\infty}(-i)^l\left[{}^eB_l P_l^{(I)\prime}(\cos\theta)\sin\theta - {}^mB_l\frac{P_l^{(I)}(\cos\theta)}{\sin\theta}\right]\right|^2 \\ I_\perp^{(s)} = \frac{\lambda^{(I)2}}{4\pi^2 r^2}\left|\sum_{l=1}^{\infty}(-i)^l\left[{}^eB_l\frac{P_l^{(I)}(\cos\theta)}{\sin\theta} - {}^mB_l P_l^{(I)\prime}(\cos\theta)\sin\theta\right]\right|^2 \end{cases} \tag{2.42}$$

we have:

$$\left|E_\theta^{(s)}\right|^2 = I_\parallel^{(s)}\cos^2\phi, \qquad \left|E_\phi^{(s)}\right|^2 = I_\perp^{(s)}\sin^2\phi\ . \tag{2.43}$$

When $\phi = 0$ or $\phi = \frac{\pi}{2}$, then $E_\phi^{(s)}$ or $E_\theta^{(s)}$ respectively vanishes so that the scattered light is linearly polarized when the plane of observation is parallel or perpendicular to the direction of vibration of the incident wave. For any other direction (θ, ϕ) the light is in general elliptically polarized and in the special case of the Rayleigh scattering the light will be linearly polarized for all directions.

The *plane of observation* is defined as the plane which contains the direction of propagation of the incident light and the direction (θ, ϕ) of observation, where ϕ is the angle

[2]In his work concerning the blue color of the sky, Rayleigh showed that this kind of scattering is also caused by spontaneous fluctuations in the density of a homogeneous medium.

[3]When considering the distant field ($r \gg \lambda$), in (2.35), the functions $\zeta_l^{(1)}$and $\zeta_l^{(1)\prime}$can be replaced by their asymptotic approximations.

between this plane and the direction of vibration of the electric vector of the incident wave.

In the case of incident natural light, the formulae for the scattered light are obtained by averaging those for the polarized light over all direction of polarization:

$$\overline{\left|E_\theta^{(s)}\right|}^2 = \tfrac{1}{2} I_\parallel^{(s)}, \qquad \overline{\left|E_\phi^{(s)}\right|}^2 = \tfrac{1}{2} I_\perp^{(s)} \ , \tag{2.44}$$

and the scattered light will be partially polarized. The degree of polarization, P, of the scattered light is defined as:

$$P = \left| \frac{I_\parallel^{(s)} - I_\perp^{(s)}}{I_\parallel^{(s)} + I_\perp^{(s)}} \right| . \tag{2.45}$$

When σ or ε are very large most of the incident light is radiated in the backward direction. From the results given by the study of the dependence of the intensity and polarization of the scattered light on the direction of scattering and on the parameters $(\lambda,\ a, \hat{n})$, for monochromatic incident light, it results the following (see Fig.2.2 and 2.3):

1. For vanishingly small spheres $(a \to 0)$, the polar diagrams for $I^{(s)} = I_\parallel^{(s)} + I_\perp^{(s)}$ and $I_\perp^{(s)}$ are symmetrical with respect to the plane through the centre of the sphere, at right angles to the direction of propagation of the incident light. For $\theta = 0$, the forward direction, and for $\theta = 180°$, the reverse direction, there is an intensity maximum. When $\theta = 90°$ (in the plane of symmetry) there is an intensity minimum.

2. When a increases, there is a departure from the symmetry, more light being scattered in the forward direction than in the reversed one; this is the *Mie effect*. Increasing still further a, practically all the scattered light is around the forward direction.

3. In the case when $a \gg \lambda$, most of the incident light is reflected as follows from the geometrical optics.

4. If $q > 1$, i.e. $\left(2a > \frac{\lambda^{(I)}}{\pi}\right)$, a series of maxima and minima of intensity appears in function of the scattering angle, and at first they are irregularly distributed.

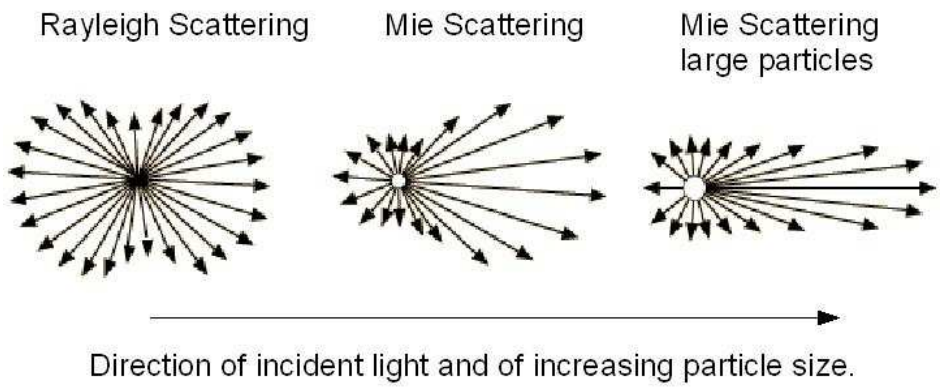

Figure 2.3: Mie scattering intensity profile function of particle radius.

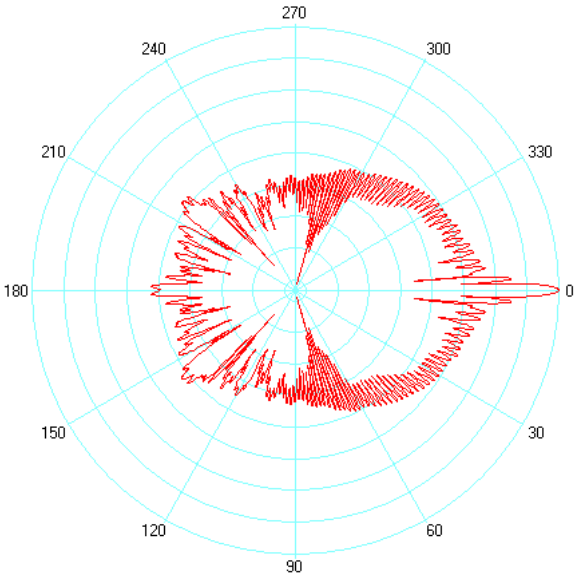

Figure 2.4: Polar diagram of scattering of red light (wavelength 0.65 µm, perpendicular polarization) from a water droplet of r = 10 µm ($q \simeq 96.67$).[38]

The results concerning the polarization of the scattered light are dependent on the value of $|\hat{n}|$:

1. If $\sigma \to \infty$ (highly conducting) or $\varepsilon \to \infty$, for very small spheres, the polarization is largest when $\theta = 60°$ (Thomson angle), and for an increasing a the polarization maximum is displaced in the direction of $\theta > 60°$.

2. When σ or ε have finite values, for very small spheres ($q \to 0$) the polarization diagram is symmetrical about the plane through the centre of the sphere, at right angles to the direction of propagation of the incident light, and has a maximum for $\theta = 90°$, where the polarization is complete. The degree of polarization is:

$$P(\theta) = \frac{\sin^2\theta}{1 + \cos^2\theta}. \tag{2.46}$$

   As a increases up to $\frac{\lambda^{(I)}}{\pi}$, the maximum is displaced in the direction of $\theta > 90°$ for dielectric spheres, and in the direction of $\theta < 90°$ for absorbing spheres. As soon as $a > \frac{\lambda^{(I)}}{\pi}$, an irregular sequence of polarization maxima appears.

3. In the direction of $\theta = 90°$, with σ or ε having finite values, for $q < 1$ the scattered light is almost completely polarized having $\mathbf{E}^{(s)}$perpendicular to the plane of observation. For $q > 1$ the behaviour becomes irregular.

If the incident light is polychromatic, the scattered intensities of the spectral components depend only on $\frac{a}{\lambda^{(I)}}$. The effect of changing the wavelength is equivalent to that of changing the radius of the sphere by an appropriate amount. For different λ, the polarization maxima will occur at different angles of observations and, when the scattered light is

observed through a polarizing prism, complicated colour changes can be observed; this effect is called *polychroism*. The wavelength dependence of the scattered light polarization is known as *dispersion of polarization* and it affords a very precise test of the theory.

2.1.4 Extinction of the incident light and cross-sections

The *optical cross-section theorem*[36] expresses in terms of the forward scattering amplitude the rate at which energy is removed from an incident, plane, monochromatic, and linearly polarized wave by the process of scattering and absorption. The *extinction cross-section* of an obstacle of arbitrary shape is the ratio Q between the rate of dissipation of energy $\left(W^{(a)}+W^{(s)}\right)$ and the rate at which the energy is incident on a unit cross-sectional area of the obstacle $\left|\left\langle \mathbf{S}^{(i)}\right\rangle\right|$:

$$Q=\frac{W^{(a)}+W^{(s)}}{\left|\left\langle \mathbf{S}^{(i)}\right\rangle\right|}=\frac{4\pi}{k}Im\left\{\frac{\mathbf{e}\cdot\mathbf{a}(\mathbf{s}_0)}{\mathbf{e}^2}\right\}. \tag{2.47}$$

In the above formula, $\left\langle \mathbf{S}^{(i)}\right\rangle$ is the time-averaged Poynting vector of the incident wave, $W^{(a)}$ and $W^{(s)}$ are the rate at which the energy is being absorbed and respectively scattered by the obstacle, $\mathbf{e}$ is the unit vector of the incident electric field, $\mathbf{s}_0$ is the unit vector in the direction in which the incident wave propagates, and $\mathbf{a}(\mathbf{s}_0)$ characterize the strength of the radiation scattered in the $\mathbf{s}_0$ direction (forward scattered).

The *scattering* and *absorption cross-section* are defined as:

$$Q^{(s)}=\frac{W^{(s)}}{\left|\left\langle \mathbf{S}^{(i)}\right\rangle\right|},\quad Q^{(a)}=\frac{W^{(a)}}{\left|\left\langle \mathbf{S}^{(i)}\right\rangle\right|}, \tag{2.48}$$

and $Q=Q^{(s)}+Q^{(a)}$.

From the Mie solution (2.35), the amplitude component of the scattered wave in the direction of the incident wave ($\phi=0$), for the forward scattering ($\theta=0$), is:

$$\left(E_\theta^{(s)}\right)_{\theta=\phi=0}=\frac{1}{2k^{(I)}}\frac{e^{ik^{(I)}r}}{r}\sum_{l=1}^{\infty}(-i)^l\,l\,(l+1)\left[{}^eB_l+{}^mB_l\right]. \tag{2.49}$$

It results that $\frac{\mathbf{e}\cdot\mathbf{a}(\mathbf{s}_0)}{\mathbf{e}^2}$ is $\frac{1}{2k^{(I)}}$; substituting in (2.47) and using the identity $Im(z)\equiv Re(-iz)$[4] , the *extinction cross section of a sphere*, in terms of ${}^eB_l$ and ${}^mB_l$, is[5]:

$$Q=\frac{\lambda^{(I)2}}{2\pi}Re\sum_{l=1}^{\infty}(-i)^{l+1}\,l\,(l+1)\,({}^eB_l+{}^mB_l). \tag{2.50}$$

In the case of a metallic sphere much smaller than the wavelength of the incident light ($q\ll 1$), the extinction cross-section has the expression:

[4]The relation $Im(z)\equiv Re(-iz)$ it is true for any complex number.
[5]For detailed explanations see p.732 and 784 of [36] .

$$Q = \frac{24\pi^2 a^3 \varepsilon^{(I)3/2} \varepsilon_2^{(II)}}{\lambda_0 \left[\left(\varepsilon_1^{(II)} + 2\varepsilon^{(I)} \right)^2 + \varepsilon_2^{(II)2} \right]} \tag{2.51}$$

where $\varepsilon_1^{(II)}$ and $\varepsilon_2^{(II)}$ are respectively the real and the imaginary part of the metal dielectric function.

Whenever $\varepsilon_1^{(II)} = -2\varepsilon^{(I)}$, there is a resonance in the spectrum of Q. This resonance is strongly dependent on the particle radius a and on the dielectric constant of the metal $\varepsilon^{(II)}$. This conditions corresponds to the enhancement of the electromagnetic field inside the metallic sphere and the collective excitations of the free conduction band electrons in the metal sphere.

The absorbance A of a colloidal solution with N non interacting spherical particles per unit volume, measured over a path length d, will be proportional to the extinction cross-section:

$$A = \log \frac{I_i}{I_d} \sim NQd \tag{2.52}$$

where I_i and I_d are the incident and transmitted intensity, respectively.

2.2 The plasmon resonances

The aim of Mie's theory was to describe the optical absorption and scattering of light by a cluster/particle and to understand the optical extinction spectra. In this theory the problem is divided in two parts: the electromagnetic problem and the material problem. The last one is solved by the introduction of the phenomenological dielectric function $\varepsilon(\omega, R)$, which may differ from the ε_{bulk} because of the effects such as the spill-out of the negative charge density beyond the sphere radius of the positive charges, or the intrinsic size effects influencing the relaxation constant Γ of free electrons. The importance and applicability of Mie's theory for metal clusters is due to $\varepsilon(\omega, R)$ since it can incorporate all important cluster effects. The Mie's theory does not give any insight into the material properties concerning the motion of electrons inside the metal particles or the discrete eigenstates.

Sixty years later, the Mie absorption was related to the collective plasmon oscillations of different multipole orders [39, 40].

2.2.1 The dielectric function: Drude model and interband transitions

The free-electron metals are those for which most of the electronic and optical properties are due to the conduction electrons alone. They have completely filled valence bands and only partially filled conduction bands. The alkali metals (Li, Na, K, Rb, Cs, Fr), magnesium (Mg), aluminum (Al), and the noble metals (Cu, Ag, Au) are considered to be free-electron metals.

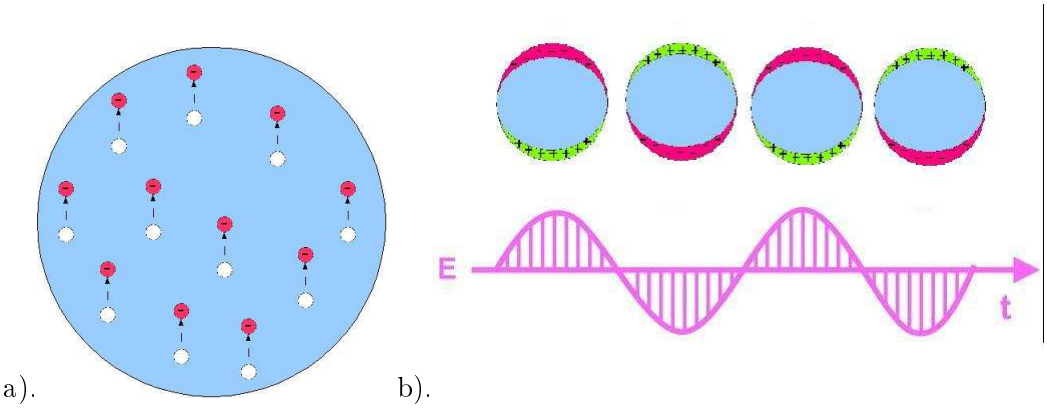

a). b).

Figure 2.5: a).Collective movement of electrons in a metallic nanoparticle, b). Excitation of a dipolar surface plasmon polariton by the electric field of an incident light wave.

The optical properties of free-electron metals are studied using the Drude-Lorentz-Sommerfeld model which assumes that the response of a metal particle to external excitations can be obtained by multiplying the response of the single free conduction electron by the number of electrons. All electrons are considered to act in phase upon a perturbation.

According to this model, the dielectric function of a system of "n" free electrons per unit volume (conduction electrons for alkali metals) can be written as:

$$\begin{aligned} \varepsilon(\omega) &= \varepsilon_1(\omega) + i\varepsilon_2(\omega) \\ &= 1 - \frac{\omega_p^2}{\omega^2 + i\Gamma\omega} \\ &= 1 - \frac{\omega_p^2}{\omega^2+\Gamma^2} + i\frac{\omega_p^2\Gamma}{\omega(\omega^2+\Gamma^2)}, \end{aligned} \tag{2.53}$$

where $\omega_p = \sqrt{\frac{ne^2}{\varepsilon_0 m_e}}$ is the Drude plasma frequency, e and m_e are the charge and the mass of the electron, $\Gamma = \frac{v_f}{l}$ is the damping constant of the electrons, l the electron mean free path, and v_f is the Fermi velocity. The damping constant is due to the scattering of the electrons on phonons, on lattice defects, impurities, etc., Γ resulting from the average of the respective collision frequencies of the electrons.

When $\omega \gg \Gamma$, the real and imaginary part of $\varepsilon(\omega)$ can be written as:

$$\varepsilon_1(\omega) \approx 1 - \frac{\omega_p^2}{\omega^2}, \qquad \varepsilon_2(\omega) \approx 1 - \frac{\omega_p^2}{\omega^3}\Gamma \ , \tag{2.54}$$

resulting that $\varepsilon_1(\omega) = 0$ implies $\omega = \omega_p$, called *the volume plasma frequency.*

The real ε_1 and imaginary ε_2 part of the dielectric function describe the polarization and the energy dissipation of matter and they are related by the Kramers-Kronig relations:

$$\varepsilon_1(\omega) = 1 + \frac{2}{\pi} P \int_0^\infty \frac{\Omega\varepsilon_2(\Omega)}{\Omega^2 - \omega^2} d\Omega, \tag{2.55}$$

where P is the principal value of the integral.

For the noble metals, $\varepsilon(\omega)$, besides the contribution from the transitions within the conduction band, there is a substantial contribution from the interband transitions. In this case the dielectric function includes all optical material properties around the visible region and can be written as:

$$\varepsilon(\omega) = 1 + \chi^{IB}(\omega) + \chi^{DS}(\omega), \tag{2.56}$$

where $\chi^{DS}(\omega)$ denotes the free-electron Drude-Sommerfeld electric susceptibility and $\chi^{IB} = \chi_1^{IB} + i\chi_2^{IB}$ is the contribution of the electrons which undergo interband transitions. Using the electric-dipol approximation for the electron-photon interaction Hamiltonian of direct transitions, Bassani and Parravicini [41] gave a basic expression for χ^{IB}:

$$\chi^{IB} = \frac{8\hbar^3\pi e^2}{m_{eff}^2}\sum_{i,f}\int_{BZ}\frac{2d\mathbf{k}}{(2\pi)^3}\left|\mathbf{e}M_{if}(\mathbf{k})\right|^2\left\{\frac{1}{\left[E_f(\mathbf{k})-E_i(\mathbf{k})\right]\left[\left(E_f(\mathbf{k})-E_i(\mathbf{k})\right)^2-\hbar^2\omega^2\right]}\right. , \tag{2.57}$$
$$\left. +i\frac{\pi}{2\hbar^3\omega^2}\delta\left[E_f(\mathbf{k}) - E_i(\mathbf{k}) - \hbar\omega\right]\right\}$$

where the integral is over the Brillouin zone, $\mathbf{e}$ denotes the unit vector along the electric field direction, $\mathbf{k}$ the vector of translation, and M_{if} is the matrix element of dipole operator $M_{if} = \left\langle\ i\ \ |e\mathbf{r}|\ \ f\ \right\rangle$, i and f denoting the initial and final states[6].

In the case of sufficiently small clusters, the quantities n, m_e, Γ, the energies $E_i(\mathbf{k})$ and $E_f(\mathbf{k})$ of the initial and final energetic level of the interband transition, and the transition matrix elements M_{if} will develop size dependencies because of the local changes of the material properties (electron density, atomic distances, etc.) close to the cluster surface, all these giving birth to a size dependent dielectric function of the cluster.

2.2.2 The position and shape of plasma resonance

In the quasi-static regime, $q \ll 1$ (which means the sphere radius is much smaller than the wavelength of the incident electromagnetic radiation $a \ll \lambda_I$), the phase retardation effects and higher multipole are neglected and then the extinction cross section (2.51) is due only to dipolar absorption. At the frequency for which the denominator, $\left[\left(\varepsilon_1^{(II)} + 2\varepsilon^{(I)}\right)^2 + \varepsilon_2^{(II)2}\right]$ has its minimum ($\varepsilon_1^{(II)} = -2\varepsilon^{(I)}$)[7], the extinction cross section Q has a resonance. This is valid for the alkali metals, but not for gold. The different behavior of the noble metals is due to their electronic properties, the influences of the core electrons in noble metals being orders of magnitude larger than those for alkali metals.

For free electron metals with $\omega \gg \Gamma$ the position of the resonance will be:

$$\omega = \frac{\omega_p}{\sqrt{1 + 2\varepsilon^I}} \tag{2.58}$$

[6] For detailed explications see Chapter 5 of Ref.[41].

[7] The $\varepsilon_2^{(II)}$ is considered to be small or to not vary much in the vicinity of the resonance.

and its shape will be described by a Lorentzian.

The width Γ^* of the resonance is generally determined by the damping constant Γ and it consists of a dispersion term, $f\left(\varepsilon_1^{II}\right)$ and a dissipative term $g\left(\varepsilon_2^{II}\right)$:

$$\Gamma^* = f\left(\varepsilon_1^{II}\right) g\left(\varepsilon_2^{II}\right). \tag{2.59}$$

In case of free electron metals with $\omega \gg \Gamma$, we will have $\Gamma^* = \Gamma$.

When the nanoparticle size became smaller than the mean free path of the electrons in the bulk metal, l_∞, the *effective* mean free path of the electrons in the nanoparticle will be $l_{eff} < l_\infty$. In these conditions the collisions of the conduction electrons with the particle surface will have an important contribution, $\triangle\Gamma(a)$, to the damping constant of the electrons in the particle[96]:

$$\Gamma(a) = \Gamma_\infty + \triangle\Gamma(a), \tag{2.60}$$

where $\Gamma_\infty = v_f/l_\infty$ is the bulk damping constant, $\triangle\Gamma(a) = A\frac{v_f}{a}$, the parameter A being a theory dependent quantity of the order of 1.

By introducing (2.60) into (2.53), one obtains the size-dependent dielectric constant of the nanoparticle in the form:

$$\begin{aligned} \varepsilon(\omega,\ a) \quad &= \left\{\varepsilon_{1\infty}(\omega) + \omega_p^2\left(\tfrac{1}{\omega^2+\Gamma_\infty^2} - \tfrac{1}{\omega^2+\Gamma(a)^2}\right)\right\} \\ &+i\left\{\varepsilon_{2\infty}(\omega) + \tfrac{\omega_p^2}{\omega^2}\left(\tfrac{\Gamma(a)}{\omega^2+\Gamma(a)^2} - \tfrac{\Gamma_\infty}{\omega^2+\Gamma_\infty^2}\right)\right\}, \end{aligned} \tag{2.61}$$

where $\varepsilon_{1\infty}(\omega)$ and $\varepsilon_{2\infty}(\omega)$ are the real and imaginary components of the bulk metal dielectric function.

The main effect of the limited mean free path, l_{eff} is the broadening of the resonance.

In consequence only the alkali metals, noble metals and aluminum will have sharp resonances. When considered in vacuum $\left(\varepsilon^I = 1\right)$, Au and Cu does not have well developed surface plasmon, respect to Ag (see Fig.2.6). Moreover, only the alkali metals and Ag have resonances in the visible spectral region.

It has to be observed that the thermodynamic phase of the cluster influences its dielectric function. The optical material functions of solid and liquid cluster are quite different and then give rise to different absorption spectra.

Embedding the clusters in transparent matrix, the plasmon resonance is red-shifted. The shift can be enhanced by using matrix with high ε^I, which shift it away from the interband transition region (see Fig.2.7.a).

When the particle size is in the range $10 \div 100nm$, the quasi-static approximation does not hold anymore and there will be extrinsic size effects due to retardation of the fields across the particle. For samples of monodispersed particles in vacuum, with increasing radius of the particles, higher-order resonances come into play (quadrupol, octupole resonances) resulting in extinction spectra with complex multipeak structures. With increasing

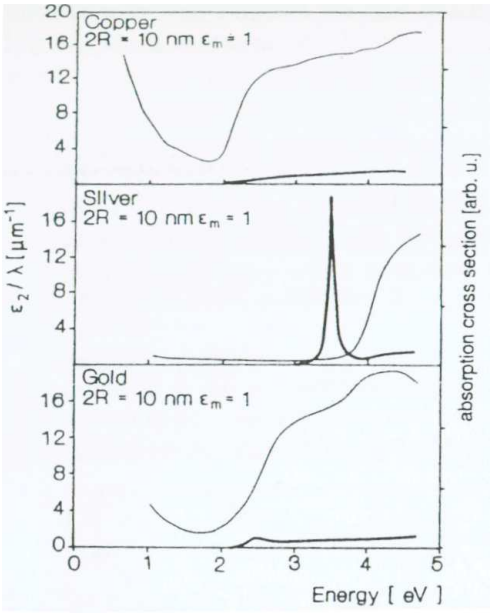

Figure 2.6: ε_2/λ for Cu, Ag and Au and their absorption cross section (bold lines) as function of photon energy.[96]

particles size, the scattering causes shifts, broadenings, and increases of the amplitude of the extinction cross section.

Realistic particle samples have a nonzero width of particles size-distribution. When the full width at half maximum (FWHM) of the particles size-distribution is increased from 0 to 50%, the multipole structures of the extinction spectra will be gradually smeared out. When the FWHM is increased above 50%, then the structures of various resonances are completely washed out and the extinction spectra seems to have only one single dominating resonance, whose λ_{max} is almost independent of the cluster size (Fig.2.7.b).

2.2.3 Corections of Mie's theory depending on the shape of the nanoparticle and their covering layers

The clusters can have non-spherical shapes and they can be composed of more than one element forming alloys or core-shell particles. These changes introduce different polarizations on the principal axes, additional boundary conditions, etc. which have to be taken into account in the Mie's theory.

The non-spherical shape of the nanoparticle induces deviations of the electric polarizability respect to that of a spherical particle, and due to $Q \sim Im(\alpha)$ [7], these changes will be reflected in the extinction spectra of the particles.

Gans [6] made the fist extension of Mie's theory: he treated the case of arbitrarily oriented ellipsoids. The ellipsoids can be *prolate* ellipsoids, when the relation of their axes is $(a > b = c)$ or *oblate* ellipsoids when $(a < b = c)$, where a is the axis of revolution. The shape of the clusters determines the geometrical depolarization factors, and consequently the electric polarizability α_i along the corresponding principal axes of the cluster. For an

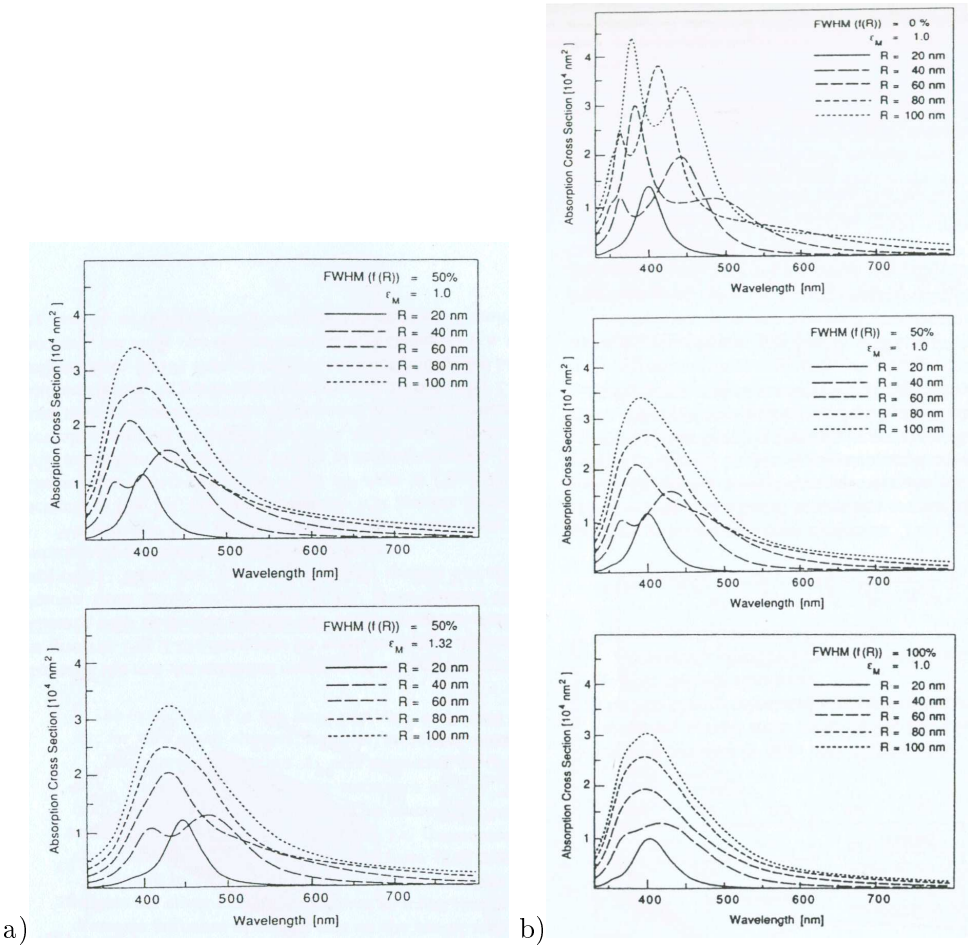

Figure 2.7: Absorption cross section for: a).free (n=1) and embedded (n=1.32) Na clusters, b).size-distributed free Na clusters in vacuum with fixed mean cluster sizes and full width at half maximum of the size-distribution.[96]

arbitrary ellipsoid we have:

$$\alpha_i = \varepsilon_0 \frac{\varepsilon^{II}(\omega) - \varepsilon^I}{L_i\left[\varepsilon^{II}(\omega) - \varepsilon^I\right] + \varepsilon^I} V_{cluster}, \tag{2.62}$$

where L_i is the geometrical depolarization factor on the i axis and $V_{cluster} = (4\pi/3)\,abc$.

The optical resonances are given by the zeroes of the denominator of (2.62) and, consequently, there are up to three resonances for arbitrary ellipsoids (see Fig.2.8.a). The magnitude of these resonances depend on the direction of polarization of the incident light with respect to the principal axis of the ellipsoid. If the ellipsoids of a sample are aligned, there are three single resonances in the absorption spectra, but a continuous cluster-shape distribution leads to smearing out these distinct peaks.

To obtain the electric polarizability for samples with arbitrarily oriented ellipsoids, Gans averaged over all orientations.

Due to the formation of crystal planes in metal clusters we find corners and edges, which prevent from the homogeneous polarization of the particle, similar to the case of

cubic[8] shape nanoparticles. In his study on the cubic shape particles, R. Fuchs [42] neglect the retardation effects, and summing over the cubic cluster modes he showed there are six most strongly excited modes. For randomly oriented cubic particles with strong damping, these modes will superimpose, in the absorption spectra resulting a single asymmetric peak (Fig.2.8.b).

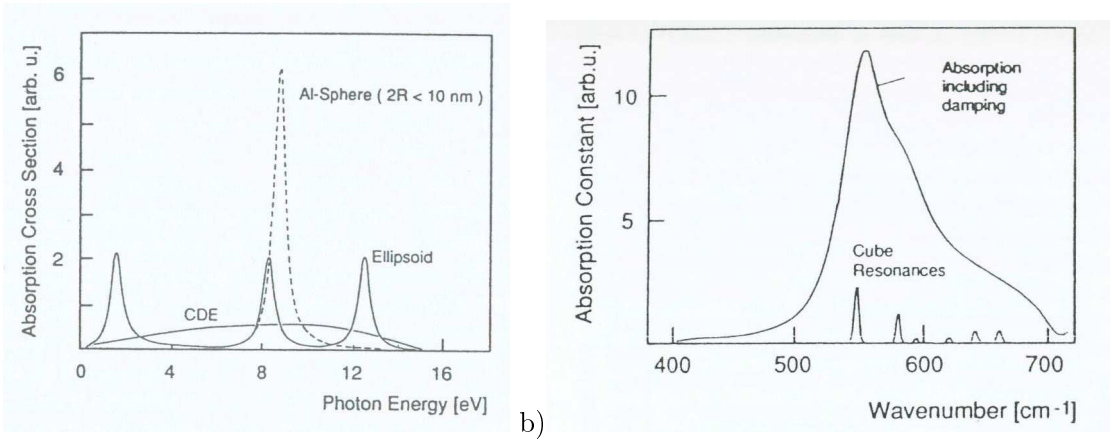

a) b)

Figure 2.8: a).Absorption cross section for Al spheres and randomly oriented ellipsoids (CDE corresponds to a continuous distribution of ellipsoidal eccentricities), b).Absorption constant for cubic MgO clusters.[96]

When the particles are composed of more than one element they can be in the form of alloys particles or core-shell particles. For the alloy particles, the same formalism as for pure metal particles, can be applied with an adequate change to the dielectric function of the nanoparticle. The core-shell particles consist of several layers of different materials centered around a core (generally are spherical or quasi-spherical particles). These materials of core and shells can be metals, dielectrics or semiconductors. The existence of the shells introduces additional internal boundary conditions, and consequently, special plasmon-polariton modes are excited in core and in shells and they couple via their interfaces, resulting in a complex multipeak extinction spectra.

If the particle has only one shell of thickness d, and dielectric function $\varepsilon_s(\omega)$ around a core of radius R, and dielectric function $\varepsilon(\omega)$, and is embedded in a matrix with dielectric function $\varepsilon_m(\omega)$, in the quasi-static approximation, the polarizability is:

$$\alpha = \varepsilon_0 \frac{(\varepsilon_s - \varepsilon_m)(\varepsilon + 2\varepsilon_s) + \left(\frac{R}{R+d}\right)^3 (\varepsilon - \varepsilon_s)(\varepsilon_m + 2\varepsilon_s)}{(\varepsilon_s + 2\varepsilon_m)(\varepsilon + 2\varepsilon_s) + \left(\frac{R}{R+d}\right)^3 (\varepsilon - \varepsilon_s)(2\varepsilon_s - \varepsilon_m)} \frac{4\pi}{3} (R+d)^3 . \tag{2.63}$$

The resulting extinction spectra will depend on the thickness of shells. In the case of a single metal shell on a metal core, the extinction spectra will have broader structure than in the spectra of particles with a single homogeneous material. For very thick shells these spectra converge to the spectra of homogeneous cluster. The interchanging of the core and

[8]The cubic shape is common for ionic particles.

shells metal materials results in strongly differing spectra.

When a metal core is covered with a dielectric shell there will be a shift of the plasmon resonance, and in the limit of large shell thickness the absorption spectra will be similar to that of the metal particle embedded in dielectric. If the metal core and the dielectric shell materials are interchanged, there is a split of the resonance in two plasmons. This is due to the two different interfaces of the metal: one with the dielectric and one with vacuum as surrounding medium.

The clusters with molten surfaces can be considered as a core-shell particles; this is the case of hot clusters in beams. The formation of the molten surface leads to a decrease in the plasmon peak.

Chapter 3

Formation of colloidal nanoparticles

The nanoparticles are produced mainly via chemical and sometimes physical methods. In nature they are created by biological pathways, by the microbes, and even in plants (Fig.3.1).

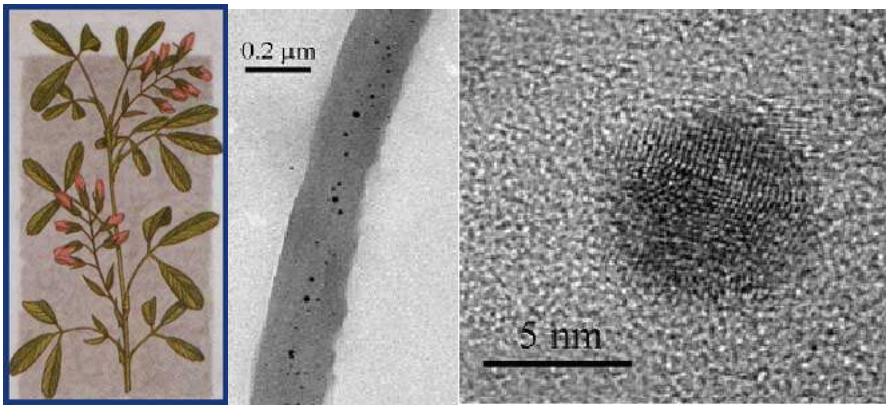

Figure 3.1: From left to right: the Alfalfa plant, TEM image of gold nanoparticles formed in an Alfalfa plant and detail of TEM image [63].

The nanoparticles can be produced as free particles in beams and smokes, embedded in homogeneous or inhomogeneous matrices, adsorbed on surfaces or as compact nanostructured aggregates. There are two different approaches for the nanoparticles production (Fig.3.2): condensing atoms into clusters and cleaving, splitting or grinding macroscopic matter.

These approaches are followed by two different theoretical concepts: the first one deals mainly with very small clusters, molecule-like structures (trimers, pentamers), for which the molecular quantum-chemical methods are applied, and the second one deals with large clusters regarded as tiny solids, for which techniques of solid-state physics are applied.

The choice of a method for the production of clusters starting from a solid state precursors depends mainly on the materials melting point. For low melting point materials, after the evaporation of the material, methods of gas aggregation or jet expansion can

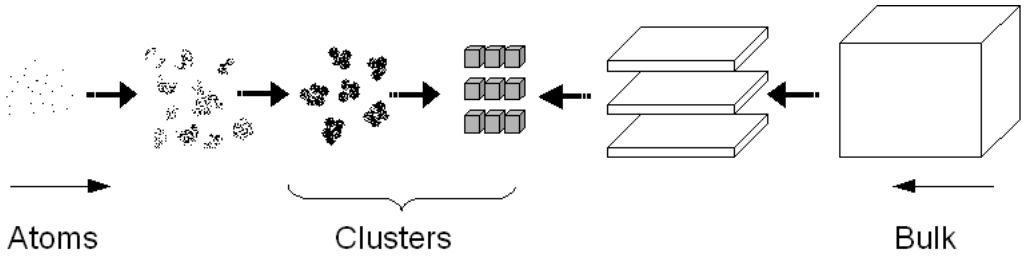

Figure 3.2: The two different approaches for production of clusters.

be used for the nanoparticles production. In these methods, the atoms or molecules are vaporized into a cold, flowing rare-gas atmosphere or the gas is expanded under high pressure through a small hole into a vacuum, both procedures leading to the atoms cooling and aggregation. In the case of high melting point materials, methods such as ion sputtering and laser ablation are used. In these cases an intense ion and laser beam respectively is directed towards the target surface and removes material in the form of neutral or charged particles, which then cluster together.

For colloidal gold nanoparticles, the conventional fabrication method is the chemical reduction of chlorauric acid ($HAuCl_4$) with citrate $[C_3H_5O(COO)_3^{3-}]$ in water, and the size control of the nanoparticles is done by adding a stabilizing agent. The drawback of the chemically produced colloidal gold nanoparticles is their contamination with reaction by-products such as anions and reducing agents, which can interfere with subsequent stabilization and functionalization steps.

A possible solution to this problem could be the production of colloidal nanoparticles by laser ablation of solid targets in liquid environment. This method gives the possibility to produce nanoparticles in a controllable, contamination-free environment, with direct formation of the colloidal solution.

3.1 Formation and growth of nanoparticles from a supersaturated solution

The formation of nanoparticles in liquids generally starts from a solution with a certain concentration of the nanoparticles material. *The nucleation* (generation of the "solid" phase) happens only if the solution is supersaturated (see Fig.3.3.a). A supersaturated solution is a solution that contains more of the dissolved material than could be dissolved by the solvent under normal circumstances.

The supersaturation of a solution leads to the nucleation and to subsequent growth of the particles. After the supersaturation point is reached, we can have a primary homogeneous (spontaneous) or heterogeneous (induced by foreign particles) nucleation, and a secondary nucleation. In the case of secondary nucleation, the generation of the "solid" phase is initiated by the presence of solid phase of the crystallizing material itself: inoculation of crystals, crystals-solution interaction or collisions. The degree of supersaturation

required for the secondary nucleation is much lower than that required for the primary nucleation.

The homogeneous nucleation is considered as a thermally activated process and the nucleation rate has a steep increase with the degree of supersaturation. There is a critical supersaturation that separates the region where no measurable nucleation occurs from that where nucleation is practically instantaneous (Fig.3.3.b). Usually the rate of nucleation at the critical supersaturation is of $1\frac{nucleus}{cm^3 s}$ [65].

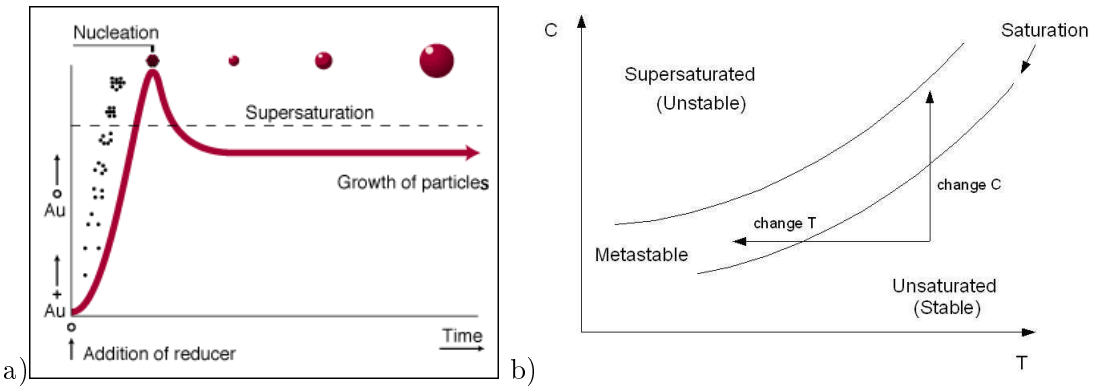

Figure 3.3: a) Nucleation and growth of the particles in solution (Reduction of gold ions to form gold particles)[64], b) Saturation-Supersaturation diagram.

The next step after the nucleation is the *growth*. The nuclei (also called *germs* or *embryonic particles*) increase their size and become nanocrystals that continue to grow. Not all the nuclei grow; there is a critical size, r_c, below which these "particles" become thermodynamically unstable and dissolve. Only the nuclei with radius larger than r_c can grow. The critical size is given by the Gibbs-Kelvin equation:

$$\frac{C_{sat}(r)}{C_{sat,\infty}} = \exp\left[\frac{2\gamma V}{rRT}\right], \tag{3.1}$$

where: $C_{sat}(r)$ is the solubility[1] of a crystal of radius r, $C_{sat,\infty}$ is the solubility of a large crystal, γ is the surface energy, V the molar volume of the solid, R is the universal gas constant, and T is the absolute temperature. The critical size, r_c depends on the supersaturation of the system.

The process of growth depends on the mass transfer, which is the transport of the solute from the bulk liquid to the nuclei surface, and on the surface integration, that is the incorporation of the solute into the solid structure. The mass transfer is generally controlled by the combined effects of diffusion and convection, but for submicron particles only the diffusion is significant [65].

To prepare uniform dispersions, the "growth by diffusion" method employed by La Mer and co-workers [66] is the most fruitful method. La Mer and Wilson introduced the valid assertion that all the particles in an assembly, growing by diffusion, develop the squares of

[1] The solubility is the maximum concentration of a dissolved substance that can exist at equilibrium for a given set of conditions, and it depends on the solvent and on the temperature.

their radii at equal rates [67]. Applying Fick's second law for a nonsteady state diffusion (the concentration within the diffusion volume changes with respect to time), Reiss [68] showed that only in the immediate neighborhood of a growing particle it is possible, in diffusion, to maintain sharp concentration gradients, and he demonstrated the validity of La Mer assumption. He also explained the existence of a "regulating mechanism" that slows down the growth of larger particles while speeding up the development of smaller ones, leading to a narrow size distribution:

$$x^2(a,t) = a^2 + G^2(t), \tag{3.2}$$

where a is the initial radius of the particle, t is the time, $G(t)$ is the rate of growing of the particle with initial radius a, and $x(a,t)$ is the particle radius at the given moment of time.

If the initial size distribution of the growing particles is not uniform (not monodispersed), since in the solution there is always a finite quantity of solute (the diffusive material), the regulating mechanism will determine how much a growth process will sharpen the size distribution (because the particles continue to grow until all, or almost all the solute in the solution is consumed).

The Reiss model can be applied to any colloidal "growth by diffusion" process and knowing the initial size distribution of the growing particles (nuclei) it gives the possibility to find the final size distribution of the grown particles.

It has to be mentioned that in crystals growth, different faces have different growth rates, but this effect is negligible for small particles [69].

In the case of metals, when their atoms are present in a liquid environment, there is a atom-to-metal transition[2]: first the metal atoms form clusters, and then the clusters grow into quasi-metallic particles, finally transforming into large metallic colloidal particles [11].

3.2 Laser ablation

Laser ablation is preferred to other methods of material removal because of the following advantages: greater flexibility for the use of materials and geometrical arrangements, almost no restriction on the material to be ablated, localized area of the evaporated source material, for surface cleaning no solvents are used, and in almost all applications the costs reduction is significant.

Lately, the laser ablation is employed as an alternative solution to the chemical production of nanoparticles and even of carbon nanotubes[43].

Laser ablation of a solid target

The laser ablation of a solid target consists of the coupling of the photonic energy to the bulk material (called *target*), the ejection of gas-phase target material, and the formation of

[2] As shown by Henglein, specially for Ag and Cu, on-line absorption spectra can be used for the observation of the atom-to-metal transition during the process of colloid formation.

a hot plasma over the irradiated surface. By means of transitions involving photon absorption, the photonic energy is coupled to the electrons of the solid target and is immediately converted into electronic excitation in the form of plasmons (for metals) or excitons[44] (for insulators). In metals, the transitions take place in the conduction band. The most of the electrons will absorb only one photon[3], which is not enough[4] to escape from the solid and in consequence the excited electrons will relax transferring their energy to the lattice and leading to the *laser induced heating* of the target[45].

Above a certain value of the laser fluence, F_{th} (the threshold fluence), significant material removal occurs in the form of an ejected luminous plasma called *plume*. This threshold value depends on the target material, its surface morphology, on the laser wavelength, and the pulse duration, τ. The material removal is controlled by the rate of thermal conduction through the lattice, which is proportional to $\sqrt{\tau}$.

When the laser pulse duration is $\tau \geq 20ps$ the ablation occurs via conventional heat deposition[44], and the threshold laser fluence, above which significant material removal occurs, is given by the energy needed to melt a surface layer of the order of the thermal diffusion length $l_T = 2\sqrt{D\tau}$ (D is the thermal diffusion constant) [46]:

$$F_{th} \approx \frac{\rho c \Delta T_m l_T}{A}, \tag{3.3}$$

where ρ and c are respectively the mass density and the specific heat of the target, $\Delta T_m = T_m - T_0$, with T_m and T_0 the melting and initial target temperature, and A is the surface absorbance[5] of the target. In this case, the threshold fluence grows[6] as $\sqrt{\tau}$ and depends on the thermal and optical properties of the target.

When the laser pulse length τ becomes shorter than the time needed to couple the electronic energy to the lattice ($\sim 10\,ps$) the heat diffusion becomes insignificant and the dependence of the threshold laser fluence on the laser pulse duration becomes weaker than $\sqrt{\tau}$ [47, 48, 49, 50]. In this case the threshold laser fluence has the value of the laser fluence needed for vaporization[46]:

$$F_{th} = \frac{\rho L_v}{\alpha A}, \tag{3.4}$$

where α is the absorption coefficient of the solid target, and L_v is the latent heat per mass unit. The values of the threshold laser fluence in this case are one order of magnitude smaller than for the case when ablation occurs via conventional heat deposition.

[3] For laser wavelength of 530nm and a laser pulse duration of 35ps.

[4] The metals workfunctions are usually of the order of 5 eV then, for the VIS and NearUV light, are necessary multiphoton processes of low order (2 or 3) for the electrons to overcome the surface barrier and escape from the solid.

[5] $A = \log(I_0/I)$, where I_0 is the intensity of the incident light, and I is the intensity of the reflected light at the target surface.

[6] This dependence is due to $l_T = 2\sqrt{D\tau}$.

Features of laser ablation plasma

The target material expelled by laser ablation forms, above the target surface, the ablation plasma called *plume*. Due to the laser beam superposition with the cloud of the ablated material, photon absorption processes take place in the plume. The two dominant photon absorption processes, in the laser produced plasma, are the photoionization of the excited neutrals and the inverse bremsstrahlung [46]. These processes are dependent on the electron and atom density, and on the laser wavelength, photon energy and intensity [49].

There are also recombination processes that reduce the number density of charged particles, and the effective degree of ionization of the laser produced plasma results from the balance between all the ionization and recombination mechanisms.

It is generally accepted that low laser intensities and very low material vaporization rates result in the formation of a collisionless, low-density vapour above the target surface. When the laser intensity increases, the vapour density increases and the ablated species cannot escape without collisions. At the target surface, in contact with it, a layer is formed [51, 52] in which reflections and collisions of the ablated species occur tending to thermally equilibrate the plasma and to lower its degree of ionization. This layer is known as *Knudsen layer*.

The presence of the Knudsen layer has a major effect on the velocities of plasma species and on their angular distribution. Most of the particles will travel in the direction normal to the target surface, and they are more energetic than the particles moving in directions forming a certain angle θ respect to the normal to the target surface.

The degree of ionization of the plasma changes during its expansion[7]. The angular distribution of the plasma has generally been fitted with a $\cos^n(\theta)$ function, with values of n ranging from 2 to more than 20. The value of n depends strongly on the laser fluence and has lower values when the plasma propagates in an environment dense enough for there to be multiple collisions that broaden the angular distribution.

When using a nanosecond or picosecond laser pulse for the ablation, the heating of the irradiated volume is fast enough to vaporize the surface during the laser pulse and the plasma shielding can occur, leading to the ionization of the nascent erosion cloud before the laser pulse is over. The bulk material under the plume will be largely screened from the last part of the laser pulse, which is efficiently absorbed by the plasma as it becomes increasingly ionized (Laser Supported Absorption).

In the case of the femtosecond laser ablation, the laser pulse terminates before the energy is completely redistributed in the solid matter and there will not be a laser-plasma interaction. Most of the input photonic energy will account for the vaporization of the ablated volume, the degree of ionization and the kinetic energies of the liberated species.

[7] The existence of a visible glow substantiates that in the plume exists a significant amount of neutrals.

Ablation of a solid target in liquid environment

When the ablation of a solid target take place in liquid environment at the target surface a thin metal layer is heated above its melting temperature. Due to the heat transfer from the metal, the adjacent water layer will be heated almost at the same temperature which is greater than the boiling temperature of the liquid in conditions of normal pressure. The vapor pressure will be about tens of atmospheres and in such conditions some liquids (different from water) could undergo chemical reactions resulting in the synthesis of new materials in the vapor layer [55]. The target ablation there will produce a large quantity of particles which will coalesce to form large nanoparticles.

The value of the laser fluence is important because it can lead to the formation of the optical breakdown in the liquid [58]. At "low" fluence, the optical breakdown of the water is avoided and direct photon ablation happens. For "high" laser fluence the optical breakdown of the water can take place and the ablation mechanism has three steps: i) direct photon ablation of the target (in the first few picoseconds), ii) formation of a cavitation bubble at the laser-target interaction point as a result of the water vaporization in contact with the hot plasma, iii) the collapse of the cavitation bubble accompanied by a release of energy [59] large enough to cause a secondary ablation of material [58, 60].

An important factor is the position of the laser focus with respect to the target (Fig.3.4), because it may allow or not the optical breakdown, influencing the laser fluence and the ablation mechanism. The occurrence of the optical breakdown phenomenon decrease the efficiency of pure radiation-related ablation, because it absorbs up to 70% of the laser power [59].

When the laser radiation is focused behind the target surface, the plasma is formed by target ablated material or, when the laser light intensity is high, in combination with the breakdown-induced plasma in water. If the laser light is focused in front of the target surface, two centers of plasma production take place. The first one, related with the water breakdown, is localized near the laser radiation focal point and it is much stronger than the second one, which is near the target surface and associated to the ablated material.

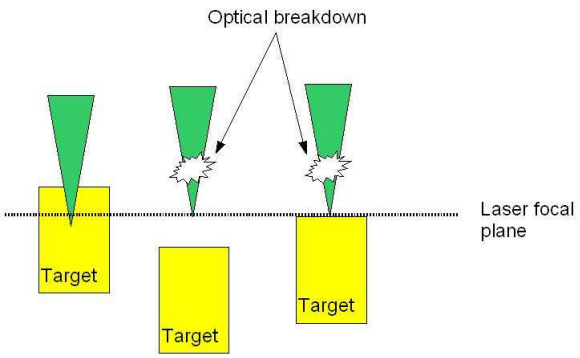

Figure 3.4: The target position with respect to the laser light focal plane, influencing the occurrence of the optical breakdown.

The efficiency of laser ablation depends on the properties of the taget material and on the laser pulse duration and wavelength. In the case of metals it is higher for materials with lower melting point temperature and hardness. When the laser ablation occurs in gaseous environment it is more efficient for shorter laser wavelengths. In liquid environment, once the colloidal nanoparticles are formed [16], the "self-absorption" of the laser light at lower wavelengths can takes place. This happens if the nanoparticles exhibit a plasmon frequency and because in liquid the particles mobility is lower than in gas, they remaining for a longer time in the laser light path.

If the extinction coefficient of the particles for the laser wavelength[8] is high enough, the particles can absorb the laser light and at the target surface arrives a reduced laser intensity leading to a lower ablation efficiency for this wavelength [49].

The literature [17] proposes two mechanisms for the process of self-absorption: the "inter-pulse" self-absorption and the "intra-pulse" self absorption. In the first mechanism, the colloidal particles formed by former laser pulses absorb the subsequent laser pulses; in this way the self-absorption is dependent on the number of laser pulses. The "intra-pulse" self absorption mechanism is independent of the number of laser pulses because the particles produced in the former part of the laser pulse absorb the later part of the same pulse. This mechanism must be taken into account mainly when the ablation of metals is made using nanosecond laser pulses, because the ejection of the ablated matter begins on the picosecond scale [16].

In the nanosecond regime, the particles found in solution have an efficient absorption of laser radiation. This can lead to additional size reduction of the particles by secondary laser ablation of the nanoparticles. For the femtosecond laser pulses this secondary ablation of colloidal nanoparticles is weak or absent, fact confirmed also by experiments of femtosecond irradiation of chemically prepared colloidal nanoparticles [62].

3.3 Formation of nanoparticles during laser ablation in liquid

A model for the formation mechanism of colloidal nanoparticles produced by laser ablation of a solid target in liquid environment has not yet been settled. It is generally accepted that during the ablation process, a laser ablated plume containing atoms, ions and small clusters is formed over the target. Because the plume is confined by a denser environment, the hot ablated species are quickly cooled and aggregate into small embryonic particles. These particles continue to grow by assembling other clusters and by attachment of free atoms, because the collisions are highly probable due to the initial velocity of the ablated species, to their diffusive mobility and to the thermodynamic instability of the cluster state. The particle growth ends up when all the surrounding clusters and atoms are consumed.

The final size of the nanoparticles and their size-distribution depends very much on the way the ablation occurs (direct radiation-ablation, shock wave or plasma-related ablation) and on the laser pulse duration which may cause or not the melting of the target.

[8] The radiation at the plasmon resonance frequency is absorbed by the metallic nanoparticles.

In the case of a pure direct radiation-ablation, without the melting of the target and plasma-related ablation, in the liquid environment are released only atoms and ions and the nanoparticles formation should proceed similarly to the particles formation from a supersaturated solution. Then, by controlling the density of ablated species, it is possible to control the final size of the nanoparticles. The density of the ablated species can be changed by adjusting the laser fluence [18, 70].

The nanoparticles can have a secondary growth due to their coalescence caused by collisions with other nanoparticles. The secondary growth together with the ejection of melted target material are the main causes for the broad size distributions of the laser produced colloidal nanoparticles.

Chapter 4

Controlling the size and shape of the nanoparticles

The laser ablation in pure water generally gives relatively large (20÷300nm) and strongly dispersed particles [54, 19, 71, 72, 73] due to: the post-ablation agglomeration of nanoclusters and the ejection of large target fragments. Moreover, the agglomeration of non-protected metal particles leads to the formation of nanoparticle aggregates with dendritic structures (Fig.4.1).

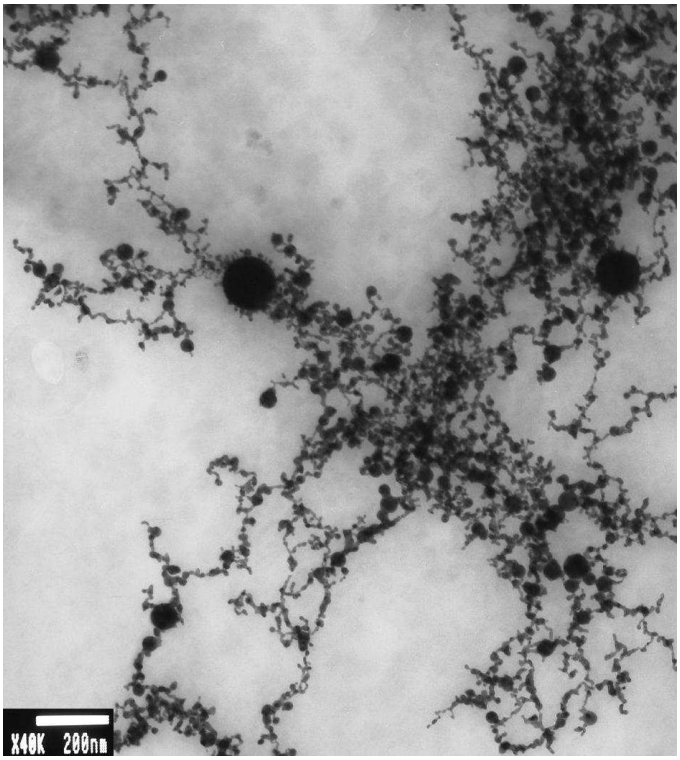

Figure 4.1: TEM image of dendritic structure formed by aggregation of gold nanoparticles in pure water.

To control and reduce the size and the size distribution of nanoparticles and to avoid

the formation of dendritic structures, the nanoparticles growth and aggregation can be controlled by chemical and/or physical methods. Nanoparticles size control by chemical methods can be done only during the nanoparticles formation and once the particle is formed there is no further chemical way to reduce the nanoparticle size. The use of the physical method for nanoparticles size control gives the possibility to control the nanoparticles size during their formation and also to reduce their size after the growth process of the nanoparticle is finished.

4.1 Chemical control for the size of gold nanoparticles

In the liquid environment, the clusters coalesce soon as collisions are highly probable due to their diffusive mobility and to thermodynamic instability of the cluster state. The stabilization depends on the nature of the liquid environment and can be created by the aqueous solution itself or by adding other substances.

For clusters to be stable in the aqueous solutions, cations of the aqueous electrolyte are necessary[96]; in pure water these cations are missing and the clusters are not stabilized. The cations adhere to the negative spill-out layers of the metal clusters forming layers at their surfaces. These interact with the charges of the ions dissolved in electrolyte and the clusters will be surrounded, protected by the so called Debye-Huckel ion clouds [96]. By their mutual electrostatic repulsion, the ions prevent a too close approach of clusters which is a prerequisite for the coalescence. This method of stabilization suffices for long term stabilization in many colloidal systems, but when the clusters are large (nanoparticles) there is need for additional stabilization. The additional stabilization is obtained by adding gelatin, surfactants or by the use of other materials which interact chemically with the cluster surfaces.

4.1.1 The protective action of Sodium Dodecyl Sulfate

The nanoparticle size can be drastically reduced by the use of aqueous solutions of surfactants [71], which cover the particles just after their ablation and thus prevent them from further agglomeration.

The surfactants are wetting agents that lower the surface tension of a liquid (allowing easier spreading) and the inter-facial tension between two liquids. They are usually organic compounds that are amphiphilic, meaning they contain both hydrophobic groups (their "tails") and hydrophilic groups (their "heads"), therefore, they are soluble in both organic solvents and water. The surfactants are often classified by the presence of charged groups in its head, into four primary groups: non-ionic, ionic (anionic, cationic), and zwitterionic (dual charge) (see Fig.4.2).

An efficient size-reduction of gold nanoparticles was observed [71, 74] by the use of anionic surfactants. These surfactants are used more for the study of nanoparticles formation because they are not always suited to be used in applications, especially for biosensing

applications, because of their biocompatibility problems.

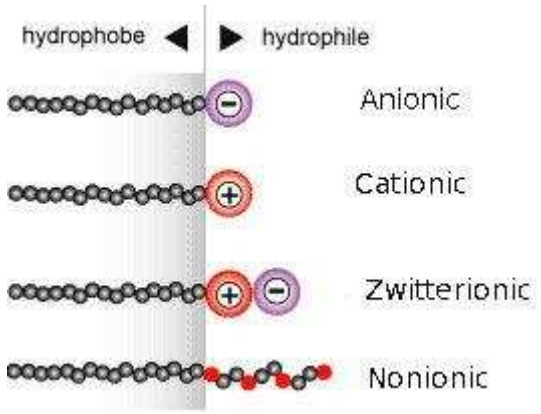

Figure 4.2: Surfactants.

When the nanoparticles are produced by laser ablation in aqueous solution of surfactant, it is supposed that the process of their formation is divided in two parts. The first part is the rapid formation of an embryonic particle, due to aggregation of target ablated atoms which are found in the core[1] close vicinity ($\sim$ 40nm for Au and $\sim$ 100nm for Ag [19]). The formation of the embryonic particle ends up when the vicinity is void of ablated atoms. The second part of the formation process is the growth of the embryonic particle. The final size of the nanoparticle is the result of two competing processes: the slow growth of the embryonic particle by adding ablated atoms which enter its vicinity by diffusion, and the coating of the particle surface with surfactant molecules.

According to this dynamic formation model, the final size of the nanoparticle depends on the number density of ablated atoms present in the core vicinity, and the number density of surfactant molecules in solution. By controlling these two factors one could select a desired nanoparticle size. Because the number density of ablated atoms depends mainly on the laser fluence, one can produce colloidal gold nanoparticles with a desired average diameter in aqueous solution of surfactant [20, 21] by optimizing the laser fluence and the surfactant concentration.

The termination of particle growth depends strongly on the diffusion and on the attachment rates of the surfactant to the particle. For this reason the size-distribution and the nanoparticles stability have a critical dependence on the surfactant properties.

The nanoparticles produced by laser ablation in aqueous solution of anionic surfactants based on sulphate ($C_nH_{2n+1}NaO_4S$) has been proven [75] to have maximum stability when the hydrophobic interaction between surfactant molecules is sufficiently large to form a stable double layer on the nanoparticle surface. In the first layer, the surfactant molecules are oriented with the hydrophilic groups towards the nanoparticle and the hydrophobic groups outwards, while they behave oppositely in the second layer (Fig.4.3.a). The two layers are bound by a hydrophobic interaction between the surfactant molecules.

[1] The core denotes the center of the region where the embryonic particle is formed.

Sodium dodecyl sulphate (SDS or NaDS)[2], also known as sodium lauryl sulfate (SLS), is one of these anionic surfactants. Being composed by a tail of 12 carbon atoms (hydrophobic group) attached to a sulfate group (hydrophilic part), the SDS molecule ($C_{12}H_{25}NaO_4S$) (Fig.4.4) has amphiphilic properties. Due to this property it can be used to control the size of colloidal nanoparticles during their formation process by enclosing them inside the forming micelle[3] (see Fig.4.3.b).

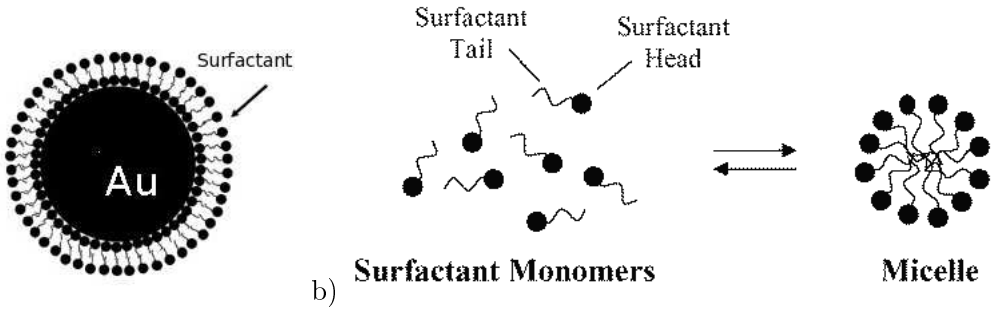

a) b)

Figure 4.3: a) Nanoparticle stabilization by a surfactant double layer, b) Surfactant micelle formation.

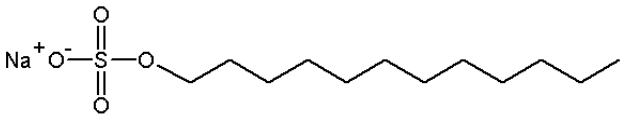

Figure 4.4: The molecule of sodium dodecyl sulphate.

The final size of the nanoparticles has an important dependence on the SDS concentration [19]. There is a critical concentration of SDS ($\sim 8 \times 10^{-3}$M) above which the forming nanoparticles start to be covered with SDS molecules. This SDS concentration is very close to the critical micelle concentration of SDS (8.2×10^{-3}M, in pure water at 25°C) [33]. It follows that the nanoparticles are stabilized only when SDS micelle are formed. With increasing SDS concentration, the nanoparticles are more stabilized and their coagulation is much slower.

Depending on the nanoparticles material, there is a surfactant concentration for which the maximum stability is reached (0.1M for Au nanoparticles, and 0.01M for Ag nanoparticles [19, 75]). When the surfactant concentration exceeds this value the nanoparticles precipitation takes place due to the "salting-out effect" and the binding of several stabilized nanoparticles by the SDS. The "salting-out effect" consist of the weakening of the

[2]The SDS is commonly used in household products (toothpastes, shampoos, shaving foams and bubble baths), and in laboratories is often used in preparing proteins for polyacrylamide gel electrophoresis [33].

[3]A typical micelle in aqueous solution forms an aggregate with the hydrophilic "head" regions in contact with surrounding solvent, sequestering the hydrophobic tail regions in the micelle centre. This type of micelle is know as a normal phase micelle (oil-in-water micelle). Inverse micelles have the head-groups at the centre with the tails extending out (water-in-oil micelle). Micelles are approximately spherical in shape. Other phases, including shapes such as ellipsoids, cylinders, and bilayers are also possible. The shape and size of a micelle is a function of the molecular geometry of its surfactant molecules and solution conditions such as surfactant concentration, temperature, pH, and ionic strength.

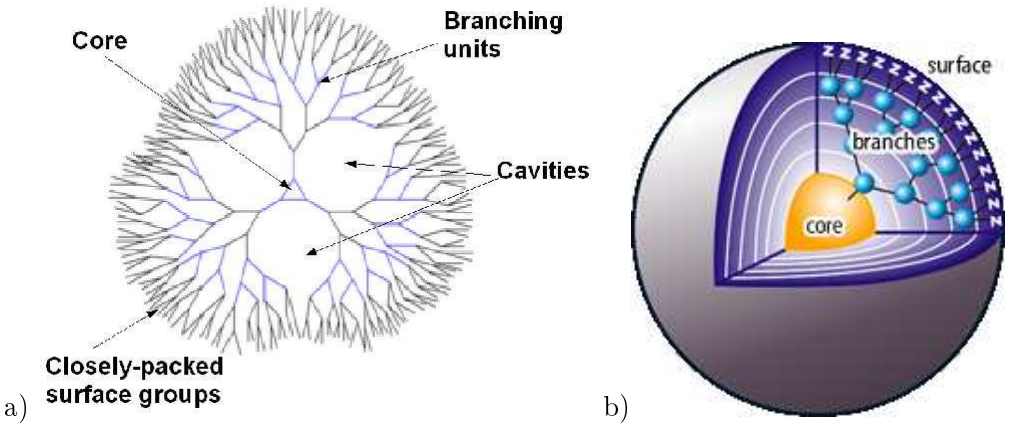

Figure 4.5: The dendrimer structure: a) 2D structure, b) 3D structure.

repulsive force between the nanoparticles, because the excess of SDS neutralize the coating, $C_{12}H_{25}SO_4^-$, through the equilibrium $C_{12}H_{25}NaO_4S \Longleftrightarrow C_{12}H_{25}SO_4^- + Na^+$[75].

The preparation in a micelle or reverse micelle is one of the most successful methods to obtain metal nanoparticles stabilized in solutions and SDS was found [19] to be the most efficient among surfactants to reduce the mean diameter of gold nanoparticles. However the SDS has two main disadvantages: it terminates the nanoparticle surface making it hardly useful for bio-immobilisations, and it is not biocompatible (denaturates the proteins causing the molecules to lose their native shape [33]).

4.1.2 Controlling nanoparticle size with dendrimers

Dendrimers are spheroid or globular nanostructures that are precisely engineered to carry molecules encapsulated in the interior void spaces or attached to the surface. They are constructed by addition of shells of branched molecules to a central core (Fig.4.5). Their size, shape, and reactivity are determined by generations (shells) and chemical composition of the core, interior branching, and surface functionalities. The dendrimers diameter increases linearly, whereas the number of surface groups increases geometrically. They are commonly created with dimensions incrementally growing in approximately nanometer steps from 1nm to over 10 nm.

By adjusting chemical properties of the core, of the shells, and especially of the surface layer, dendrimers can be tailored to fit the needs of specific applications. They can have catalytic core functionalities or peripheral catalytic sites. Their precise and designable architecture, tunable solubility, low toxicity and immunogenicity, and bioattachment capability make dendrimers the ideal building blocks for biotechnology.

A dendrimer is water-soluble when its end-group is a hydrophilic group. It is theoretically possible to design a water-soluble dendrimer with internal hydrophobicity, which would allow it to carry a hydrophobic drug in its interior, and then dendrimers can be used for drug delivery systems. An important property is that the dendrimer volume increases when it has a positive charge.

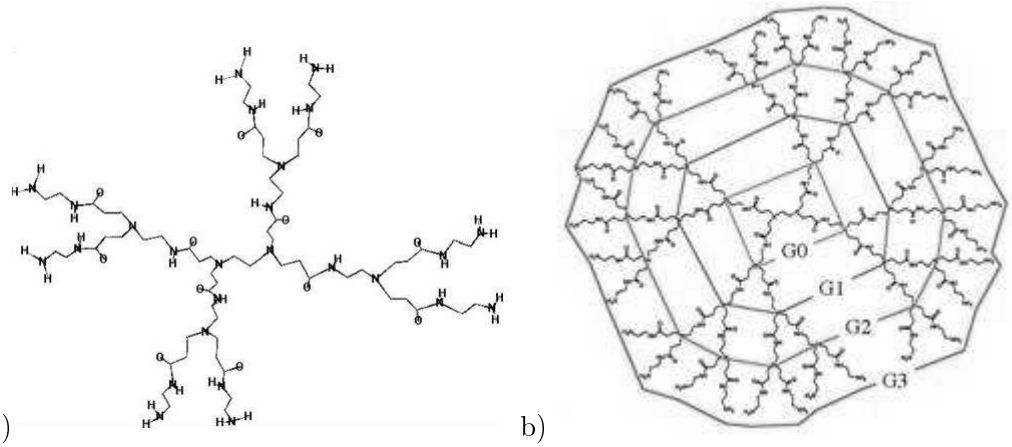

a) b)

Figure 4.6: 2D structure of PAMAM dendrimer: a) generation 1 (G1), b) generation 3 (G3).

Tomalia's PAMAM (polyamidoamine) dendrimers[34] (Fig.4.6) were the first dendritic structures that have been thoroughly investigated and received a wide-spread attention. PAMAM dendrimers are positively charged at physiological pH and can thus interact with biologically relevant anions such as nucleic acids [35].

Most dendrimers possess flexible branches that can take different conformations, implying that the end groups can fold back into the interior of the molecule. The flexibility in dendritic molecules allows them to take shapes that are far from globular[4].

Since dendrimers contain a large number of regularly spaced internal and external functional groups (see Fig.4.5 and Fig.4.6), it is expected that they operate as templates to grow inorganic crystal in their internal or external region, resulting in organic-inorganic hybrid nanostructures. By using dendrimers as templates, dendrimer-metal nanoparticles are chemically synthesized in aqueous and non-aqueous media, metal particle sizes being significantly affected by the dendrimer concentration and by the dendrimer generation.

Until now the dendrimer-gold nanoparticle were synthesized only chemically[5] [76, 77, 29]. It has been observed that the size of gold particles and their size-distribution decreases with increasing the dendrimer concentration. Due to the strong interaction between the metal particles and the external functional groups of the dendrimer[6], the dendrimer concentration required to obtain stable metal nanoparticles is extremely low compared to that of linear polymers used as a protective colloid for the nanoparticles.

When gold nanoparticles are produced in PAMAM dendrimers with the surface amino ($-NH_2$) group, the average particle size decreases with an increase of the dendrimer generation. This is due to the raising of the number of surface amino groups[76]. It was shown that low generation (G0) PAMAM do not have an effective protective action for the

[4]Such shapes are only observed when dendrimers are exposed o external stimuli.

[5]Dendrimer-gold nanoparticle were synthesized by reduction of $AuCl_4^-$ with irradiation of UV in aqueous solution [76], and by addition of reductants such as sodium borohydride, $NaBH_4$ into noble metals ions-dendrimer aqueous solution[77, 29]

[6]The strong interactions were observed between gold nanoparticles and dendrimers with amino group and silver nanoparticles and dendrimers with carboxyl group.

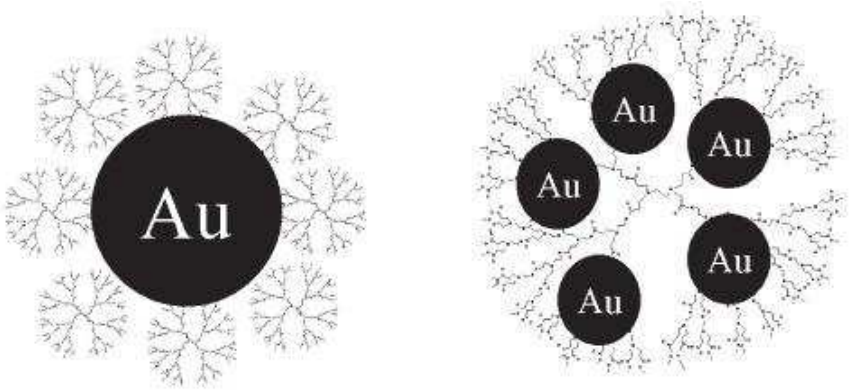

a) b)

Figure 4.7: Possible configurations of PAMAM-metal nanoparticles [78].

colloidal nanoparticles, like it happens for higher generations (G5-G10) PAMAM.

There are two possible configurations for the formation of PAMAM-protected-metal nanoparticle. In the first, the nanoparticle surface can be surrounded by several dendrimer molecules (Fig.4.7.a) and is meet mainly when low generation PAMAM are used.

In the second configuration (see Fig.4.7.b) the metallic nanoparticles are trapped inside the dendrimer. This configuration is meet only when G6-G10 PAMAM are used, and is due to the fact that they provide, in their inner cavities, sites for complex formation. This property can significantly reduce the size of metal nanoparticles. Gold nanoparticles (with sizes up to 4nm) can be completely formed inside individual dendrimer molecule. In the case of G10 PAMAM, has been shown[78] that within one molecule multiple gold nanoparticles (up to 3 nanoparticles of 4nm diameter each [78]) can be formed (in the case of chemical production of gold nanoparticles), due to more crowded volume inside the dendrimer.

4.2 Light changing the size and shape of nanoparticles

Once the colloidal nanoparticles are formed, there is no chemical way to further change their size. However, there is the possibility of using a physical method to reduce the nanoparticles size and shape after the production process ends.

If the nanoparticles of the final colloidal solution possess a strong absorption band at an energy that coincides with the energy of a laser, the nanoparticles can be excited by laser irradiation leading to desorption of their atoms, and then to the changing of their size. This technique is called "laser-assisted size-control" and could be a powerful tool to prepare nanoparticles with desired size and size-distribution. It has to be mentioned that, since the atoms desorb preferably from surface sites with low coordination number[7], the

[7] In materials science, the bulk coordination number is the number of atoms touching any other atom in a crystal lattice. The surface coordination number is always less than the bulk coordination number, and is dependent on which Miller index the surface uses. Miller indices are a notation used to describe lattice planes and directions in a crystal.

particles do not only shrink in size but may also change their shape.

For metallic nanoparticles, the rate of desorption of the atoms depends on the laser wavelength and on the particle size, meaning that the process is stimulated by excitation of surface plasmons [79]. Since the gold nanoparticles have an intense surface plasmon peak centering at 520nm, their size-control can be performed using a 532nm laser wavelength. Because the resonant surface plasmon frequency depends also on the particle size, it is possible to have a size-selected fragmentation of the nanoparticles by simple use o a certain laser wavelength.

The size reduction of the nanoparticles can be a photo-thermal process or/and a photo-fragmentation process caused by multiphoton ionization.

In the case of photo-thermal effects (which occurs mainly when nanosecond lasers are employed) the size of the nanoparticles are reduced as a consequence of their increased temperature up to the boiling point. If the boiling temperature can't be reached, then the explanation is that the nanoparticle reach a temperature that allows the formation of a layer of vapor on its surface [60, 80, 25]. This process is possible when the dissipation of energy is not sufficient. The heat dissipation depends on the surrounding of the nanoparticles and whether they are capped or not. Smaller nanoparticles have fast heat dissipation and they are less expected to reach a temperature sufficient for reduction, which explain the observation that larger particles are reduced to smaller particles [25].

When the laser fluence is not high enough, the nanoparticles do not absorb the energy required for size reduction, and this process usually leads to the reshaping of the nanoparticles with edges or spheroidal forms which will be transformed into spheres[81, 82, 83].

The process of size reduction by photo-fragmentation has three steps[84]: the electron ejection from nanoparticle, the formation of a transient state in the nanoparticles, and the fragmentation. The electron ejection leads to charging of the nanoparticle surface and intraparticle changes occur resulting in a transient state, which is an intermediate in the photo-fragmentation process. The intermediate state is seen as an aggregate [84] of smaller clusters and trapped electrons that are in proximity. Finally the transient aggregate will disintegrate in smaller nanoparticles.

In the process of photo-fragmentation the laser irradiation leads to the fragmentation of the nanoparticles with an average diameter larger than a threshold value. This threshold value decreases as the laser fluence increases.

When the colloidal nanoparticles are irradiated with a laser light, in order to reduce the nanoparticles diameter, the following processes will take place: the fragmentation of "parent" nanoparticles, Au_n , and the aggregation of the "product" nanoparticles, Au_m [13]. In the process of fragmentation, the "parent" nanoparticle is fragmented in the "product" nanoparticles, p gold atoms, and q small fragments Au_i of gold nanoparticles:

$$Au_n \xrightarrow{h\nu} Au_m + pAu + qAu_i.$$

The fragmentation products are dispersed in the solution, therefore, the nanoparticles

present in the solution can grow by adding these fragments:

$$Au_m + pAu + qAu_i \longrightarrow Au_{m'} + Au_k + p^{'}Au + q^{'}Au_i,$$

where $Au_{m'}$ is the grown "product" nanoparticle, Au_k is a new nanoparticle produced by aggregation of small fragments, and $p^{'}Au$ and $q^{'}Au_i$ are the rest of p' gold atoms and q' small fragments dispersed in the solution.

The fragmentation rate is proportional with the laser fluence and the aggregation is proportional with the concentration of small fragments in the solution.

During the laser irradiation of the nanoparticles the following changes take place:

- the fragmentation rate of each nanoparticle decreases during the irradiation (because its absorption coefficient per atom decreases with the decrease of its diameter),
- the aggregation rate increases because the concentration of the small fragments increases.

When the rate of fragmentation equals that of aggregation, the average diameter of the nanoparticles reach its minimum value[8], and when the laser irradiation is stopped, the fragmentation is terminated. The aggregation will continue until all the gold atoms and the small fragments are consumed.

The physical size-control is also possible during the production of the nanoparticles by laser ablation of a solid target in liquid [17, 19, 60]. When the forming nanoparticles reaches the size for which the plasmon resonance almost coincides with the laser wavelength used for target ablation, these nanoparticles are excited and the desorption of their atoms takes place. In this way one will have two co-existing actions of the same laser beam: the ablation of the solid target and the size reduction of the existing nanoparticles.

[8] For the given laser wavelength.

Chapter 5

Experiments and results

5.1 Materials and experimental setups

The preparation of the colloidal gold nanoparticles was done by focusing the fundamental (1064nm) or the second harmonic (532nm) of a modelocked Nd-YAG laser (EKSPLA PL2143A: repetition rate 10Hz, pulse width 25ps at 1064nm and 20ps at 532nm) on a gold solid target (Goodfellow) placed on the bottom of an optical glass cuvette containing the liquid environment. The liquid column above the target was 2cm.

The ablation process and the subsequent production of nanoparticles were monitored by measuring on-line the transmittance[1] T of a low power beam at 514.5nm (T@514.5nm) from an Ar laser. Being near the central wavelength of the characteristic plasmon resonance of the gold nanoparticles, the decrease of T@514.5nm is associated to the plasmon band. The experimental setup is sketched in Fig.5.1. The ablation laser beam enters from the top of the cell and incides perpendicularly on the gold target. The Ar laser beam passes horizontally through the cuvette, at 2mm from the Nd:YAG beam and 3mm from the target.

The Ar beam transmitted through the cuvette enters the photodiode, the signal is transmitted to the data acquisition system and registered using a LabView program. This program controls also the laser (on/off and repetition rate) and it allows us to vary the number of laser shots after which the acquisition of the transmitted signal is made. For a best monitoring of the ablation process and of the particles formation, the Ar transmitted signal was registered after each laser shot.

The gold nanoparticles suspensions were prepared in: doubly deionized water (18.2 MO.cm @25°C), aqueous solution of sodium dodecyl sulfate (SDS), and aqueous solutions of ethylendiamine-core poly(amidoamine) dendrimer of generation 5 with primary amine surface functional group, PAMAM G5. SDS was from Carlo Erba Reagents and PAMAM G5 from Dendritech®.We prepared gold nanoparticles by laser ablation also in: toluene, chloroform, and diethyl ether, all of them from Carlo Erba Reagents.

[1] In the graphics we plot I_T/I_0 where I_T is the intensity of transmitted light at a given moment during the nanoparticles production and I_0 is the value of the transmitted light through the cell containing the liquid environment before the beginning of the ablation.

The laser pulse energy was varied from 0.1 to 40mJ, with corresponding fluences ranging from 0.013 to $2.6 J/cm^2$, and the ablation time from few seconds to several hours. If not differently specified, the focussing conditions of the laser beam were maintained constant in all the experiments and the diameter of the laser spot on the gold target was 1.4mm for both wavelengths.

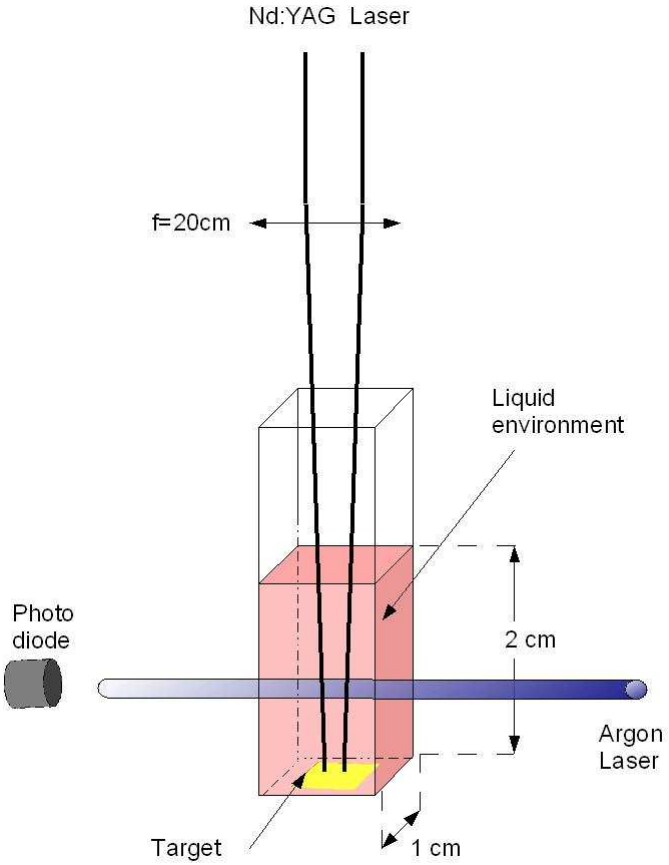

Figure 5.1: The setup for the laser ablation of a solid target in liquid environment and on-line monitoring of the subsequent formation of colloidal nanoparticles.

The UV-VIS spectra were recorded with a double beam spectrophotometer (Perkin Elmer mod. Lambda19) one day after the preparation of the suspensions. TEM images of the nanoparticles were obtained by dipping copper grids in the suspensions and the images were recorded with a HRTEM JEOL2010, 200KV.

The particle mean diameter and dispersity were determined by analysis of the TEM images using Image J software. In each case the length scale was set to the value given by the TEM photo. The diameter of each particle was measured using the Image J tool for measurements. The precision of the measurements done in this manner was of 0.01nm.

The SEM images were obtained by evaporating the colloidal solution on a Ta foil, and SEM images were recorded with a Scanning Electron Microscope JEOL JSM-5600LV.

UV irradiation of PAMAM G5-gold nanoparticles suspensions was performed by using a low power lamp emitting at 245nm (model UVG-11, Ultraviolet Products Inc.) with an

estimated intensity on the samples of the order of $10\text{mW}/cm^2$. As will be shown later, the purpose of this irradiation was to determine the workfunction of the gold nanoparticles.

For the production of colloidal gold nanoparticles in solutions at different temperatures, the setup was modified as shown in Fig.5.2. The cuvette containing the solution was introduced in a metal cell in contact with a Peltier cooler which allowed to vary the solution temperature between -5°C and +50°C. The value of the solution temperature was estimated from the measurements of its resistivity using a thermocouple. The metallic cell was opened at the top side, to allow the entrance of the ablating laser beam, and had also an aperture for the entrance of the monitoring Ar laser beam

The ablating laser was switched on only when the solution resistivity settled at a constant value indicating that the same temperature was reached in all the liquid..

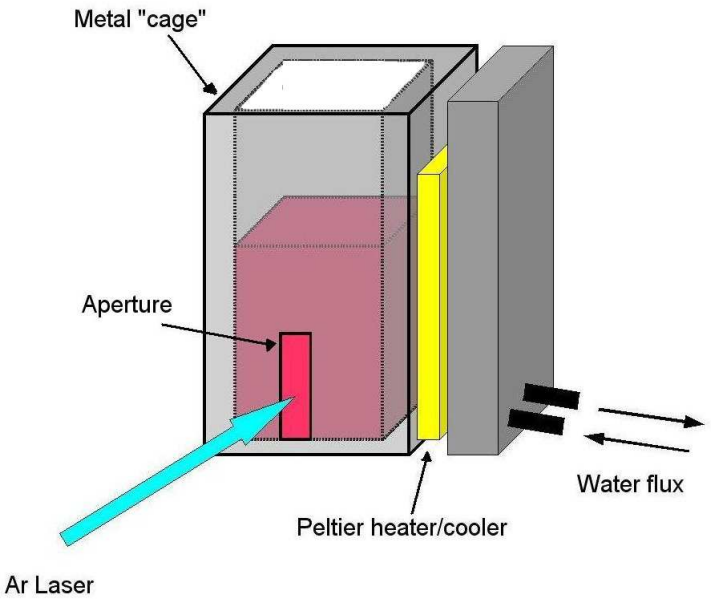

Figure 5.2: The setup used for production of nanoparticles in solutions at different temperatures.

After the laser is switched on, in every liquid environment, almost instantly, a reddish jet can be seen coming up from the target on the laser beam trajectory, as also reported by the results of Tsuji group[88] for the microsecond-resolved imaging of laser ablation at solid-liquid interface (see Fig.5.3.a). The jet material diffuses in the entire liquid environment, and in a few minutes of laser ablation the solution changes its color into different nuances of red or violet (Fig.5.3.b) depending on the liquid properties and the laser parameters. The color changing is evidence for the formation of colloidal gold nanoparticles with diameter bigger than 2nm which exhibit the plasmon band absorption.

a) 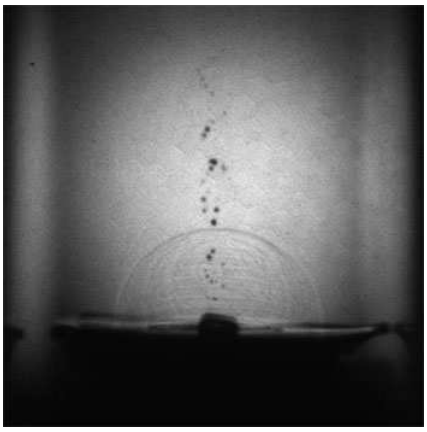 b) 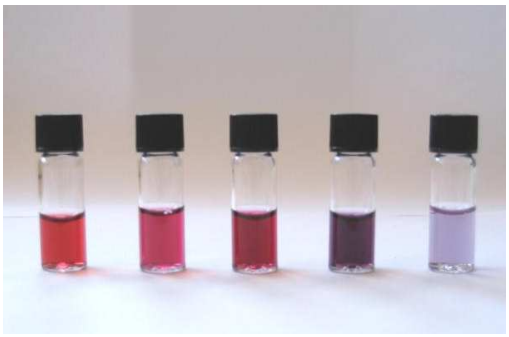

Figure 5.3: a) Microsecond-resolved imaging of laser ablation of an Ag target at solid-liquid interface[88], b) Colloidal gold nanoparticles with different sizes.

5.2 Gold nanoparticles in H_2O

5.2.1 Experimental results

The study of the production of colloidal gold nanoparticles by ablation method was first investigated using doubly deionized water (18.2 MO.cm @25°C) as liquid environment. The first evidence for the generation of gold nanoparticles in water was the reddish jet coming up from the target. In a few minutes after the beginning of the gold target ablation, the entire liquid turned red. The absorption spectra of the resulting solution exhibited the characteristic band around 520nm, which is associated with gold nanoparticles plasma oscillations of conduction electrons in water (see Fig.5.4).

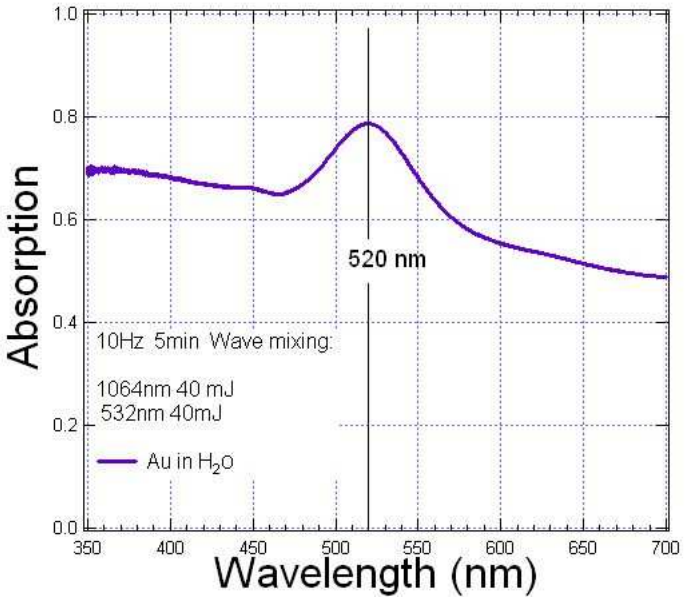

Figure 5.4: Absorption spectra of colloidal gold solution in doubly deionized water.

Since the position of laser focus with respect to the target is an important factor of the

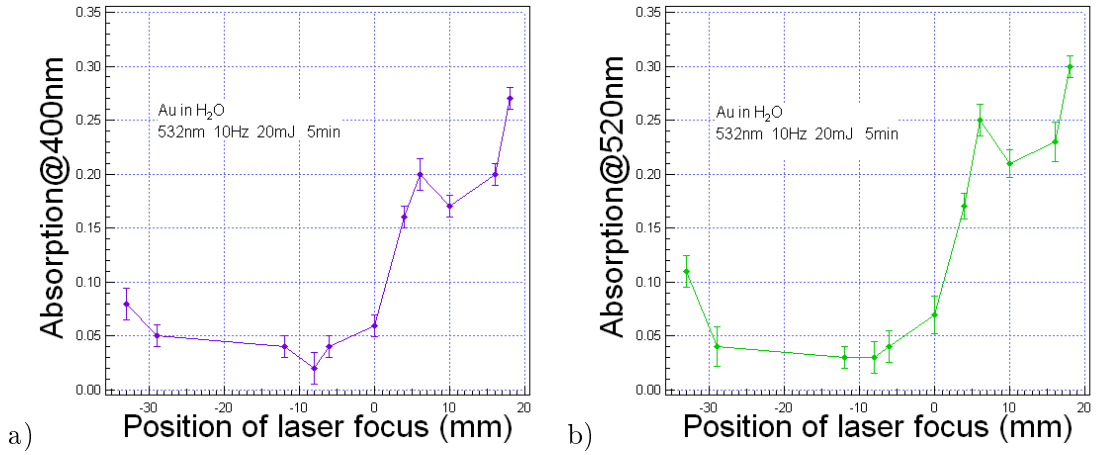

Figure 5.5: Absorption at 400nm a), and 520nm b) of solutions produced with the laser beam focalised behind and in front (-) of the target surface.

laser ablation in liquid environment, because of its influence on the ablation mechanism (see Section 3.2), we first prepared a number of samples focalising the laser beam at different distances from the target. The position of laser focus was varied between 18mm behind the target surface, to 33mm in front of the target surface.

To evaluate the abundance of gold in solution, and then the ablation efficiency, the method proposed by Ref.[20] was adopted. Since the spectral features below 450 nm do not significantly change with preparation conditions and the absorbance below 450nm is proportional with the concentration of gold atoms present in the solution[19, 20], we took the absorbance at 400 nm (A@400nm) as a measure of the quantity of gold ablated from the target.

To monitor the changes in the plasmon band absorption we used the absorbance at 520nm (A@520nm) and the central wavelength of the plasmon band.

In Fig.5.5.a[2], it can be seen that, only when the laser is focused at least 5mm behind the target surface, a bigger quantity of ablated gold is found in the liquid. Moreover, only in these conditions, the absorption spectra presents an increased absorption in correspondence with the plasmon band of gold nanoparticles at 520nm (Fig.5.5.b). This means that the ablation and the production of colloidal gold nanoparticles, which exhibit the plasmon band, is more efficient when the laser is focused at least 5mm behind the target surface[3]. For this reason, in all the following experiments, the laser beam was focused at 2cm behind the target surface.

Further we investigated the differences in the production of colloidal gold by ablation with the two laser wavelengths (1064nm and 532nm) and at different laser energies and repetition rates. The time of ablation was varied in such a way that the total energy (in mJ) employed for preparation of the sample (with a certain laser wavelength) was the same

[2]In all the figures of this thesis, the line between points is only a guide for the eye.

[3]This is due to the fact that a focalised beam produces laser droplets and nanoparticles of greater size which precipitate fast, in the liquid remaining only a smaller quantity of ablated gold.

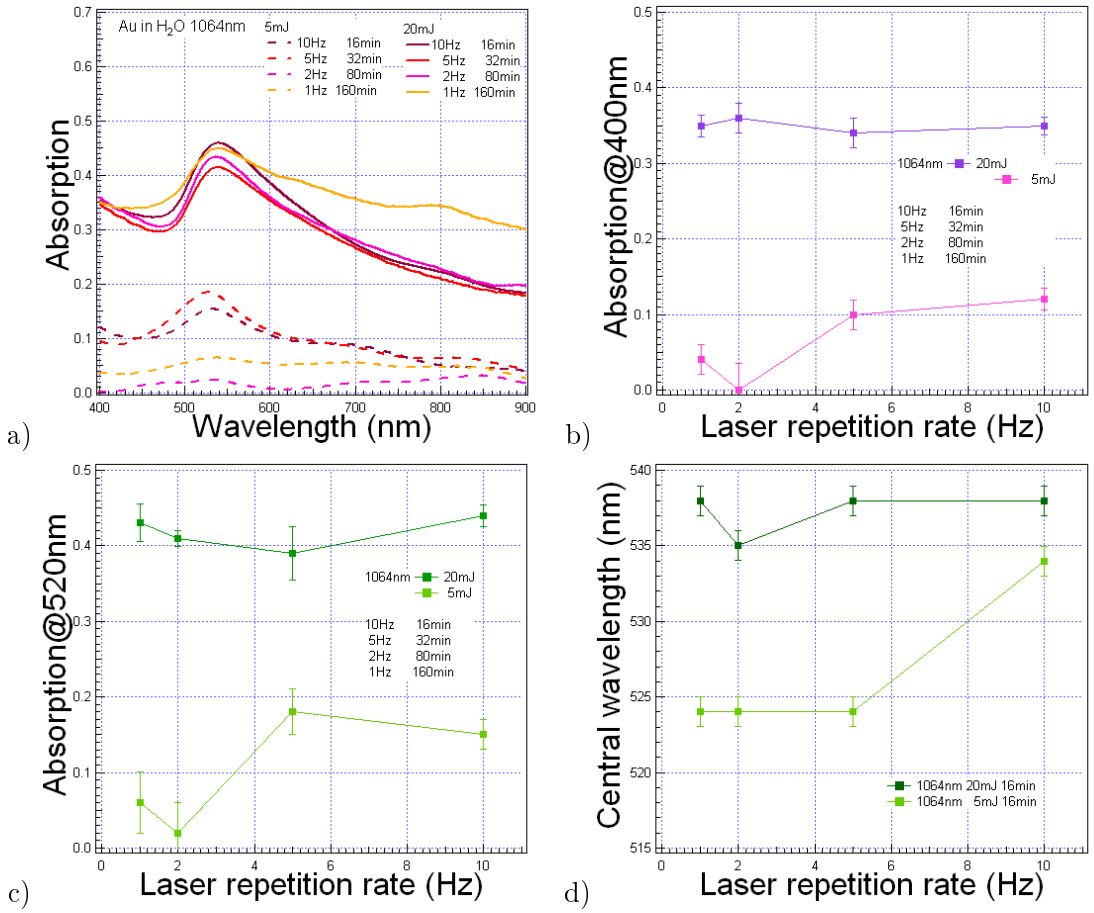

Figure 5.6: a) Absorption spectra of solutions prepared by laser ablation with 1064nm at 5mJ and 20mJ using different laser repetition rates; Absorbance at 400nm b) and 520nm c); d) Central wavelength of the plasmon band.

for all the laser repetition rates.

Fig.5.6.a presents the absorption spectra of the colloidal solutions produced by laser ablation at 1064nm at 5mJ and 20mJ. The value of A@400nm (Fig.5.6.b) reveals that the abundance of ablated gold do not depend on the laser repetition rate for 20mJ, while at 5mJ there is almost no target ablation at laser repetition rates of 1Hz and 2Hz. The absorbance at 520nm (A@520nm) (Fig.5.6.c) has a dependence on the repetition rate similar to A@400nm, at 20mJ has only a slight dependence on the laser repetition rate while at 5mJ, for 1Hz and 2Hz the A@520nm has very small values. It follows that the ablation process and the formation of nanoparticles (which exhibit the plasmon band) is more efficient with increasing the energy of the laser beam. The laser energy influences also the central wavelength of the plasmon band (Fig.5.6.d), which is red shifted for the samples made with 20mJ respect to those made with 5mJ.

To can compare the solutions made with the two laser wavelengths, the samples made with 532nm were prepared in two ways:

1. the ablation time was changed in such a way to have the same total energy of the

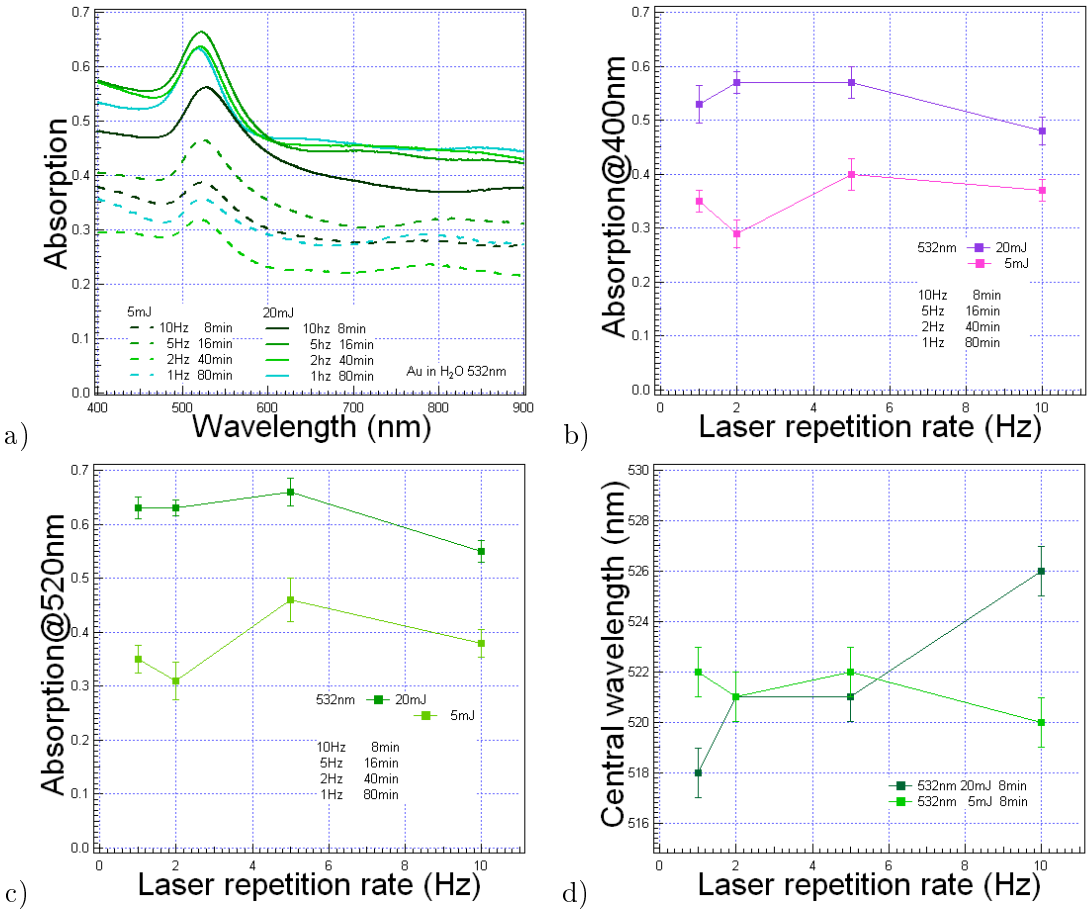

Figure 5.7: a) Absorption spectra of solutions prepared by laser ablation with 532nm at 5mJ and 20mJ using different laser repetition rates; Absorbance at 400nm b) and 520nm c); d) Central wavelength of the plasmon band.

532nm laser beam as for 1064nm, (Fig.5.7),

2. the ablation time and the laser energy[4] were the same as for 1064nm, (Fig.5.8).

Fig.5.7.a presents the absorption spectra of the samples prepared at the same total energy as for 1064nm. The A@400nm (Fig.5.7.b) varies with the laser repetition rate for both laser energies. It can be seen, comparing the Fig.5.6.b and Fig.5.7.b, that for the ablation with the same total energy, there is a greater amount of ablated gold when using 532nm than when using 1064nm; the difference is higher at 5mJ in which case the amount of gold ablated with 532nm is four times greater than for 1064nm. For 532nm at 10Hz the quantity of ablated gold in solution seams to decrease respect to the solution ablated at smaller repetition rates.

The A@520nm (Fig.5.7.c), as in the case of 1064nm, has the same dependence on the repetition rate as A@400nm. Fig.5.7.d shows the variation of the central wavelength of the plasmon band. At 20mJ the plasmon band is shifted to the longer wavelengths with increasing the repetition rate, while at 5mJ the plasmon band is centered around 521nm.

[4]The energy in mJ.

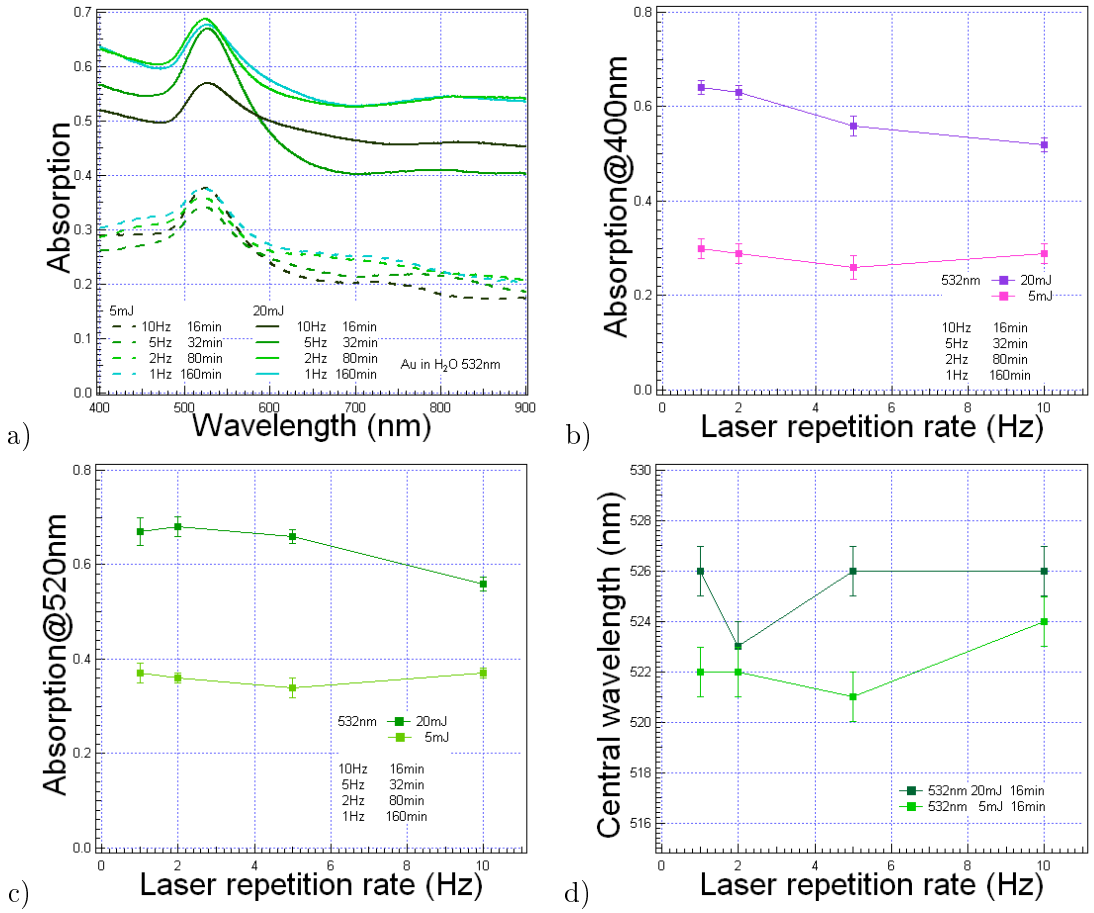

Figure 5.8: a) Absorption spectra of solutions prepared by laser ablation with 532nm at 5mJ and 20mJ, using different laser repetition rates; Absorbance at 400nm b) and 520nm c); d) Central wavelength of the plasmon band.

In Fig.5.8 are presented the results for the solutions prepared in the same conditions as for 1064nm. In this case the ablation time is two times longer than for the previous solutions made with 532nm. As can be seen in Fig.5.8.b, the quantity of ablated gold present in solution is bigger at 1Hz and decreases with increasing the laser repetition rate. The A@520nm (Fig.5.8.c), similar to the previous solutions, has the same dependence on the repetition rate as A@400nm, and from Fig.5.8.d it follows that the plasmon band is slightly red shifted when using higher laser energies.

If now we look at the values of A@400nm for the samples prepared with 532nm (Fig.5.7.b and Fig.5.8.b), we can see that for the two laser energies there is a different dependence of the quantity of ablated gold on the ablation time. At 5mJ there is a greater amount of gold in solution for shorter ablation time, and at 20mJ the amount of gold in solution is greater for longer ablation time.

The position of the central wavelength of the plasmon band (Fig.5.9) also depends on the ablation time in a different manner for 5mJ and 20mJ. At 20mJ there is a red shift (variable with the repetition rate) of the plasmon for the longer ablation time, while at 5mJ the ablation time has only a small influence on the central wavelength of the plasmon

band (except for 10Hz).

It has to be mentioned that here the absorption spectra were done immediately after the production of the colloidal solution, with the colloid in the same quartz cuvette in which it was produced, and the spectrophotometer beam passed at 1cm above the cell bottom.

For the solutions produced with 532nm the cuvette walls remained blue colored (see cuvette A in Fig.5.10) after removing the colloidal solution, which appeared less colored after transferring it in another cuvette, while the solutions produced with 1064nm left on the cuvette walls only a slightly red color (see cuvette B in Fig.5.10).

The observations relative to the ablation with 532nm:

- the decrease of the amount of ablated gold in solution with increasing the laser repetition rate,
- the decrease of A@400nm at 5mJ with the time of ablation and only a small increase of A@400nm at 20mJ with increasing the ablation time,
- the blue color left on the cuvette walls,

lead to the idea that in the case of ablation with 532nm the coalescence[5] of the nanoparticles[89] occurs leading to the formation of aggregates.

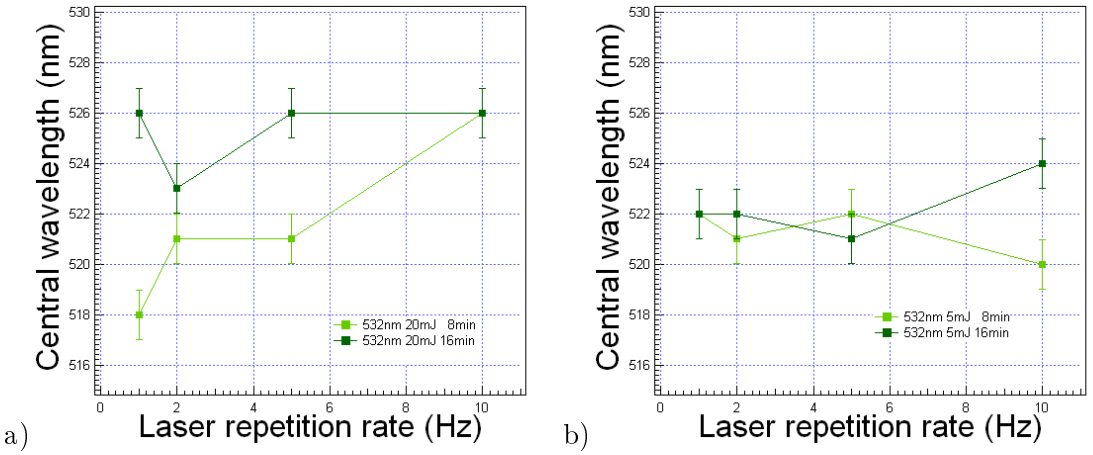

a) b)

Figure 5.9: Dependence of the position of the plasmon band central wavelength on the ablation time for ablation with 20mJ a) and 5mJ b) at 532nm.

The aggregates formation can lead to precipitation. As consequence of the precipitation, in suspensions would remain a smaller amount of ablated gold, resulting in a lower value of A@400nm. For the same total energy, at higher laser repetition rates, the quantity of ablated material in time unit is higher than at lower repetition rates, and then (as the solution is free of any stabilizer) at higher repetitions rates a greater quantity of gold

[5]Coalescence implies that the particles grow irreversibly together and form a single new particle usually containing grain boundaries.

nanoparticles will form aggregates and will precipitate resulting in a smaller amount of gold in solution.

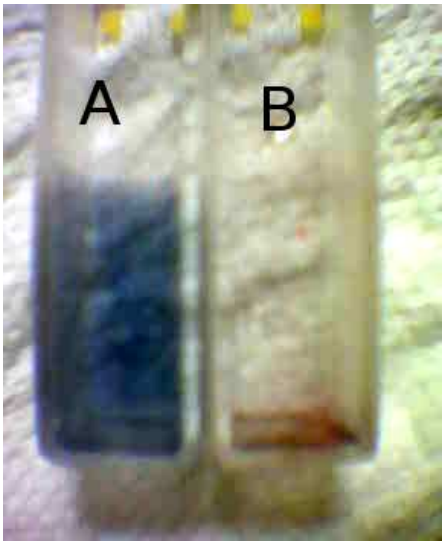

Figure 5.10: The empty cuvette after the production of the colloidal gold nanoparticles in water by laser ablation with 532nm (A) and 1064nm (B).

The TEM analysis confirms the hypothesis of aggregates formation. Fig.5.11.a shows the TEM image of a fresh solution and Fig.5.11.b and c show the TEM images of samples made with the same solution after one day. All these images reveal the presence of the coalescence aggregates: smaller aggregates in the case of the fresh solution, and more extended aggregates for the one day solution. In both cases, the aggregates are formed by spherical gold nanoparticles connected with metallic bounds.

Fig.5.12 present SEM images of gold aggregates supported on a tantalum foil, prepared by evaporating 5ml of colloidal solution produced with 532nm at 10Hz, 50mJ, and 5min ablation time. It follows that uncapped gold nanoparticles produced by laser ablation in doubly deionized water form aggregates with web-like structures (Fig.5.12.a) when the water is evaporated.

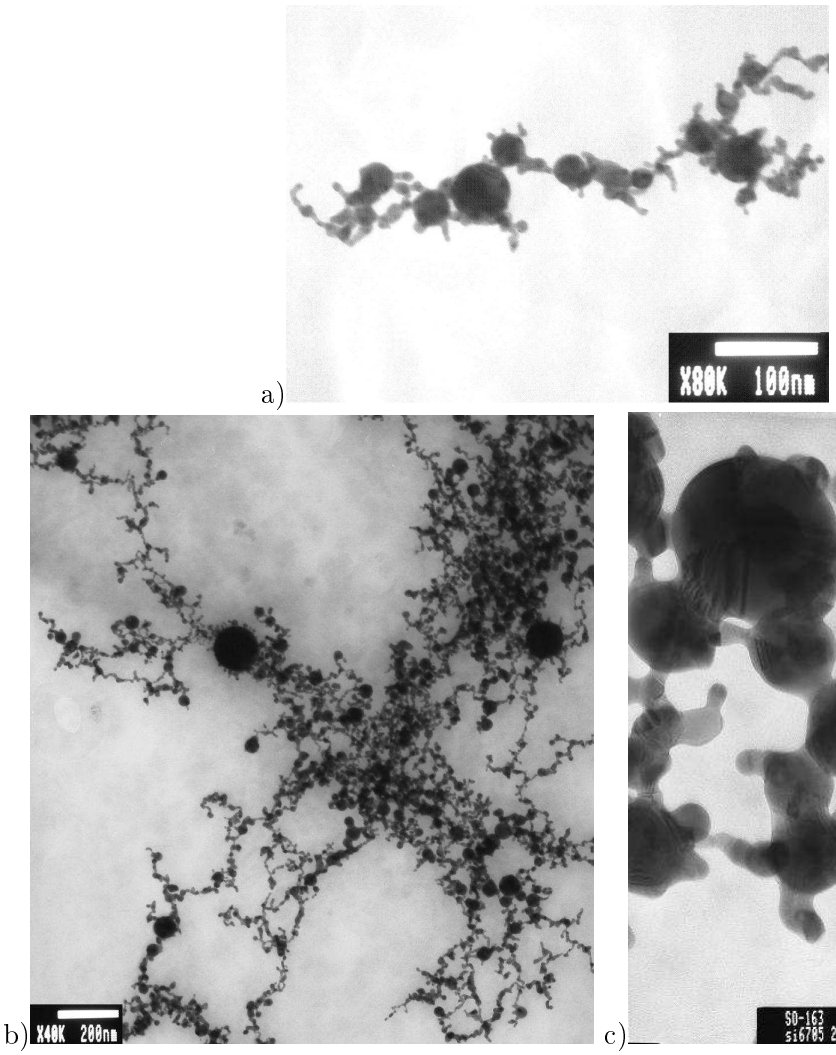

Figure 5.11: TEM photos of Au nanoparticles in H_2O produced by laser ablation with 532nm 10Hz 20mJ 10min: a) fresh colloidal solution, b) at 24 hours after the production of the colloid, and c) detail of b).

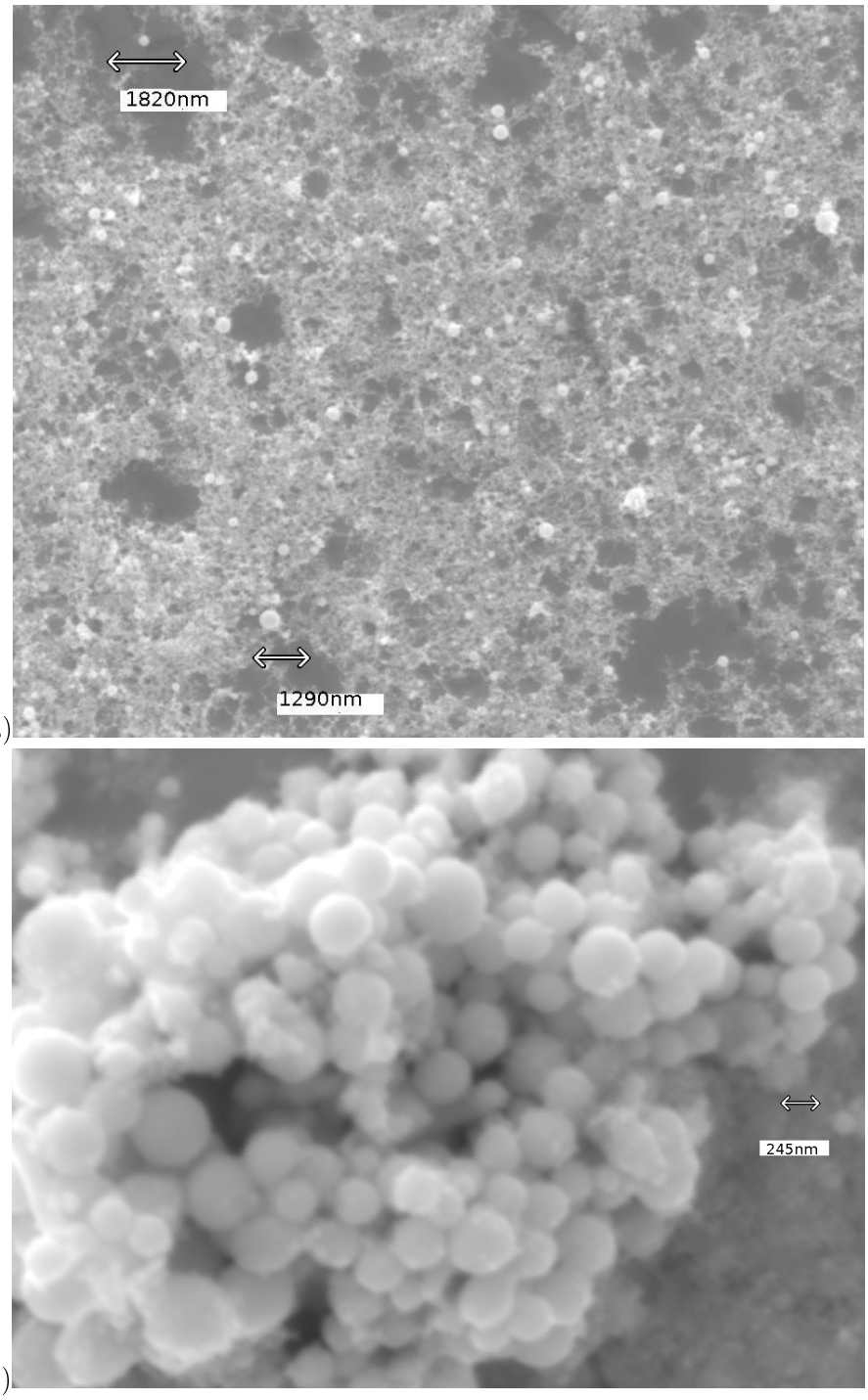

a)

b)

Figure 5.12: SEM images of gold aggregates supported on a tantalum foil: a) web-like structure, b) aggregate of big nanoparticles.

5.2.2 Discussion

These first experiments on production of colloidal gold nanoparticles by pulsed laser ablation in doubly deionized water, have shown the following:

- it is possible to produce colloidal gold nanoparticles with spherical shape by picosecond laser ablation of a gold solid target in doubly deionized water;
- the nanoparticles revealed to be unstable, specially those produced with 532nm: they aggregate quickly even during their production resulting in a blue color solution (Fig.5.13);

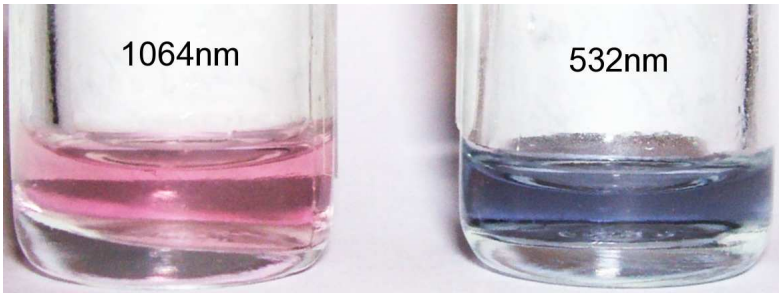

Figure 5.13: Colloidal gold in deionized water produced by ablation with 1064nm and 532nm.

- the different characteristics (colors and stability) of the solution produced with 532nm and those produced with 1064nm indicates that the laser wavelengths could have an important role for the process of nanoparticles formation.

The fact that the nanoparticles produced with the laser wavelength of 532nm are subjected to early aggregation can be explained on the basis of Derjaguin-Landau-Overbeek-Verwe theory (DLOV)[90]. This theory describes the mechanism which allows to keep the hydrosols[6] in a metastable (without aggregation) state for months. It considers that the total interaction potential, V_{tot}, between neighbouring clusters is achieved by superimposing the attractive Van der Waals potential and a repulsive electrostatic potential (due to electrical charging of the cluster), screened by clouds of ions.

When the screening length[7] $\kappa^{-1} = \left[e^2 \sum n_i(\infty) z_i / \varepsilon_0 \varepsilon \kappa_B T\right]^{-1/2}$ (where n_i and z_i are the concentration and the valences of the ions in electrolyte) and the surface distance d between the two spheres are smaller than the particle radii R, V_{tot} can be approximated by the following expression:

$$V_{tot} = -\frac{A}{12}\frac{R}{d} + 4\pi\varepsilon_0\varepsilon R V_0^2 \frac{d}{d+2R}\left[1 + \frac{R}{R+d}e^{-\kappa d}\right], \tag{5.1}$$

[6] A hydrosol is a colloid with water as the dispersing medium.

[7] The screening length is functions of: ions charge, ionic concentration, dielectric constant of the solvent, and temperature.

where the first term represents the Van der Waals contribution, the second one gives the electrostatic Coulomb potential, A is the Hamaker constant (described below) and V_0 is the surface potential.

This pair potential, at proper values of A and κ, exhibits a potential barrier which stabilizes aqueous colloidal systems, provided its height exceeds markedly the energy of thermal motion of the colloidal clusters. If the barrier is reduced below the thermal energies, the particles immediately are led to aggregation. There are two ways to modify the potential barrier , one is by changing the ions concentration[8] which would modify the κ value and then the potential barrier (Fig.5.13.a), and the second one is to increase the attraction force.

It has to be mentioned that the DLOV theory do not considers the mechanical barriers, given by ions and molecules adsorbed at the cluster surface, and hydrodynamical forces, which both may prevent particles from coalescence, then remaining in the state of coagulation.

In the photo-induced coagulation, the concentration and the type of electrolyte species, if they exist, of the colloid solution remain unchanged before and after the irradiation of light [91]. It results that the interparticle potential energy drastically decreases due to an enhancement of the van der Waals force causing spontaneous coagulation among particles in close proximity. Hence, the whole process should be governed by the enhancement of the van der Waals force induced by the irradiation; in our case laser irradiation.

When the colloid is irradiated at Mie resonance frequency, there is a photoinduced electric dipole [91] given by:

$$\mu_{irr} = \alpha\left(R, \omega_M\right) E\left(\omega_M\right), \tag{5.2}$$

where $\alpha\left(R, \omega_M\right)$ is the particle polarizability and $E\left(\omega_M\right)$ stands for the external electric field at the Mie resonance frequency ω_M.

For weak-intensity light sources, the number of particles absorbing at the Mie resonance is very small, leading to only one exciting particle being surrounded by other ground state particles which are perturbed by the photoinduced electric dipole (5.2). The induced electric dipole moment on the surrounding particles is approximately given by:

$$\mu_{ind} = \mu_{irr}\alpha_0/d^3, \tag{5.3}$$

where α_0 is the static polarizability of a particle. Then the dipole-induced dipole interaction leads to an energy interaction between particles given by:

$$U_{irr} = -\frac{\mu_{irr}\mu_{ind}}{d^3} = -\frac{\alpha\left(R, \omega_M\right)^2 \alpha_0 E^2\left(\omega_M\right)}{d^6}. \tag{5.4}$$

[8]When one adds salt to colloid dispersion, particles spontaneously aggregate as a result of the reduction of the thickness of the electrical double layer (corresponding to the increment of electrostatic screening effect by ions). In this case, one can control the electrostatic potential by the concentration and by the valence of electrolytes (Schulz-Hardy rule).

The Hamaker constant A, is connected with the interparticle interaction energy U, by [91]:

$$A = Ud^6\pi^2\varsigma^2, \tag{5.5}$$

where ς is the atomic number density of a particle. When the nanoparticles are irradiated $U = U_{irr}$. Since U is proportional to d^{-6} it follows that A is independent of the distance between particles.

The ratio of the interaction energy under irradiation (at low radiation power) at the Mie resonance frequency, U_{irr} and the interaction energy under "dark" conditions (without irradiation) U_d is given [91] by:

$$\frac{U_{irr}}{U_d} = \frac{16\alpha_0 E^2}{27\hbar\omega_M}\left(-\frac{R}{D_M}\right)^2, \tag{5.6}$$

where D_M is the centroid of the surface screening charge at the Mie resonance frequency. The ratio[9] $\frac{R}{D_M} \sim 100$ and the average energy ratio $\frac{\langle\alpha_0 E^2\rangle}{\hbar\omega_M}$ is of the order of $10^{-3} \div 10^{-2}$ for a conventional light source and 1 for a laser source. Hence, $\frac{U_{irr}}{U_d}$ becomes $10 \div 100$ for a conventional light source and 10^4 for a laser. It follows that the interaction potential is enhanced by at least one order in magnitude when particles are illuminated by the Mie resonance frequency. This enhancement is accentuated by the use of a laser source. Moreover, the larger the particles, the larger ratio $\frac{R}{D_M}$ becomes, giving much stronger interaction among particles.

Since the Hamaker constant A is directly related to U (5.5), the irradiation at the Mie resonance frequency increases the value of A.

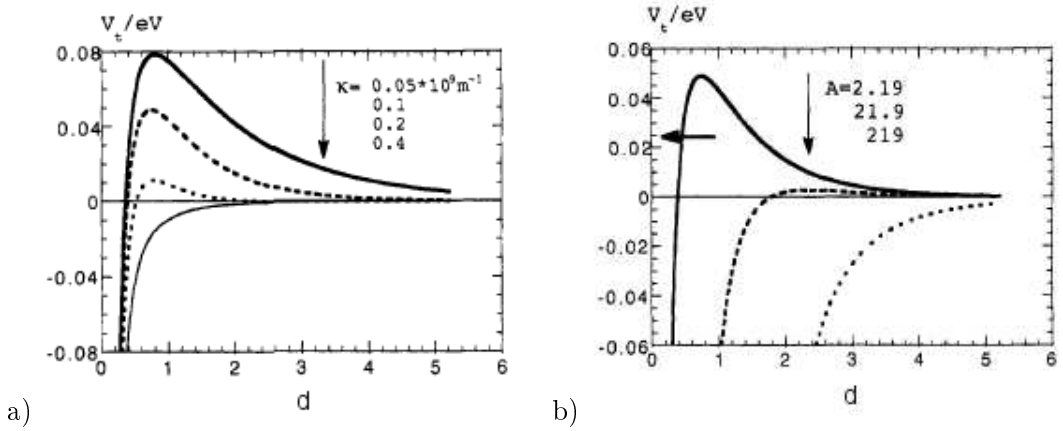

Figure 5.14: The total interaction potential as function of interparticles distance for different values of: a) κ, b) A from dark condition 2.19eV to low power irradiation 219eV [91].

Fig.5.14 shows the changes in the interaction potential due to the values enhancement of the screening length κ^{-1} (Fig.5.14.a) and of the Hamaker constant A (Fig.5.14.b). The peak

[9]Considering the values: $R = 10nm$ and $D_M = 0.1nm$.

of a barrier in the figure does not almost shift for the change in the screening length κ^{-1}, while in the change of the Hamaker constant, the energy barrier shifts apparently toward longer distance causing a long-range attractive force, and finally the barrier disappears. It follows that the interaction potential seems to have a long-range attractive force via the irradiation.

Then the excitation of the plasmons resonances of the nanoparticles by the absorbed light results in additional attractive forces via induced electromagnetic multipolar interactions. Moreover, Ref.[92] shows that there is a threshold laser power for which the photoinduced aggregation takes place, meaning that the photoinduced aggregation is caused by a nonlinear process.

5.3 Production of gold nanoparticles in aqueous solution of SDS

5.3.1 Experimental results

As known from literature[75], one of the factors which determines the final size of the nanoparticles produced in SDS aqueous solution is the concentration of SDS. The critical value of the SDS concentration for which the nanoparticles are stabilized is very close to the SDS critical micelle concentration (0.008 M, in pure water at 25°C) [19, 33], and the maximum stability of gold nanoparticles produced by laser ablation in aqueous solution of SDS is reached for a concentration of 0.1M [75].

Fig.5.15 shows an evidence for the influence of the SDS concentration. In the absorption spectra of the colloidal solution with a 0.04M concentration of SDS (Fig.5.15, blue line), the plasmon band is almost absent, while for the solution with concentration of 0.1M SDS (Fig.5.15, green line), the plasmon band is clearly evidenced. Moreover, for the second sample A@400nm is 2 times higher meaning that the amount of gold in solution is significantly greater. These observations lead to the conclusion that a greater number of nanoparticles are stabilized by the SDS molecules and remain in suspension.

Fig.5.16.a, b, and c present TEM images of colloidal gold nanoparticles produced by 16min ablation with 1064nm 10Hz 15mJ in 0.02M SDS. The produced nanoparticles have spherical shape and are well separated one from the other.

Fig.5.16.d presents the size-distribution diagram of the nanoparticles diameter (measured using the Image J software). While the TEM photos (Fig.5.11) of nanoparticles produced in doubly deionized water present aggregates formed by nanoparticles of tens

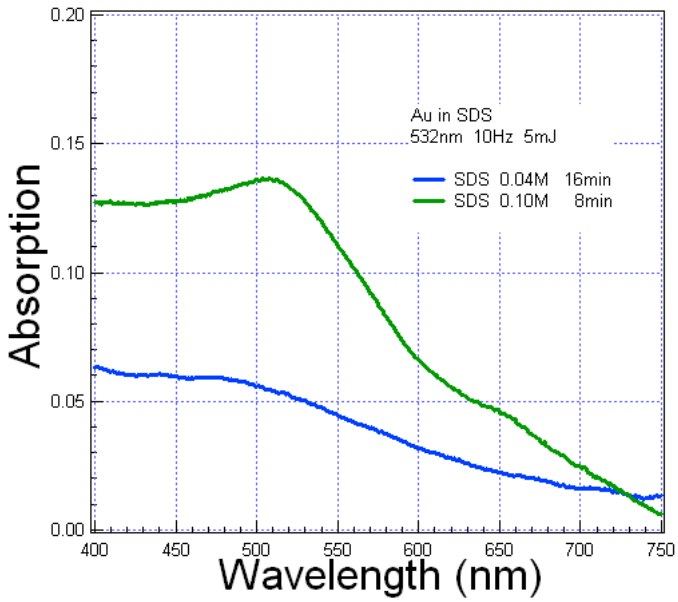

Figure 5.15: Absorption spectra of colloidal gold nanoparticles in aqueous solution of two different SDS concentrations.

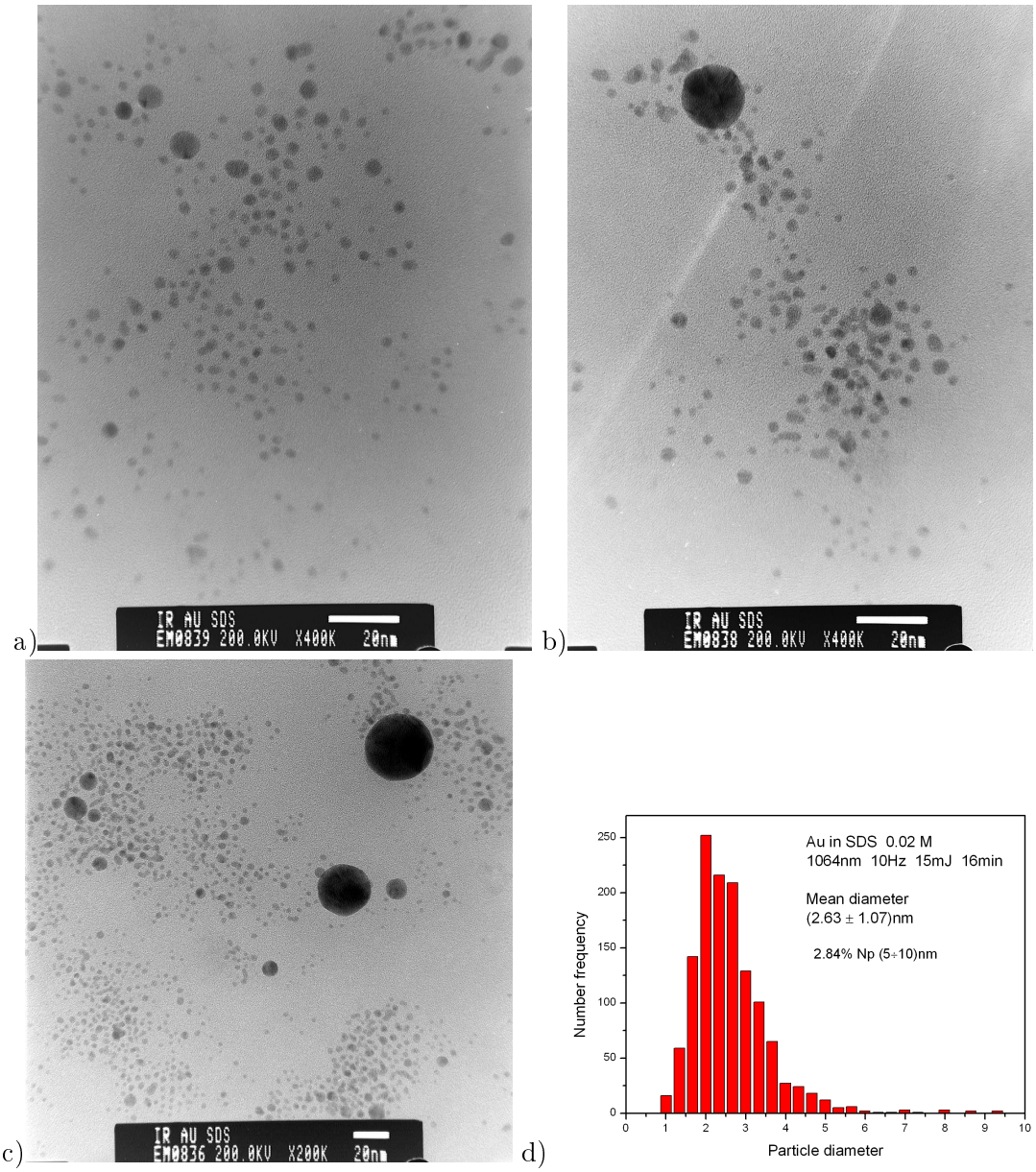

Figure 5.16: a), b), and c) TEM images of the same colloidal solution of gold nanoparticles produced by 16min ablation with 1064nm 10Hz 15mJ in 0.02M SDS, and d) Size distribution of the nanoparticles diameter measured using the Image J software.

and hundreds of nanometers, in SDS solution (Fig.5.16) the mean diameter of the gold nanoparticles results to be 2.63nm±1.07nm, and only less than 3% of the nanoparticles have diameter greater than 5nm. It follows that the use of SDS leads also to the reduction in the diameter of the produced nanoparticles.

Compared with the results reported in the literature[20] for the nanosecond laser pulses at 1064nm, we obtained using the picosecond laser at 1064nm in 0.02M aqueous solution of SDS a reduction with 70% of the mean diameter of the nanoparticles. From the results of the same author it follows that the mean diameter is reduced to 1.7nm when using the 532nm laser wavelength in 0.05M aqueous solution of SDS, which represents a reduction

of with 80%.

To monitor the ablation process and the formation of nanoparticles which exhibit the plasmon band absorption, the transmission T of a low power beam at 514.5nm (T@514.5nm) from an Ar laser was registered on-line. The wavelength of 514.5nm was chosen because it is in the vicinity of the central weavelength, 520nm, of the gold nanoparticles plasmon band and its absorption gives a direct information on the process of nanoparticles formation.

Fig.5.17 shows the T@514.5nm during the ablation with 1064nm (red line) and with 532nm (green line) at the same total energy (in eV). For 1064nm T@514.5nm has almost exponential decay, until 16000 laser shots when it reaches the zero. For 532nm, in the first 1000 laser shots T@514.5nm perfectly follows the same trajectory as for the 1064nm, then it starts having an oscillatory behaviour and finally, after 9000 laser shots, it sets to a constant value.

This measurement clearly shows that there is a different action of the two laser wavelengths, i.e.:

- for 1064nm the target is continuous ablated, leading to the formation of an increased number of gold nanoparticles which exhibit the plasmon band and in consequence absorb the 514.5nm,
- for 532nm the ablation and the subsequent formation of the nanoparticles seems to take place only in the first 3000 laser shots.

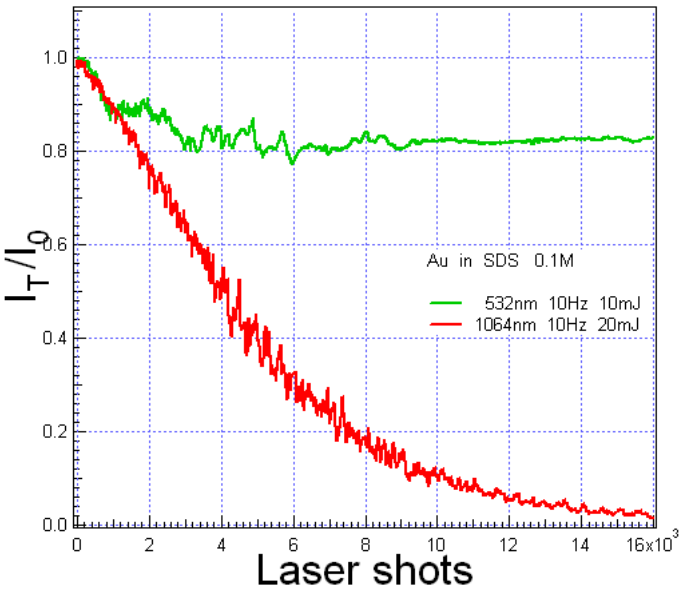

Figure 5.17: On-line monitoring of T@514.5nm during the production of two colloidal gold solution in SDS 0.1M by ablation with 532nm (green line) and 1064nm (red line) at the same total energy.

To determine the influence the ablation wavelength and of the other laser parameters on the process of ablation and on the formation of nanoparticles, various transmission

measurements were done for both laser wavelengths at different energies and repetition rates. In Fig.5.18 is presented the on-line monitoring of T@514.5nm during the production of colloidal gold solution in SDS 0.1M by ablation: at different laser energies (Fig.5.18.a and b) and at different laser repetition rates (Fig.5.18.c and d) for both laser wavelengths.

The on-line measurements presented in Fig.5.18.a show that the ablation with 532nm in SDS solution takes place only when the laser energy is at least 5mJ. Ablating the target at different energies (≥5mJ) of 532nm (Fig.5.18.a) does not change too much the number of laser shots (around 1000) where the oscillatory behaviour starts, but it changes the number of shots after which the constant value sets in. Moreover, the final value of the T@514.5nm scales down with increasing laser beam energy: 0.8 at 5mJ, 0.6 at 10mJ and 0.45 at 15mJ.

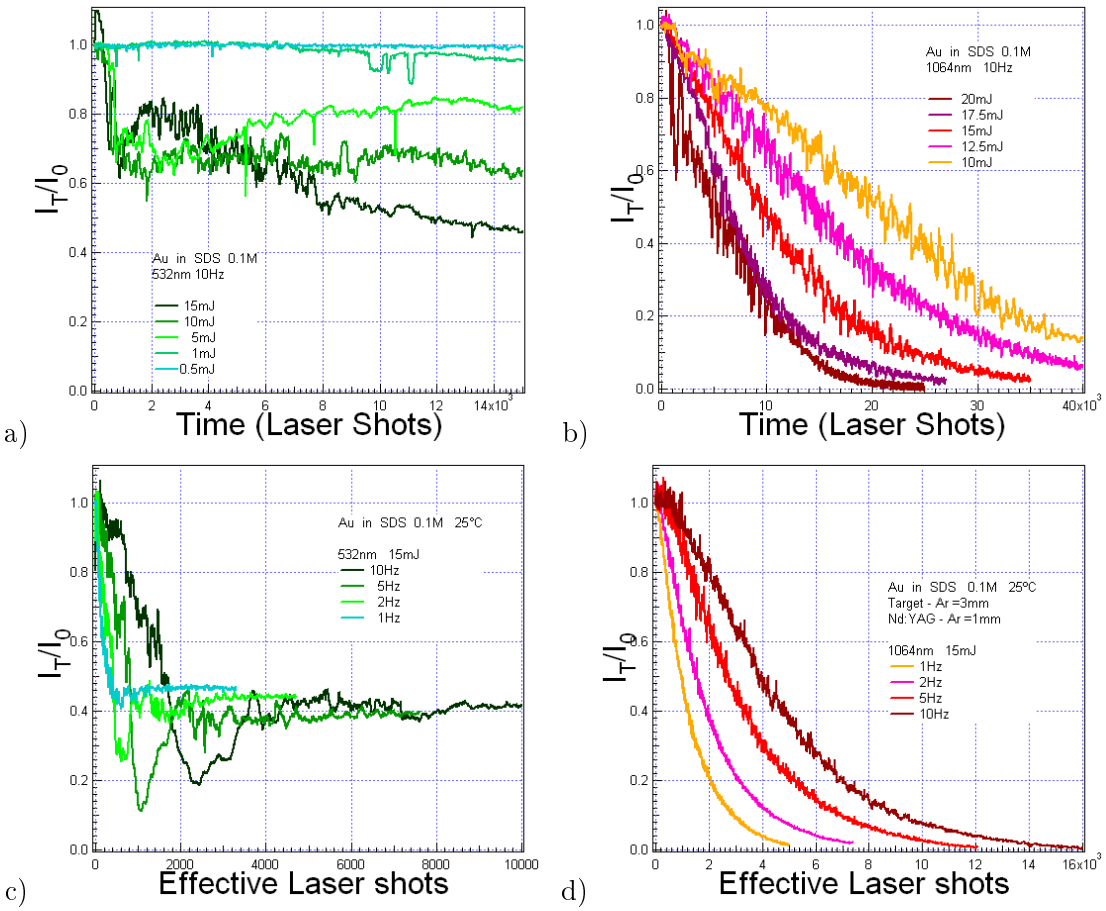

Figure 5.18: On-line monitoring of T@514.5nm during the production of colloidal gold solution in SDS 0.1M by ablation: at different laser energies of a) 532nm, b) 1064nm, and at different laser repetition rates of c) 532nm, d) 1064nm.

The T@514.5nm, around 1000 shots presents an initial minimum after which the oscillatory behaviour starts. When the energy of the ablation laser beam is increased to 15mJ, the final constant value of T@514.5nm becomes lower than the value of the initial minimum. This means that during the oscillatory behaviour, at 15mJ the ablation process continues, while at 5mJ and 10 mJ there is no further ablation of the target (due to the

absorption of 532nm by the formed nanoparticles) after the first minimum is reached.

For 1064nm (Fig.5.18.b), when the laser energy is increased, the number of laser shots (and then the ablation time) needed to arrive at complete absorption of the 514.5nm decreases. This behaviour lead to the conclusion that for 1064nm both, the ablation rate and the number of nanoparticles formed in unit time increase as the laser beam energy increases.

Fig.5.18.c presents the measurements at different repetition rates for the same laser energy of 532nm. The number of laser shots at which the initial minimum of T@514.5nm is reached increases with the increase of laser repetition rate (500 shots at 1Hz, 2100shots at 10Hz). The value of the initial minimum changes with the repetition rate and seams to have an oscillatory behaviour attaining a smaller value at 5Hz. The final constant value of T@514.5nm is slightly lower with increasing the laser repetition rate (0.46 at 1Hz, 0.43 at 2Hz and 0.4 at 5Hz and 10Hz).

It follows that changing the repetition rate for 532nm influence only the way which T@514.5nm evolves until its final value, letting the later almost unchanged (for the given laser energy).

In the case of 1064nm (Fig.5.18.d) changing the laser repetition rate lead only to a change of number of the laser shots needed to reach the zero of T@514.5nm. This change corresponds to a longer ablation time for lower repetition rates.

As a further step, we have studied the dependence of the nanoparticles production on the temperature. The temperature of the solution was initially set to a fixed value, between $10°C$ and $+50°C$, using the Peltier cooler system (Fig.5.2), and was maintained constant during the laser ablation of the target. The upper limit of the temperature is due to the Peltier system and the lower limit is $10°C$ because is not to far from the Krafft temperature[10] of SDS in water.

In the case of ablation with 532nm (Fig.5.19.a, c, d), the variation in temperature (in the investigated range) do not changed the final constant value of T@514.5nm, but changes the value and the position its first minimum (Fig.5.19.c). For lower temperatures the value of minimum T@514.5nm is smaller and is reached after a major number of laser shots (at $10°C$ it is 0.18 reached after 3000 shots, and 0.26 reached after 1800 shots at $50°C$).

For the samples produced by ablation with 1064nm (Fig.5.19.b), the lowering of the solution temperature implies a slower decrease of T@514.5nm (Fig.5.19.d) and an increase of the number of laser shots needed to reach the complete 514.5nm absorption by the solution.

5.3.2 Discussion

From the above presented results, it follows that:

- the use of SDS not only prevent the nanoparticles aggregation but leads also to reduction of their diameters (respect to the production in deionized water),

[10]The Krafft temperature is the minimum temperature at which the surfactant form micelle.

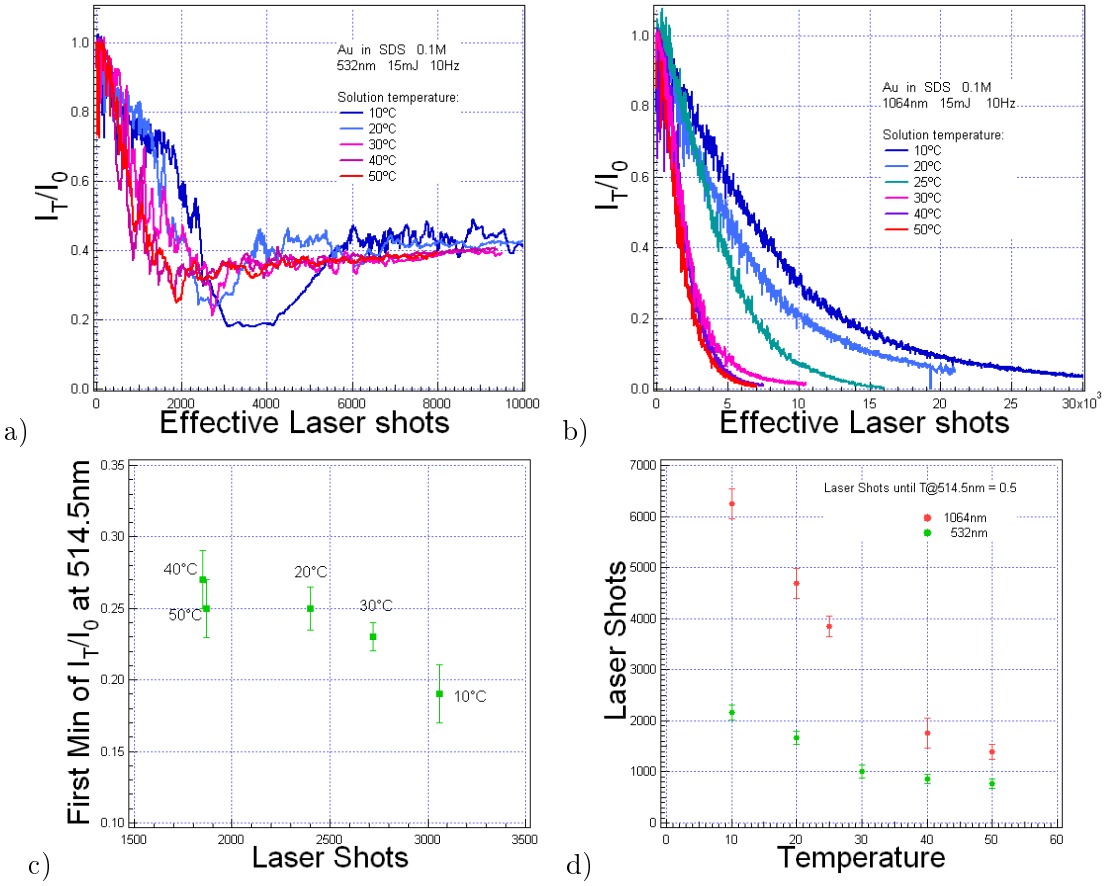

Figure 5.19: The temperatures influence on T@514.5nm during the production of colloidal gold in 0.1M SDS solution by ablation with a) 532nm, b) 1064nm, c) value of first minimum of I_T/I_0 as function of temperature and laser shots, d) evolution of number of laser shots needed to arrive at $I_T/I_0 = 0.5$ as function of temperature.

- the on-line monitoring of T@514.5nm revealed different mechanisms of ablation and subsequent formation of nanoparticles for the 1064nm and 532nm,
- for the 1064nm the laser energy and the repetition rate influence only the velocity of the ablation process and formation of nanoparticles, while for 532nm, in particular the energy variation, has more complex consequences,
- the change of the temperature of the solution seems to influence the formation of nanoparticles exhibiting the plasmon band.

In fact, increasing the temperature of the SDS solution from $10°C$ to $50°C$, leads to a faster decrease of T@514.5nm. As the absorption of 514.5nm is supposed to be proportional to the number of nanoparticles exhibiting the plasmon band, it follows that with increasing the temperature, the rate of production of these nanoparticles is increased.

These observations on temperature effect on the evolution of T@514.5nm could be explained by a combined action of the solution viscosity and gold and SDS concentration in the volume, V, over the target surface where the formation of the nanoparticles take

place.

The viscosity μ of water is $8.9 \times 10^{-4} Pa \cdot s$ at 25°C and as a function of temperature: $\mu = A \times 10^{\frac{B}{(T-C)}}$, where $A = 2.414 \times 10^{-5} N \cdot s/m^2$, $B = 247.8\ K$ and $C = 140\ K$. It follows that at lower temperatures the solution viscosity increases and the nanoparticles will have a reduced mobility.

We suppose the quantity of ablated gold in unit time is the same for all temperatures. Then at $10°C$ we will have the followings:

- the viscosity is increased respect to its value at $25°C$, leading to a reduced mobility of the ablated species,
- the concentration of saturation of gold is lower than at $50°C$ (see Section 3.2),
- the temperature is lower than the Krafft temperature, T_M, which for SDS in water is $12C$ [93], and hence the SDS could not form micelle.

In this conditions, at $10°C$ the ablated species and the formed particles will remain a longer time in the volume V and the gold concentration will be increased by the continuous introduction of ablated gold. The shortage of SDS can occur, due to the reduced diffusion[11] of SDS molecules towards the V volume. In this way, the high concentration of gold and the reduced protective action of SDS (due to both, the reduced concentration and the absence of micelle formation) could lead to formation of bigger and unprotected nanoparticles. These particles can aggregate and then to precipitate. In this way in solution remain a smaller quantity of gold nanoparticles exhibiting the plasmon band, and this would explain the reduced absorption of 514.5nm.

Increasing the temperature at $50°C$ will lead to:

- an increased mobility of the nanoparticles due to reduction of the solution viscosity with the temperature increase,
- a higher value of the concentration of saturation for gold, respect to its value at $10°C$.

At $50°C$, the reduced solution viscosity allows to the ablated species and the formed particles to leave in a shorter time the volume V, and to be avoided the shortage of SDS molecules. In this way the gold concentration in the volume V will not increase to fast respect to the SDS concentration, and because the temperature is higher than the T_M, the protective action of SDS would be maximal for the concentration used in the experiment (see Section 4.1.1). In this way the gold precipitation is avoided leading to an increased quantity of gold in suspension and an accentuated absorption at 514.5nm for the same number of laser shots as at $10°C$.

[11] The reduce diffusion of SDS molecules is also due to the increased viscosity of the solution.
During the experiments at temperatures lower than T_M a transformation of SDS solution to a gelatin-like consistence could be seen.

For the solutions produced by ablation with 532nm, the increase of T@514.5nm after reaching the initial minimum reflects a reduction of the number of nanoparticles exhibiting the plasmon band. A possible explication of this is the size reduction of the nanoparticles exhibiting the plasmon band by the intense laser beam at 532nm (see Section 4.2). The fact that T@514.5nm sets at the constant value means that the rate of nanoparticles fragmentation equals that of aggregation of smaller fragments and the average diameter of the nanoparticles reach its minimum value.

The size reduction effect of the 532nm also explain the step-like decrease of T@514.5nm for the low temperature solutions produced with 532nm.

To be sure that the explanation proposed above is the right one, further investigations have to be done on the temperature influence on the SDS solution in the absence of the particles production and how these changes of the solution affect the laser energy reaching the gold target.

5.4 Gold nanoparticles produced by laser ablation in aqueous solution of PAMAM G5

We investigated the production of gold nanoparticles by laser ablation in aqueous solution of ethylendiamine-core poly(amidoamine) (PAMAM), because it has already been successfully used for the chemical preparation of metal-dendrimer nanocomposites. In spite of its efficiency and versatility as stabilizing agent, up to now, its role in the nanoparticles production by laser ablation has never been studied.

The interest in studying the nanoparticles production by laser ablation in PAMAM solution is increased by the fact that the PAMAM has already been demonstrated to behave either as a conventional stabilizer for metal nanoparticles or as a nanoreactor, thanks to its ability to encapsulate small metal clusters or metal ions[94]. In the present work, this PAMAM's property was exploited to investigate the production mechanism of the nanoparticles [95] and their photo-stability.

This chapter describes the production of gold nanoparticles by picosecond laser ablation with 532nm and 1064nm laser wavelengths, in aqueous solution of PAMAM G5 (Fig.5.20). According to tabulated values provided by the producer, PAMAM G5 is a monodisperse compound, having a molecular diameter of 5.4nm. The solutions were 3.8mM, referred to superficial amino groups, and were obtained by dilution of 22.2% aqueous solution of PAMAM G5 from Dendritech® with doubly deionized water (18.2 MO.cm @25°C). This molar concentration lead to a concentration of PAMAM molecules of $10^{16}\frac{molecules}{cm^3}$.

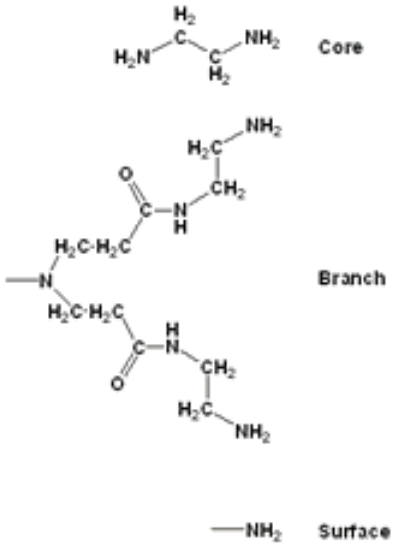

Figure 5.20: Core, branch, and surface components of PAMAM G5.

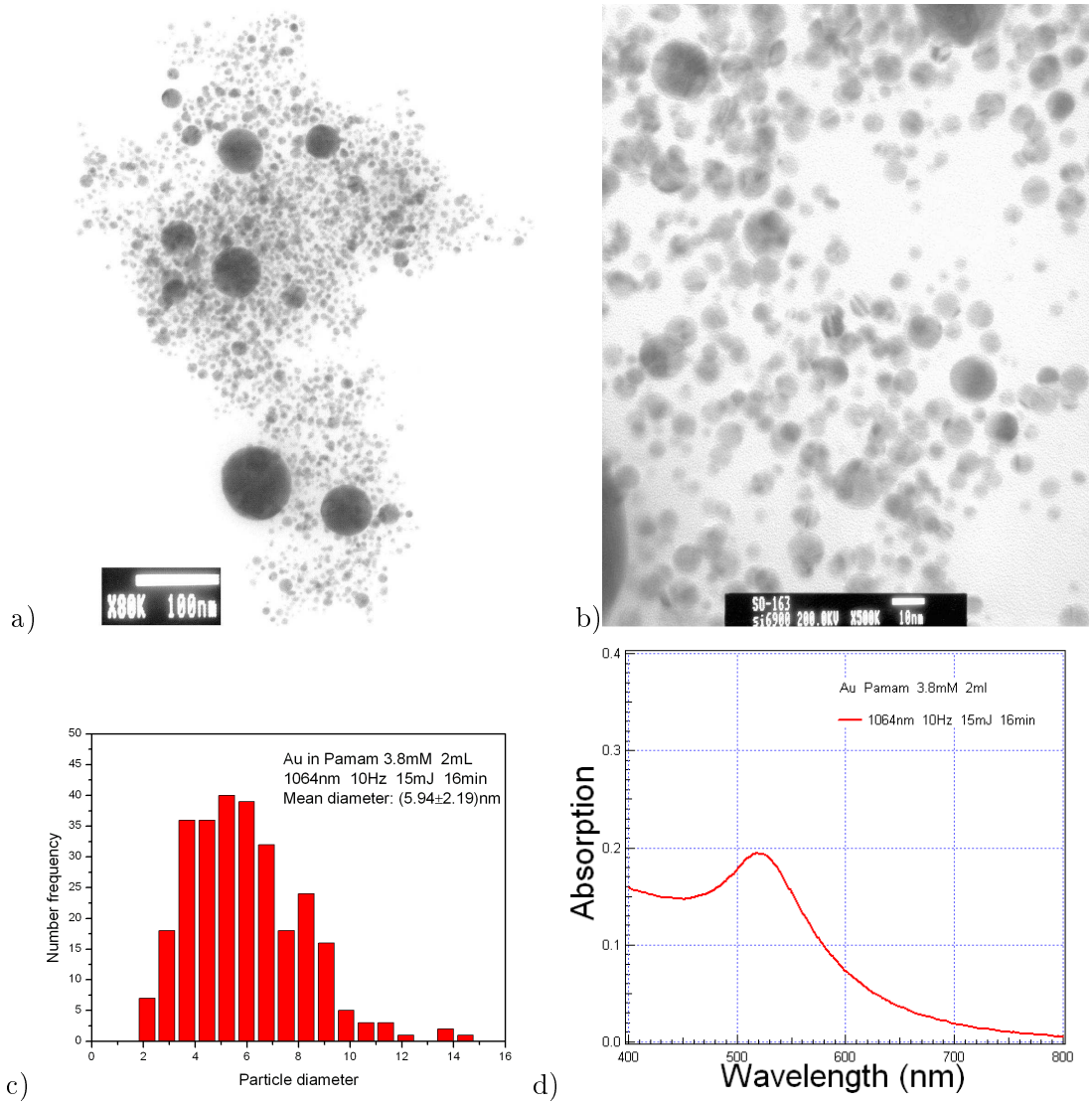

Figure 5.21: Colloidal solution produced by laser ablation with 1064nm in 3.8mM aqueous solution of PAMAM G5: a) TEM image of gold nanoparticles, b) detail of a), c) the size distribution , and d) absorption spectra.

5.4.1 Experimental results

The Fig.5.21.a and b show TEM images of gold nanoparticles in aqueous solution of PAMAM G5, made several weeks after the solution preparation. It is clearly seen, that the gold nanoparticles produced with 1064nm in aqueous solution of PAMAM G5 are isolated one from another, with a mean diameter of about 6nm and a relatively broad size-distribution (see Fig.5.21.c), and they do not form aggregates. The absorption spectra (Fig.5.21.d) present the characteristic band around 520nm, which is associated with plasma oscillations of gold nanoparticles conduction electrons.

Confronting the nanoparticles produced at 1064nm and 532nm (at the same laser parameters) (Fig.5.22) is evident the effect of size reduction by the use of the 532nm laser

a)

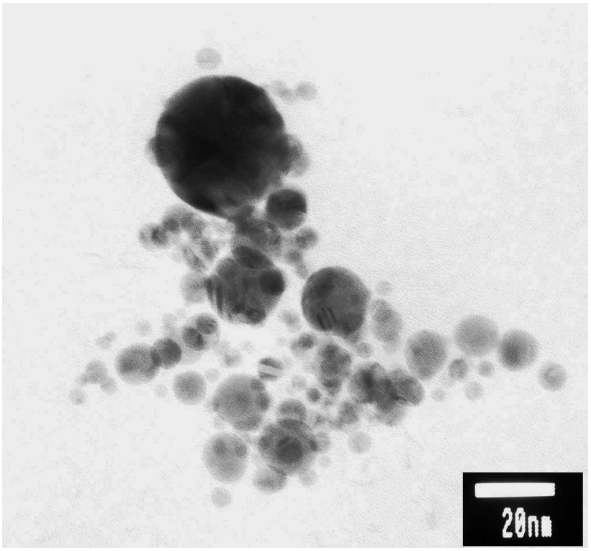

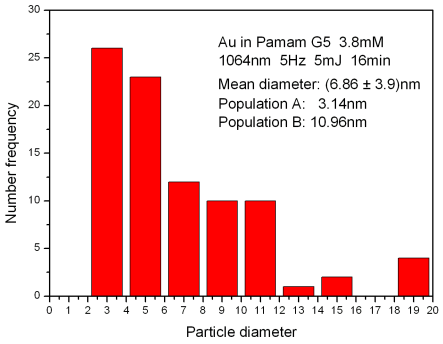

b)

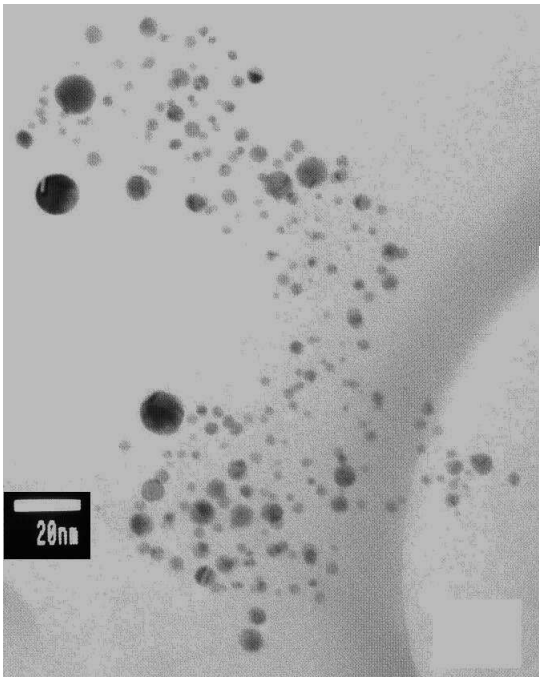

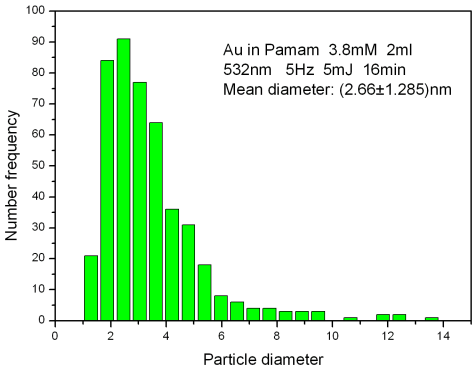

Figure 5.22: TEM photos and size distribution of colloidal gold in PAMAM 3.8mM produced by ablation with: a) 1064nm 5Hz 5mJ 16min, b) 532nm 5Hz 5mJ 16min.

beam. While for the colloids produced by ablation with 1064nm (Fig.5.22.a) the mean diameter of the nanoparticles is 6.8nm with standard deviation 3.9nm, for 532nm (Fig.5.22.b) the mean diameter is reduced at 2.6nm with a standard deviation of 1.3nm.

Fig.5.23 presents the absorption spectra of the two colloidal solutions showed in Fig.5.22. The plasmon band is present in both cases. In the spectra corresponding to the solution produced with 532nm the plasmon band is weaker and there is an intense absorption band at 290nm.

The band at 290nm was never observed for the solutions of gold nanoparticles produced by ablation with 532nm in water or aqueous solutions of SDS and is missing also from the

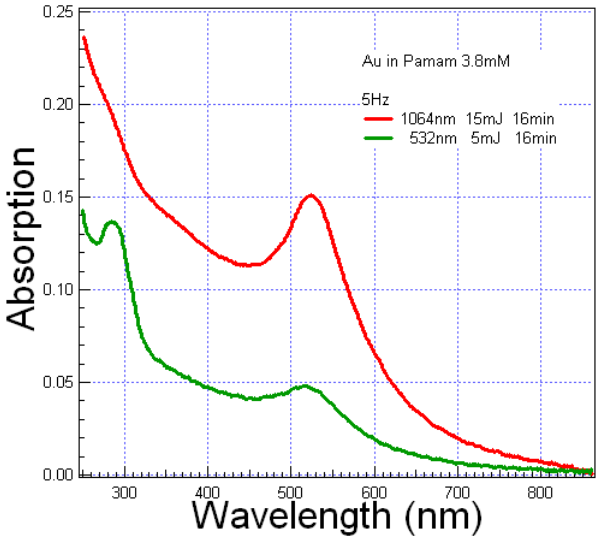

Figure 5.23: Absorption spectra of colloidal gold in PAMAM 3.8mM produced by ablation with 1064nm (red line) and 532nm (green line).

absorption spectra of the colloidal solutions in PAMAM G5 produced by ablation with 1064nm (Fig.5.23). For these reasons the presence of the band at 290nm is thought to be due to the combined effect of 532nm ablation and use of PAMAM G5 [96].

In order to clarify the origin of the 290nm absorption band, we prepared colloidal solutions by ablation at the same parameters of 532nm in water and in SDS solution. Moreover, a 3.8mM PAMAM solution was irradiated with 532nm in the absence of the gold target, with the purpose to verify if the 290nm band originates from the degradation of the PAMAM G5 molecules under the action of the laser beam. As it can be observed in Fig.5.24, the 290nm band is missing from all absorption spectra of this solutions.

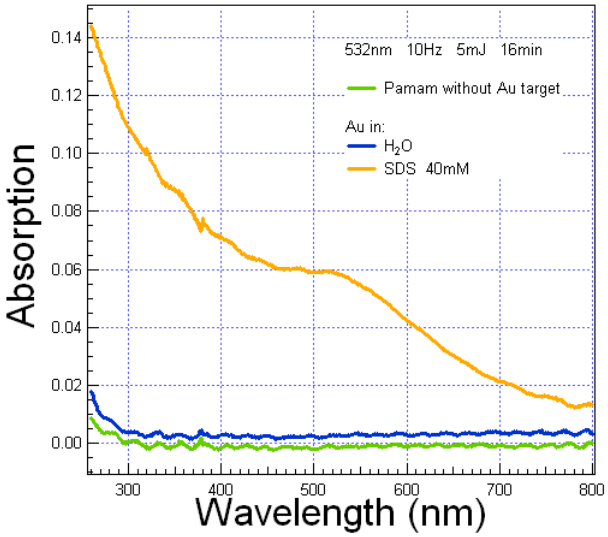

Figure 5.24: The absorption spectra of the solutions prepared by ablation or irradiation at 532nm in different liquids.

Because the 290nm band is present only in the PAMAM G5 colloidal solutions produced by ablation with 532nm, and seeing the three dimensional structure of PAMAM G5 molecule, it was concluded that the band centered at 290nm could originate from a charge transfer (CT)[12] between gold cations trapped inside inner cavities of PAMAM G5 molecules and the ligand. In particular, its spectral position is an indication of the presence of charged gold species in the suspension, the trapping of Au cations leading to the new absorption band centered around 290nm [29].

To confirm this hypothesis for the origin of 290nm band, a chemical reduction experiment [97] was performed[13] (Fig.5.25). To a colloidal solution produced by laser ablation with 5mJ of 532nm a freshly made ice-chilled $NaBH_4$ solution was added. The reduction process took place only after the addition to the suspension of $NiCl_2$ powders that, in $NaBH_4$ solution, is reduced to $Ni(0)$ which acts as a catalyst.

The final result was the disappearance of the UV peak (see the continuous line in Fig.5.25). The need of the $NiCl_2$ catalyst suggests that the positively charged gold clusters created by the 532nm laser light are located inside the dendrimer, for this reason being less reactive than usual to $NaBH_4$. The plasmon band had no significant change because the chemical reduction produced small gold clusters which do not contribute to the plasmon band.

From the results obtained in the previous experiments it follows that the 532nm laser beam produces charged gold clusters. When the process takes place in PAMAM G5 solution, these clusters are trapped and stabilized inside the PAMAM G5 molecules, and the band at 290nm can be considered as a fingerprint of the process.

To investigate the way how charged gold clusters are produced by the 532nm radiation, it was prepared a colloidal solution by ablation at 1064nm 15mJ and then was irradiated with 532nm at 5mJ and 10mJ. The UV-VIS absorption spectra of the three solutions are showed in Fig.5.26 The spectrum of the initial solution (the one produced at 1064nm) exhibited a well resolved plasmon band and no peaks in the UV region. After post irradiation, the plasmon band experienced a considerable reduction, particularly in the case of the sample obtained with the more energetic pulse. The band centered at 290nm is present in the spectra of both post irradiated solutions and its behavior is contrary to that of the plasmon band, being more intense for the sample irradiated with the more energetic pulse.

The mean diameter of the colloidal nanoparticles produced with 1064nm was 4.4nm with a standard deviation of 3.2nm (Fig.5.27.a), and the post irradiated solutions had a mean diameter of: 3nm for 532nm 5mJ, Fig.5.27.b, and 2.7nm for 532nm 10mJ, Fig.5.27.c,

[12] A charge transfer complex (CT complex) is defined as an electron donor electron acceptor complex, characterized by electronic transition(s) to an excited state. In this excited state, there is a partial transfer of electronic charge from the donor to the acceptor [99]. Almost all CT complexes have unique and intense absorption bands in the ultraviolet-visible (UV-VIS) region. Apart from charge transfer interactions between donor and acceptor, electrostatic forces exist as well. Ligand to metal charge transfer (LMCT) complexes experience a partial transfer of electrons from the ligand to the metal. This is common when the metal is at a high oxidation state.

[13] Dr. Anna Giusti, INSTM and Department of Chemistry and Industrial Chemistry DCCI, Genova University, Italy.

with the respective standard deviations of ±1.2nm and ±1.4nm.

In the case of nanosecond laser pulses, the size reduction of the nanoparticles was attributed to a photo thermal process due to direct heating of gold nanoparticles induced by high laser fluence[25]. With picosecond pulses, the photo-fragmentation mechanism is expected to be different. For Ag nanoparticles, Kamat et al.[84] observed that the photo-fragmentation produced by picosecond radiation in resonance with the plasmon band arises from electron ejection due to multiphoton absorption and subsequent charging and disintegration of the particles into smaller size products.

Fig.5.28 illustrates the evolution of absorbance at 514.5nm (A@514.5nm) in function of the number of laser shots during the post irradiation at different 532nm energies of a solution produced with 1064nm. As the 514.5nm is very close to the plasmon resonance of the gold nanoparticles, and due to the low diameter and dispersity of our nanoparticles [96], the A@514.5nm at a time t is approximately proportional to the concentration of the gold nanoparticles, *N(t)*. The variation in the concentration of gold nanoparticles, caused by the photo-fragmentation with 532nm, can be written as:

$$\triangle N(t) = -N(t)\alpha f \triangle t,$$

where: α is the absorption coefficient of the suspension, and f is the laser repetition rate. Then by simple integration, the following formula for the concentration of nanoparticles is obtained:

$$N(t) = N_0 \exp\left[\alpha f T\right],$$

where fT is the total number of laser shots, and the decay rate α provides a measure of the efficiency of the photo-fragmentation process.

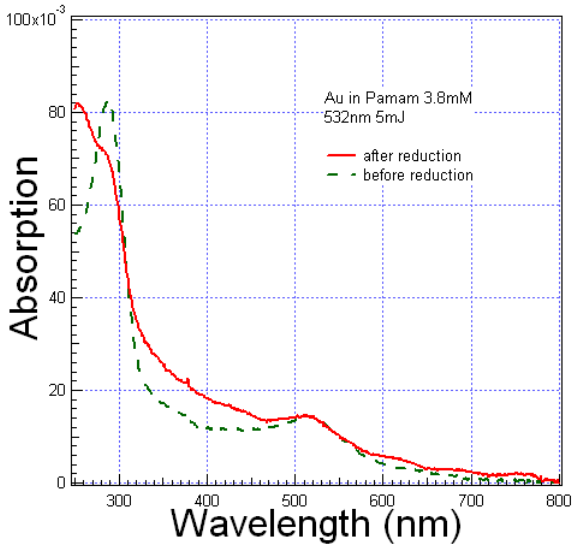

Figure 5.25: Absorption spectra of gold-dendrimer suspensions obtained with 5mJ pulses and 532nm, before (dashed line) and after (continuous line) chemical reduction.

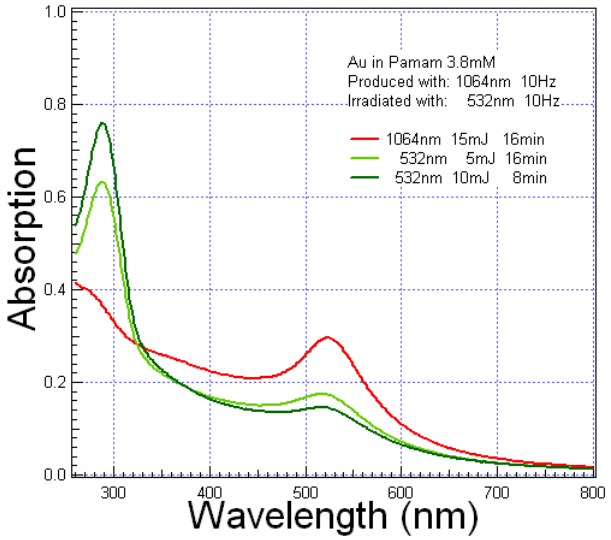

Figure 5.26: Absorption spectra of colloidal gold in PAMAM 3.8mM produced by ablation with 1064nm (red line) and irradiated with 532nm (green lines).

This model neglects the decay of laser intensity across the liquid column and the effects of turbulence and diffusion. It gives useful indication on the order of photo-fragmentation process, even if it does not reproduce exactly the initial part of the absorbance curves and its step-like behaviour present in some cases.

When the decay constants α, obtained from the fitting of the curves in Fig.5.28 with exponential functions, are plotted versus the energy of 532nm laser beam (Fig.5.29), a quadratic dependence is found, indicating that the fragmentation is the result of a two-photon-absorption mechanism [97], leading to the ejection of the conduction electrons. The workfunction of bulk gold is 5.1eV, and it is expected to be much lower in the case of thin films and nanoparticles. Then the two photons at 532nm (2.3eV) could be enough to extract one electron from a gold nanoparticle.

The parabolic fit of the decay constant versus laser pulse energy contains also a linear component [97] of one order of magnitude smaller than the quadratic component at low pulse energy. This component is probably associated with a thermal effect due to the promotion of d-electrons to the conduction band, the laser energy (2.3eV) being strongly resonant with the states corresponding to the L point of the Brillouin zone of gold, for which the distance from Fermi level is of order of 2.4eV[100].

The plasmon band has been fitted with Mie's cross section at the first order to calculate the density of gold nanoparticles. Inserting the TEM data for average radius and standard deviation, a particle density of $4.8 \times 10^{12} Np/cm^3$ was found for the sample of 1064nm, and $4.5 \times 10^{13} Np/cm^3$ for the sample of 532nm, representing an increase by one order of magnitude in the number of particles after post irradiation with 532nm.

The fact that the size reduction of the nanoparticles is accompanied by the build up of the UV band at 290nm (Fig.5.26), leads to the conclusion that this band is connected with the photo-fragmentation of the existing nanoparticles in smaller fragments.

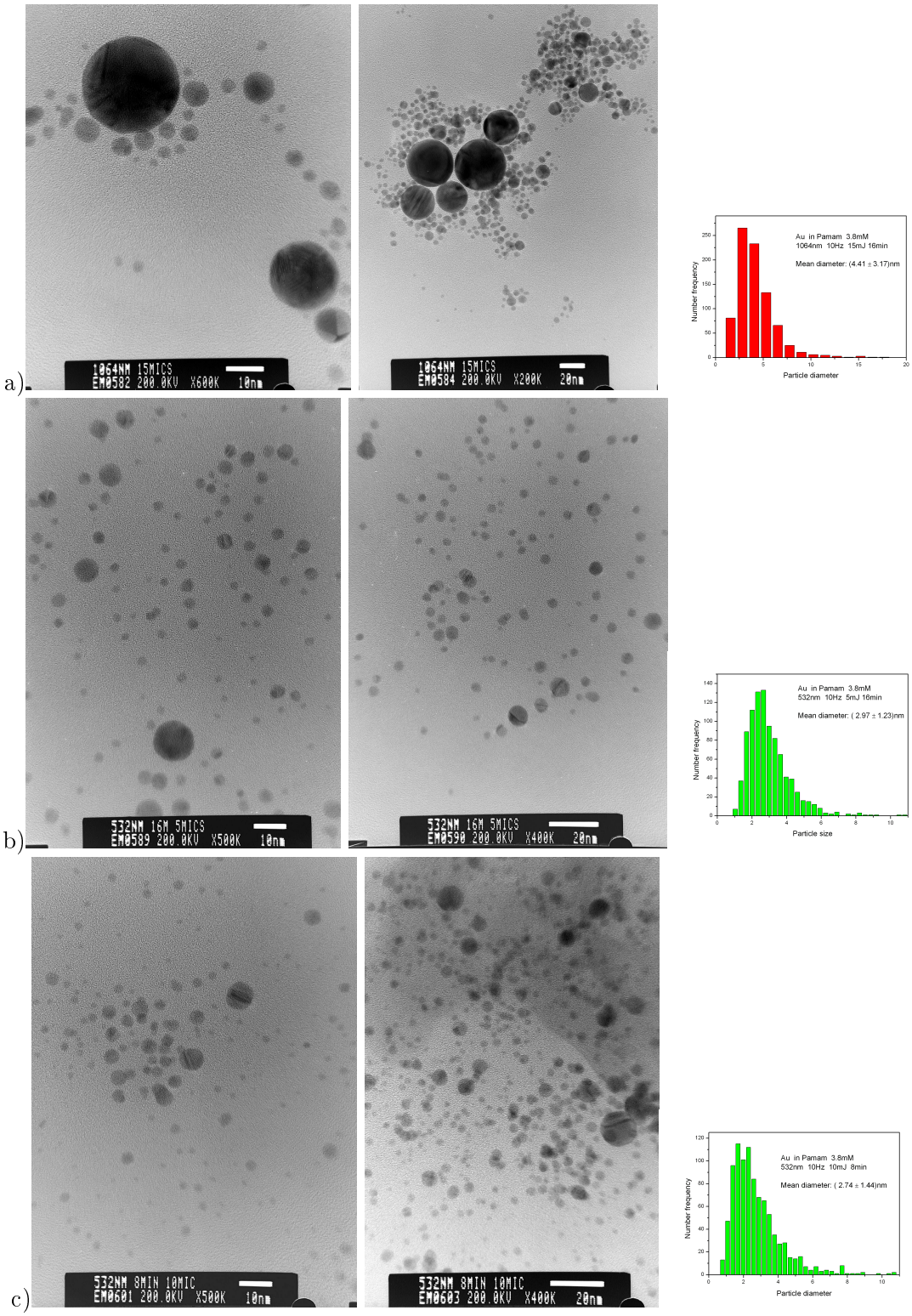

Figure 5.27: Gold nanoparticles in PAMAM 3.8mM: a) produced by ablation with 1064nm 15mJ 16min, and irradiated with 532nm: b)16min at 5mJ, c) 8min at 10mJ.

The formation of the charged gold clusters could be due either to their direct ejection from the target[98], to photo-fragmentation of existing gold nanoparticles, or both.

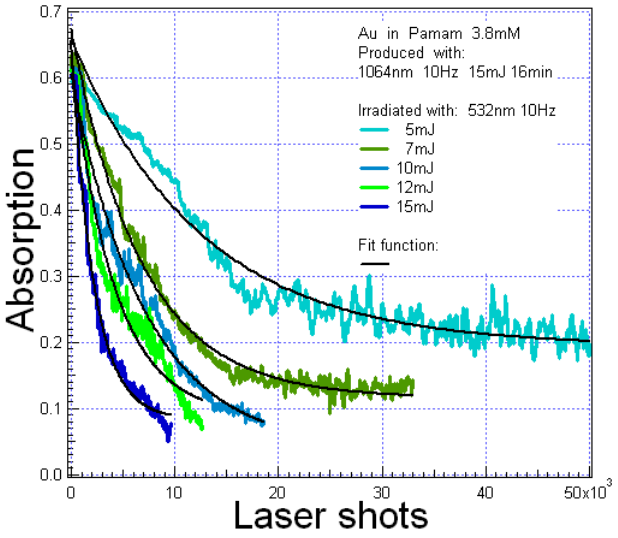

Figure 5.28: Evolution of the A@514.5nm during irradiation with different energies of 532nm of an initial solution produced at 1064nm.

The on-line monitoring of T@514.5nm (Fig.5.30. a and b) presents the same different ablation mechanism [95] in the case of 532nm and 1064nm, as observed before for the ablation in SDS solution (Fig.5.16). In the case of ablation with 1064nm (Fig.5.30.a), there is a continuous exponential decay, which for sufficiently long exposure and sufficiently high energy per pulse, reduces to 0, while at 532nm, (Fig.5.30.b), it produces an initial minimum value of T@514.5nm, followed by an oscillatory behaviour and the instauration of a final constant value dependent on the energy of the ablation beam.

Comparing the transmission measurements for the ablation with 1064nm and 532nm (Fig..5.30.a and b) it can be seen that for ablation at 532nm the decrease of T@514.5nm, associated with the build up of the plasmon band, starts around 0.5mJ, corresponding to a fluence of 0.03 J/cm^2, and at 1064nm the threshold energy and fluence are higher by a factor of 10, that is 5mJ and 0.3 J/cm^2, respectively. These values represent the ablation threshold energies for the two laser wavelengths, at the given experimental conditions.

The abundance of ablated gold as a function of laser shots[19] (Fig.5.30.c and d) confirms the two different ablation mechanisms for 1064nm and 532nm. The spectra used to infer the data reported in Fig.5.30.c and d were recorded one day after the preparation of the solutions and, consequently, are not affected by diffusive mechanisms or instabilities that can have some influence on the on-line transmission curves.

For the ablation at 1064nm the quantity of ablated gold in solution grows linearly with the time of ablation. The slope changes can be attributed to attenuation of the laser beam with increasing of the colloid concentration. In contrast, at 532nm, the abundance of ablated gold grows very rapidly up to 600 laser shots, and then tends to saturation with an oscillatory behaviour.

The origin of saturation for 532nm is due to the following reasons: i) as long as the ablation process produces gold nanoparticles, the green light is progressively attenuated by

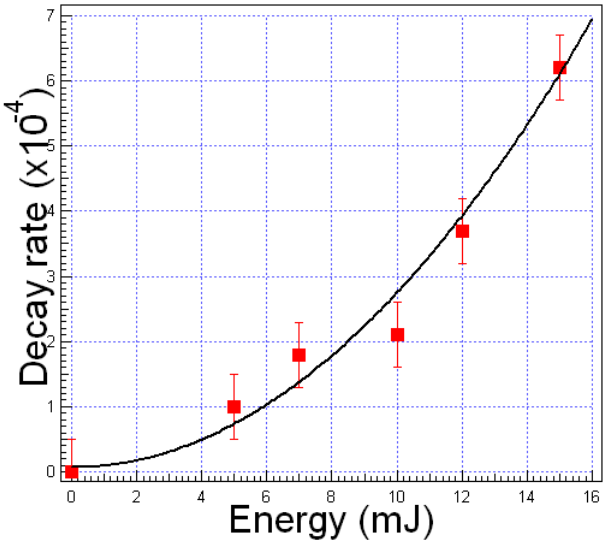

Figure 5.29: Decay constant α, plotted versus laser energy.

the solution (due to the plasmon band absorption at 520nm) and the laser fluence reaching the target decreases; ii) at the same time, according to [84], the absorbed 532 nm radiation can induce multiphoton absorption and subsequent photo-fragmentation [96] of the gold nanoparticles. This process progressively reduces the concentration of gold nanoparticles and eventually recovers the fluence reaching the target.

The final constant value of T@514.5nm reflects the equilibrium reached between the rate of fragmentation and that of the nanoparticles formation (see Section 4.2). Moreover, for ablation at 532nm, when the abundance of ablated gold arrives to the saturation, the averaged diameter of the nanoparticles should have reached its minimum value.

The spectra of a number of colloidal solutions produced by ablation with 532nm at various laser energies are presented in Fig.5.31. The 290nm band and the gold plasmon band are present in all spectra (in the sample produced at 0.5mJ the plasmon band is very small). By increasing the ablation energy, the plasmon band increases with an oscillatory behaviour. The band at 290nm has an analogue evolution with increasing the laser energy, but it increases faster and its oscillatory behaviour is more evident.

Fig.5.32 reports the evolution of the absorption spectra with increasing number of the laser shots (which is the increase of the ablation time) at the same laser energy of 532nm. The plasmon band centered at 520nm appears in the spectrum after 150 laser shots and rapidly saturates with an oscillatory behaviour (Fig.5.33.a), while the 290nm band starts to be visible only around 1000 laser shots, grows with increasing the number of laser shots and after 7000 laser shots have an oscillatory behaviour (Fig.5.33.b).

When the results of the evolution of absorption at 520nm, presented in Fig.5.33.a, are confronted with the results of absorption at 400nm, presented in Fig.5.30.d, it can be seen they have a similar evolution with increasing the number of laser shots at 532nm: they have an initial rapid increase and then saturates.

It follows that by ablation with 532nm, first are produced gold nanoparticles which

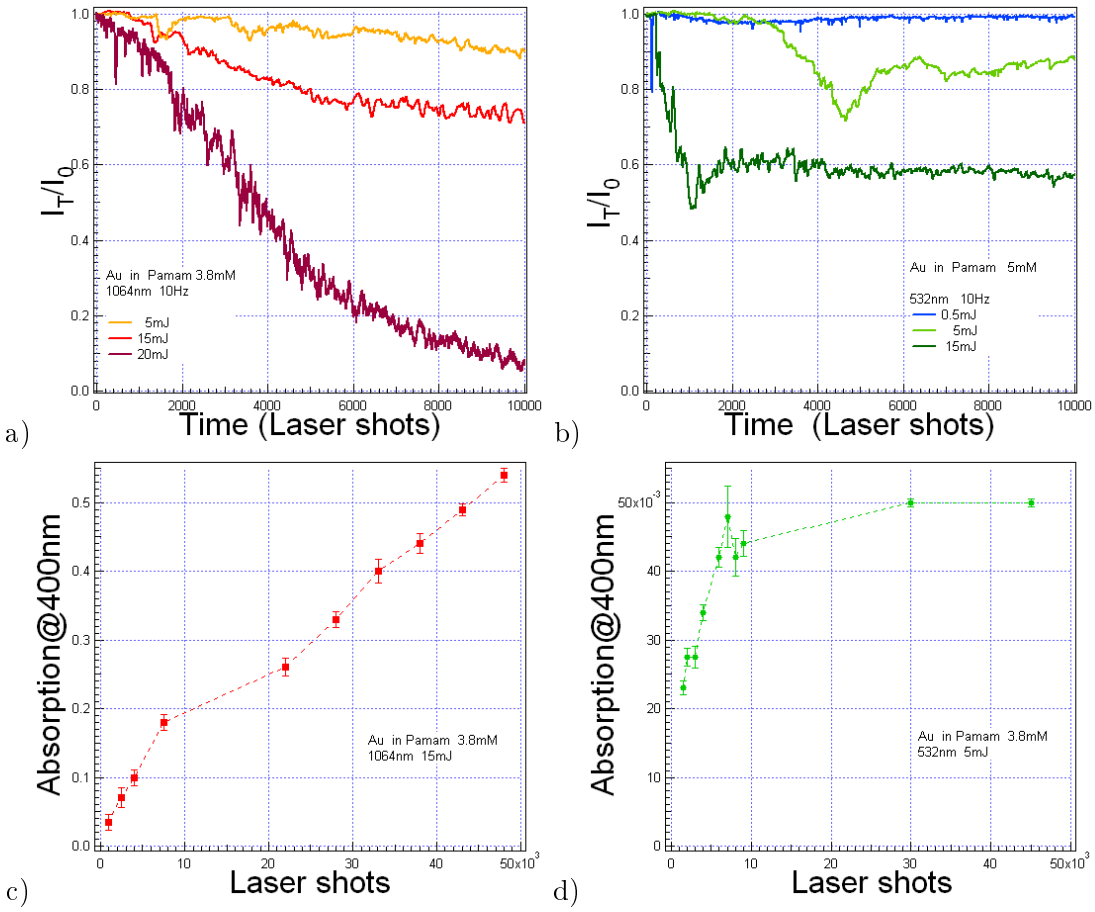

Figure 5.30: Suspensions of gold nanoparticles in 3.8 mM PAMAM G5: ablation threshold for a) 1064nm, b) 532nm, evidenced by the on-line monitoring of T@514.5nm. Absorbance at 400 nm versus number of laser shots at: c) 1064 nm, 15 mJ per pulse, d) 532 nm, 5 mJ per pulse.

exhibit the plasmon band. After their number and diameter are high enough so that they have an efficient absorption of the laser energy, the green light is progressively attenuated by the solution and the laser fluence reaching the target decreases. Due to the absorption of 532nm, the photo-fragmentation of these nanoparticles takes place accompanied by the formation of the charged gold clusters which give birth to the 290nm absorption band (Fig.5.33.b).

The evolution of the absorption spectra with increasing number of the laser shots at the same laser energy of 1064nm is shown in the Fig.5.34. The plasmon band has a first rapid linearly increase in the first 10000 laser shots, followed by a net change between 10000 shots and 20000 shots, and a further linearly increase after 20000 shots. The absorbance at 520nm (Fig.5.35) (the plasmon band evolution) for these solutions is identical with that for the absorption at 400nm (Fig.5.30.c), which reflects the quantity of ablated gold present in solution. It follows that the use of the 1064nm results in continuous ablation of the gold target and subsequent nucleation and growth of the gold nanoparticles.

The net change of the absorbance between 10000 shots and 20000 shots is present

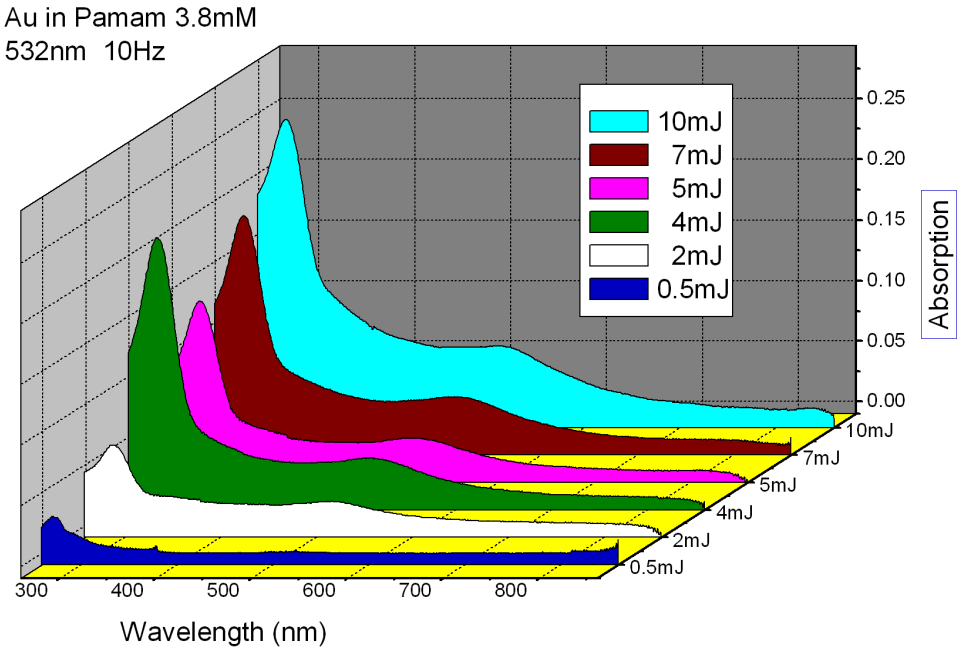

Figure 5.31: The evolution of the 290nm band and of the plasmon band when the ablation is made at different energy of the 532nm laser beam.

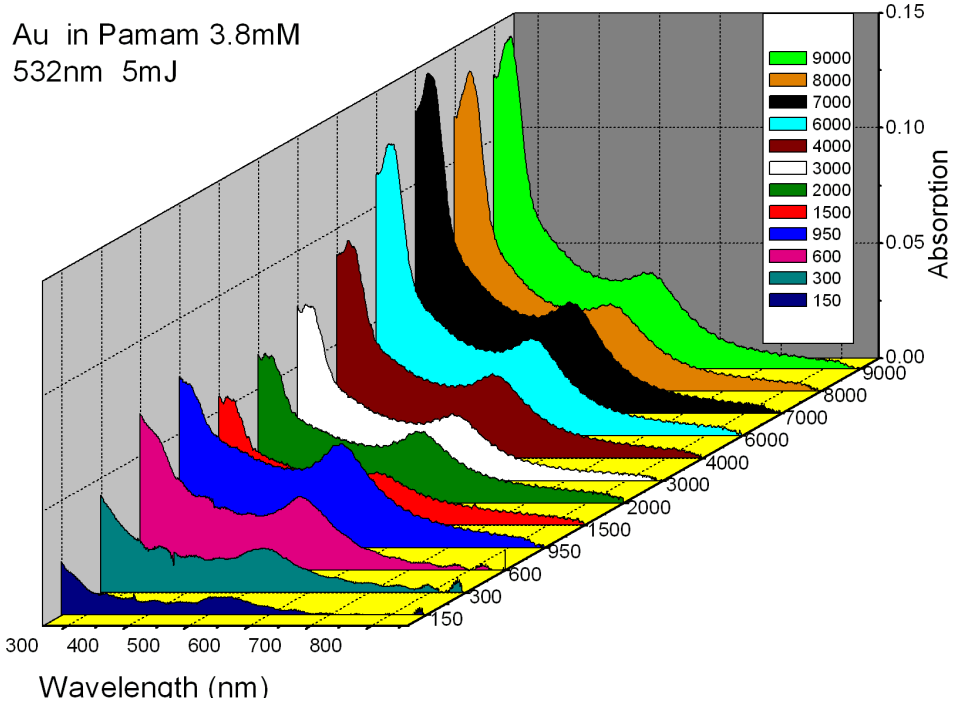

Figure 5.32: The behaviour of the 290nm band and of the plasmon band as a function of the number of laser shots at 532nm.

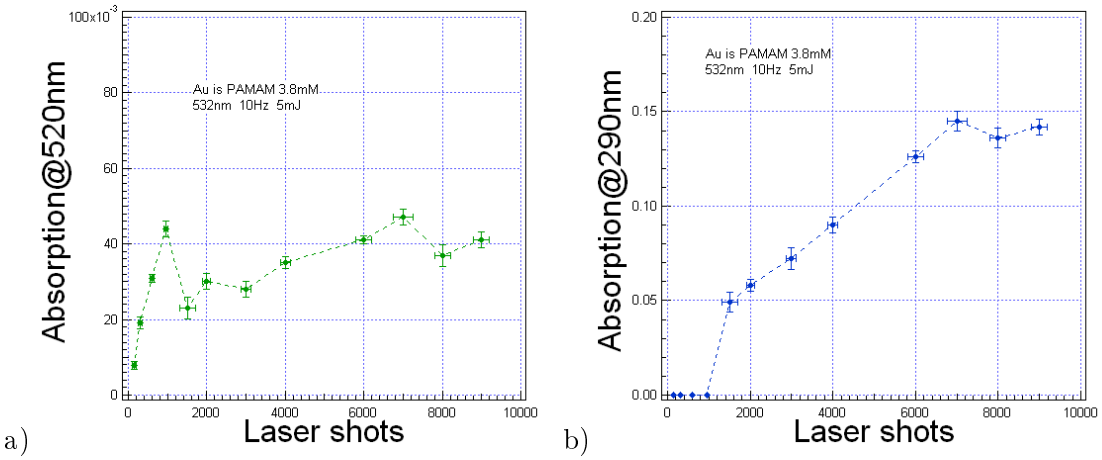

Figure 5.33: The behaviour of the absorbance at 520nm a) and at 290nm band b) as a function of the number of laser shots at 532nm.

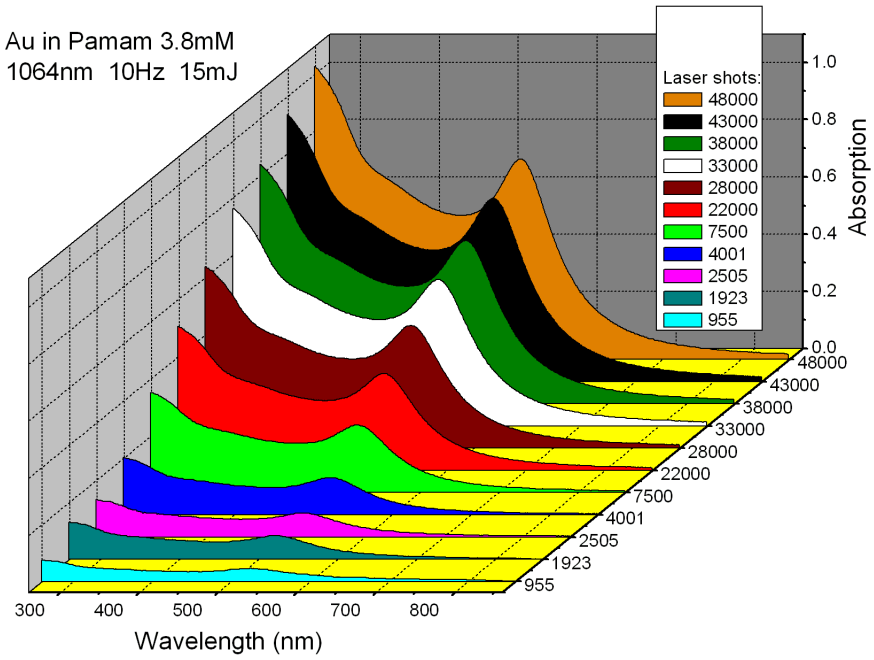

Figure 5.34: The absorption spectra as a function of the number of laser shots at 1064nm.

in both figures (Fig.5.30.c and Fig.5.35). It is not clear yet what cause this change in the absorbance at 400nm and 520nm (further investigations are on the way and will be presented elsewhere). A possible hypothesis is that it could be due to an attenuation of the 1064nm laser beam with increasing concentration of the nanoparticles in solution. This would lead to a decrease in the energy of the laser beam reaching the target, and then to a reduction of the quantity of ablated gold, followed by a subsequent reduction of the rate of formation of nanoparticles exhibiting the plasmon band.

A degradation mechanism of the nanoparticles [97], similar to that of the 532nm, is observed by exposing PAMAM G5 stabilized suspensions of gold nanoparticles in water for 20minutes to the low power UV radiation of a mercury lamp emitting at 254nm with

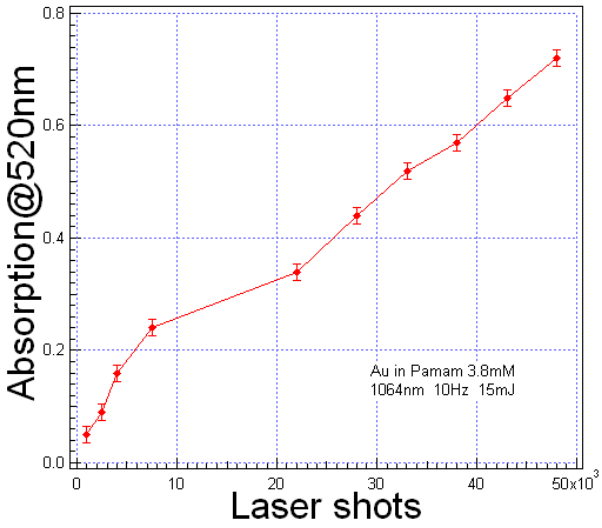

Figure 5.35: Absorbance at 520nm as a function of the number of laser shots for 1064nm.

a fluence of $160\mu W/cm^2$ (Fig.5.36). The UV post-irradiation was performed by using 1-mm-thick quartz cuvettes completely filled with PAMAM G5-stabilized suspensions of gold nanoparticles, meanwhile at 532nm the laser post-irradiation of the suspensions was performed in the same conditions adopted for their preparation.

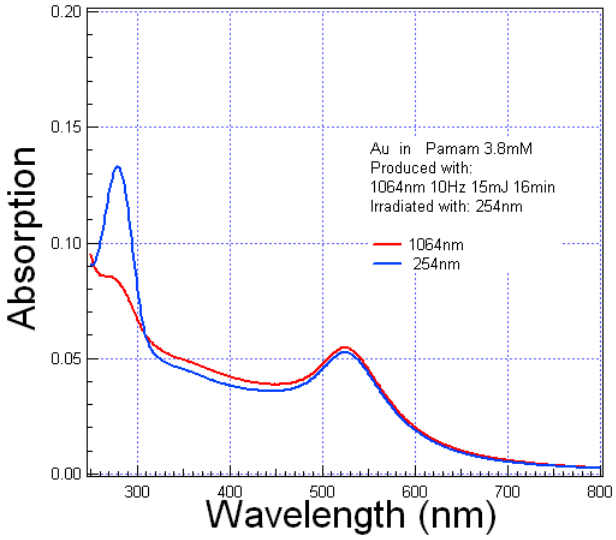

Figure 5.36: Absorption spectra of a colloidal gold solution produced by ablation with 1064nm in PAMAM 3.8mM and post-irradiated for 20minutes with a mercury lamp emitting at 254nm with a fluence of $160\mu W/cm^2$.

The absorption spectrum of the UV irradiated solution, is almost identical with the spectra of the initial solution in the vicinity of the plasmon resonance (Fig.5.36), which confirms that UV-induced size reduction is negligible and that UV irradiation does not substantially influence the density of nanoparticle. In analogy with what was observed in the case of 532nm irradiation, the growth of the intense peak at 290nm in the absorption

spectra of the UV irradiated solution indicates that there is an extraction of conduction electrons from the gold nanoparticles and consequent production of gold cations or metal clusters trapped by PAMAM G5.

For the 254nm radiation, the photon energy is 4.9eV, and it results that one photon is sufficient to obtain the electron ejection in a single-photon process.

The value of the mean diameter of gold nanoparticles produced by ablation with 1064nm and post-irradiated with the UV lamp (Fig.5.37) is 4.75nm. It follows that the size of the nanoparticles is not reduced by the radiation with 254nm. By fitting the absorption spectrum with Mie's cross section, a density of $3.5 \times 10^{12} N/cm^3$ was found, which is of the same order of magnitude as for the non irradiated samples. This confirms that the irradiation with 254nm lamp lead to the production of gold cations without having a size reduction effect on the gold nanoparticles.

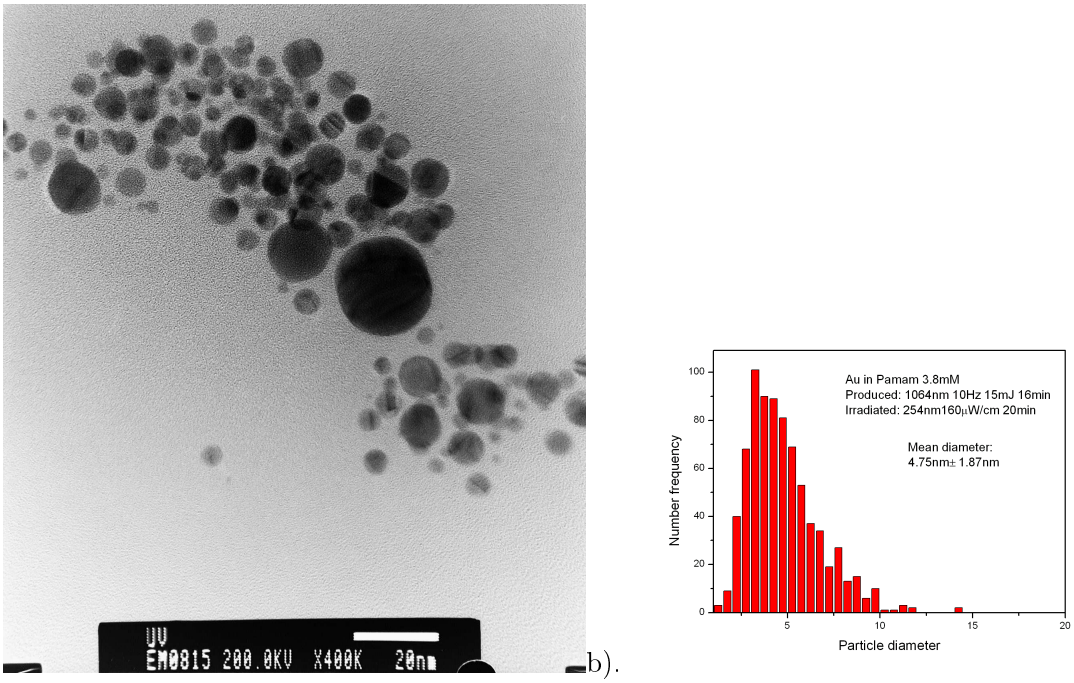

a). b).

Figure 5.37: TEM photo, a)., and size distribution , b)., of gold nanoparticles produced with 1064nm and post-irradiated for 20minutes with a mercury lamp emitting at 254nm with a fluence of $160 \mu W/cm^2$.

5.4.2 Discussion

The results of the experiments performed in aqueous solution of PAMAM G5 for the production of colloidal gold nanoparticles lead to the following conclusions:

- for the production of gold nanoparticles by laser ablation at 1064nm an almost linear growth of gold nanoparticles concentration versus the amount of ablated material per shot is found;

- there are evidences which allow to conclude that the ablation process with 532nm is the result of a three competing processes:

    1. ablation of the target followed by nucleation of the ablated species and growth of the nanoparticles;
    2. linear absorption of the laser beam by the existing gold nanoparticles and subsequent reduction of the energy reaching the target, which causes a decrease of the ablation rate and subsequent saturation of the plasmon band;
    3. absorption of the laser beam by the existing gold nanoparticles leading to electron ejection from nanoparticles, formation of gold cations, and fragmentation of the nanoparticles [97];

- the photo-degradation mechanism is attributed to photoejection of electrons from gold nanoparticles and subsequent instability produced by an excess of positive charges [29, 84];

- the known size-reduction effect of the 532nm for gold nanoparticles has been demonstrated to be a two-photon process when picosecond laser pulses are used;

- the appearance of the 290nm band originates from a charge transfer (CT) between gold cations trapped inside inner cavities of PAMAM G5 molecules and the ligand, the origine of Au cations induced by the 532nm radiation being attributed to electron ejection subsequent disintegration of existing gold;

- the workfunction of PAMAM G5-capped-gold nanoparticles in water is lower than the value of 5.1eV attributed to bulk gold, and it was possible to locate it below 4.6eV [97];

- exposure of the suspensions to the mercury lamp at 254nm permitted to observe single-photon degradation, but was not enough for a size-reduction effect of the gold nanoparticles.

5.5 Work in progress

Until now the synthesis of gold nanoparticles by laser ablation was investigated mainly in liquids like water [88, 85, 60], aqueous solution of SDS [18] and cyclodextrines[86], a number of aliphatic alcohols and alkanes [104], and toluene[101] , and the previous experiments used nanosecond and femtosecond laser pulses.

In the following the first results, obtained during this thesis work, for the synthesis of gold nanoparticles by picosecond laser ablation in toluene, chloroform and diethyl ether are presented. In all the experiments, the gold solid target (Goodfellow) was placed on the bottom of a 1cm x 1cm cuvette containing 2mL of liquid. The liquid column above the target was 2cm.

5.5.1 Core-shell gold nanoparticles in toluene

Toluene, also known as methylbenzene or phenylmethane, has the formula C_7H_8 (Fig.5.38) and is a water-insoluble liquid widely used as an industrial feed stock and as a solvent. It is used to open red blood cells in biochemistry experiments and as a carbon source for making Multi-Wall Carbon Nanotubes.

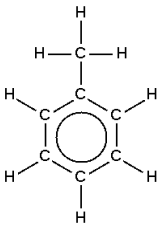

Figure 5.38: Structure of toluene molecule.

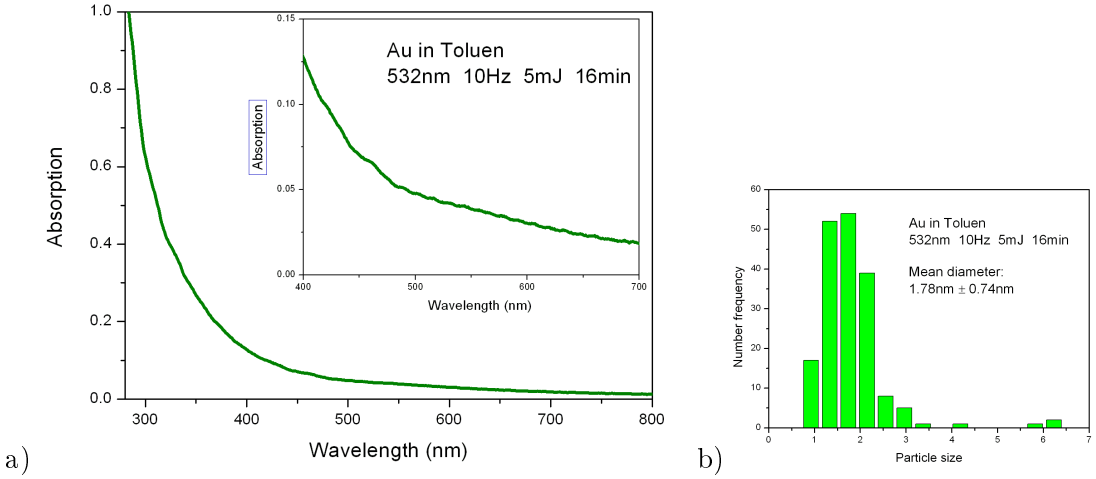

Figure 5.39: Gold nanoparticles produced by 16 min laser ablation in diethyl ether with 532nm at 10Hz 5mJ: a) the absorption spectra, and b) the size distribution.

We produced gold nanoparticles in toluene by 16min ablation with 532nm at 10Hz and

5mJ. The absorption spectra of the resulting solution did not present the characteristic plasmon band of the colloidal gold (see Fig.5.39.a) and this lead to the initial erroneous conclusion that no gold nanoparticles are produced. But TEM investigations (Fig.5.40) show the presence of the gold nanoparticles with mean diameter of 1.8nm and a standard deviation of $\pm$0.7nm (Fig.5.39.b).

Our first results are in accordance with those of Meneghetti group [101] which produced gold nanoparticles by nanosecond laser ablation at 1064nm in toluene. The gold nanoparticles synthesized by laser ablation in toluene result to be core-shell nanoparticles, the gold core being surrounded by a carbon shell[101]. The absence of the plasmon band is attributed to both: the small size of the nanoparticles (<2nm) and to the carbon matrix which, as follows from the Mie's theory for core-shell nanoparticles, suppresses the surface plasmon resonance[102].

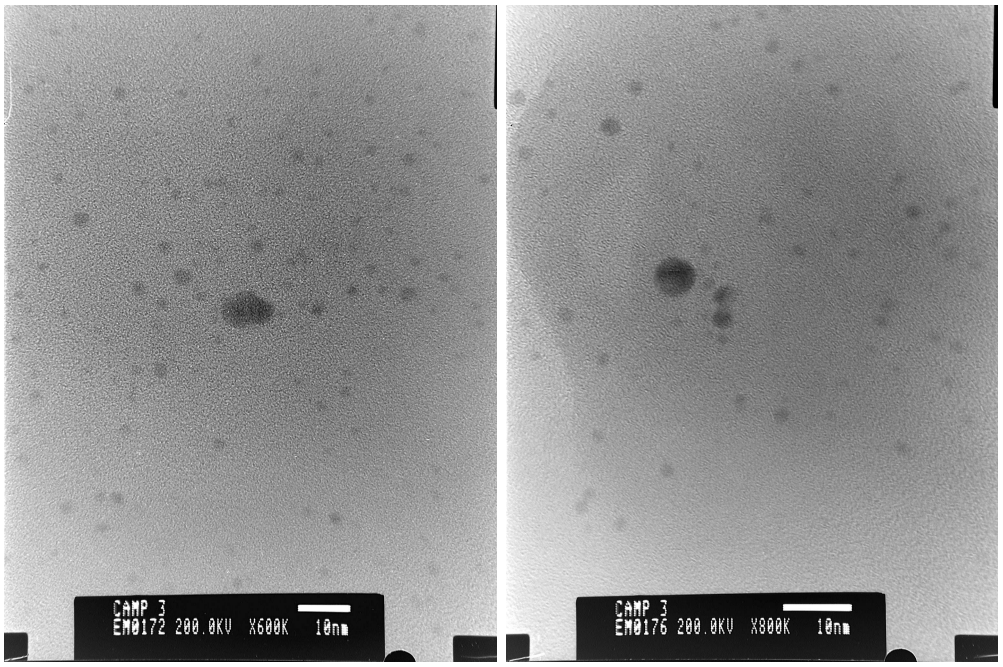

Figure 5.40: TEM images of gold nanoparticles in toluene.

5.5.2 Gold nanoparticles in chloroform ?

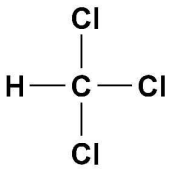

Figure 5.41: Structure of chloroform.

Chloroform, also known as trichloromethane and methyl trichloride, is a chemical compound with formula $CHCl_3$, as shown in Fig.5.41. It has a myriad of uses as a reagent,

and it is a common solvent because it is relatively unreactive, miscible with most organic liquids, and conveniently volatile. Small amounts of chloroform are used as a solvent in the pharmaceutical industry and for producing dyes and pesticides. Chloroform is an effective solvent for alkaloids[14] in their base form.

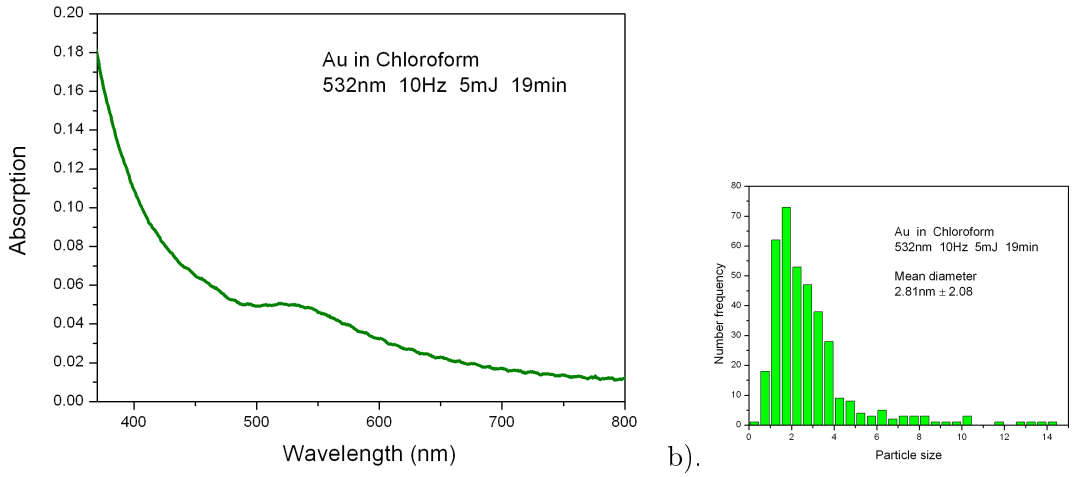

a). b).

Figure 5.42: Gold nanoparticles in chloroform, produced by laser ablation with 532nm at 10Hz 5mJ 19min: a) absorption spectrum, and b) size distribution.

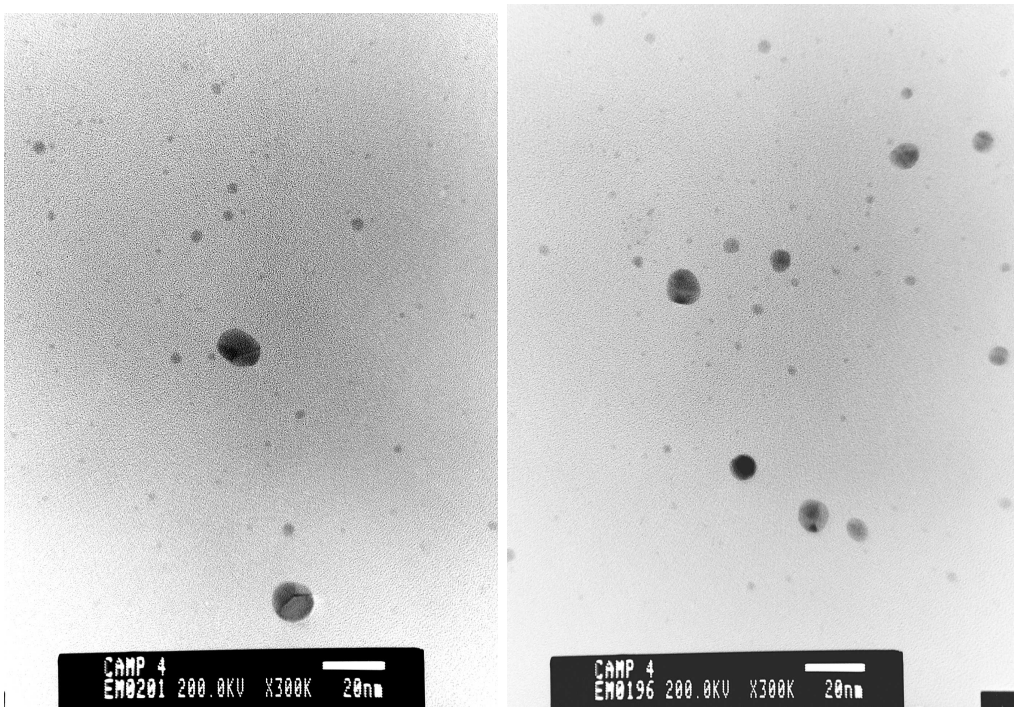

Figure 5.43: TEM photos of gold nanoparticles in chloroform, produced by laser ablation with 532nm at 10Hz 5mJ 19min.

[14] An alkaloid is, strictly speaking, a naturally occurring amine produced by a plant, but amines produced by animals and fungi are also called alkaloids. Many alkaloids have pharmacological effects on humans and other animals. Some alkaloids are used medicinally as analgesics (pain relievers) or anaesthetics, particularly morphine and codeine, and for other uses.

In chemistry, gold nanoparticles in chloroform were obtained only by phase transfer of capped gold nanoparticles[103], their production directly in chloroform being unattainable because of the chlorides formation.

Laser ablation of gold in chloroform[104] and in chloroform solutions of cetyltrimethylammoniumbromide (CTAB)[15] [105] was studied using nanosecond laser pulses. In the previous experiments, the formation of gold colloids was not observed, the plasmon band was missing from the extinction spectrum of the resulting solution, and only a gold-chlorine compound was obtained.

We performed 19min ablation of the gold target in 2ml of chloroform with 532nm at 10Hz and 5mJ. Fig.5.42.a shows the absorption spectra of the resulting solution and a maximum of absorbance can be seen in correspondence to the characteristic plasmon band of the gold nanoparticles. The absorption spectra was take several days after the production of the solution. The TEM images of this sample are presented in Fig.5.43, and from their analysis followed that the gold nanoparticles in chloroform have mean diameter of 2.8nm with a standard deviation of 2.1nm, as shown in Fig.5.42.b, and 9% of the nanoparticle have been found to have a diameter bigger than 5nm.

Energy Dispersive X-ray Spectroscopy (EDS or EDX) analysis (Fig.5.44), was performed for the TEM samples prepared on cooper grids, and resulted that gold and cooper were the only elements in the sample. From the results of TEM and EDX analysis and from those of absorption spectroscopy it seams that we obtained gold nanoparticles in chloroform, but more investigations need to be done on this.

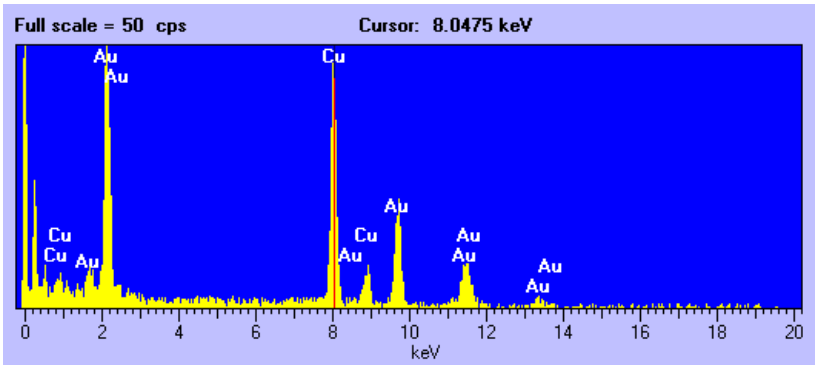

Figure 5.44: EDX analysis for TEM samples.

5.5.3 Production of gold nanoparticles in diethyl ether

Diethyl ether, also known as ether and ethoxyethane, has the formula $CH_3 - CH_2 - O - CH_2 - CH_3$, as shown in Fig.5.45. It is used as a common solvent, non-polar organic compounds being highly soluble in it, and it is sparingly soluble in water (6.9 g/100 ml).

The gold nanoparticles were produced by 16 min laser ablation in diethyl ether with 1064nm at 10Hz and 5mJ. The absorption spectra of the colloidal solutions produced

[15]CTAB is suitable for use in molecular biology applications for genomic DNA purification and it is intended for research use only, not for use in human, therapeutic or diagnostic applications.

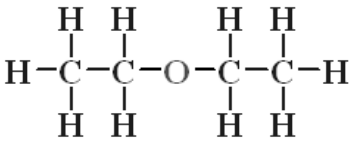

Figure 5.45: Structure of diethyl ether molecule.

in diethyl ether (Fig.5.46.a), do not present the characteristic plasmon band. The TEM images (Fig.5.47), revealed big nanoparticles with mean diameter of 16.82nm and standard deviation of 12.3nm (Fig.5.46.b). Moreover, 23% of the nanoparticles have diameters over 20nm and 4% of them have diameters greater than 50nm.

The reason of the plasmon band absence from the absorption spectra is unknown and we do not have yet a plausible hypothesis for this.

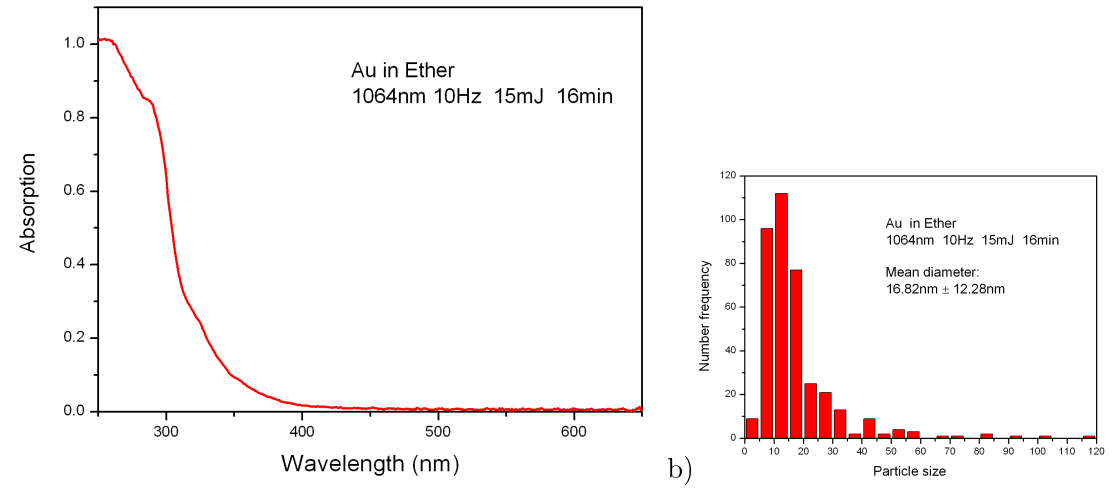

a) b)

Figure 5.46: Gold nanoparticles produced by 16 min laser ablation in diethyl ether with 1064nm at 10Hz and 5mJ: a) the absorption spectra, b) the size distribution.

5.5.4 Preliminary results

From the preliminary experiments of production of colloidal gold nanoparticles by picosecond laser ablation in toluene, chloroform and diethyl ether it follows that:

- spherical shape nanoparticles are produced in all three liquids;
- the nanoparticles produced in toluene and in diethyl ether do not exhibit in their absorption spectra the characteristic plasmon band of the gold nanoparticles, they could by core-shell nanoparticles (gold-carbon) but further investigations have to be done to confirm this hypothesis;
- in toluene and chloroform we obtained very fine nanoparticles, while in diethyl ether the nanoparticles diameter is one order of magnitude greater ($\simeq$17nm);

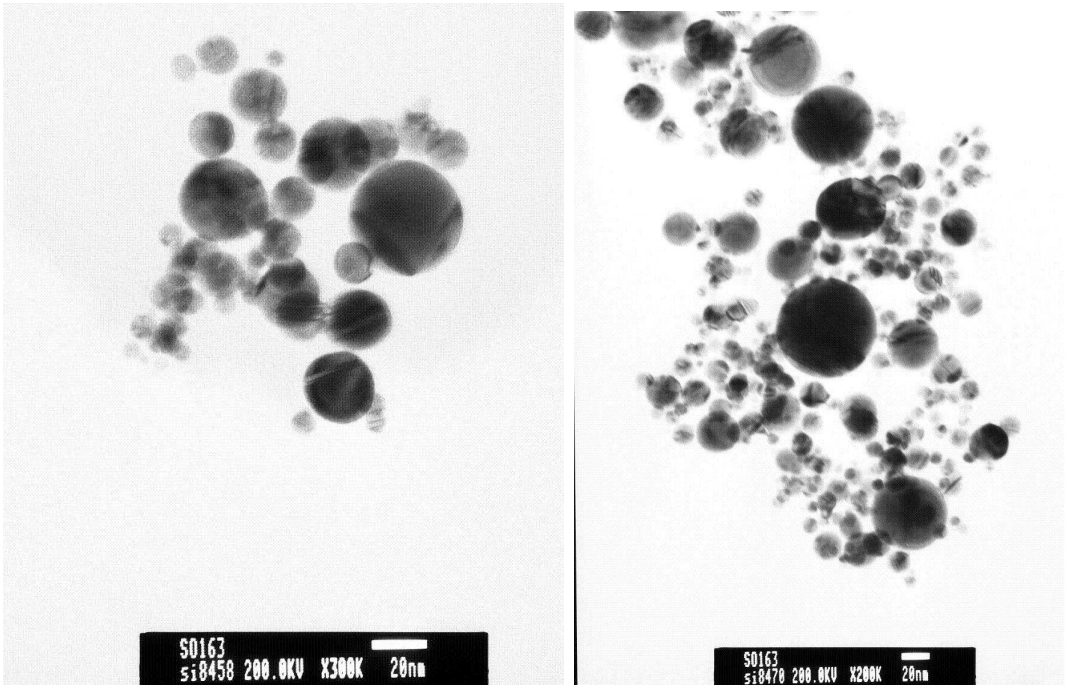

Figure 5.47: TEM photos of gold nanoparticles produced by 16 min laser ablation in diethyl ether with 1064nm at 10Hz 5mJ.

- the spectroscopic and EDX analysis confirm that the nanoparticles produced in chloroform are gold nanoparticles.

Chapter 6

Conclusions and further developments

In this thesis we have reported an experimental study of the synthesis of colloidal gold nanoparticles by picosecond laser ablation of a solid target in various liquid environments. The experimental work was focused mainly on the study of colloidal gold nanoparticles production in water with PAMAM G5 as stabilizing agent in a concentration of 3.8mM. For the target ablation were used the fundamental (1064nm) and the second harmonic (532nm) of a modelocked Nd:YAG laser. Our investigation was based on the combined use of different experimental techniques, i.e. on-line monitor of the optical transmission of a low power beam at 514.5nm from an Ar laser, UV-VIS spectroscopy and electron microscopy (TEM).

The results show that by picosecond laser ablation spherical shape gold nanoparticles were produced in all experimented liquids. The mean diameter of the resulting nanoparticles turned out to be dependent on the laser wavelength employed for the target ablation, on the nature of the liquid environment, and on the stabilizing agent. Its value was rather small: between 1.7nm in toluene and 4.5nm in aqueous solution of PAMAM G5, with the exception of diethyl ether in which the mean diameter of the nanoparticles is increased to 16.8nm.

When the liquid environment is the doubly deionized water, the produced nanoparticles coalesce into greater size nanoparticles, form aggregates with dendritic shapes and precipitate fast unless a stabilizing agent, (SDS or PAMAM G5) is introduced in the solution. The aggregation of unprotected nanoparticles in water is enhanced in the samples produced by ablation with 532nm laser wavelength due to the excitation of the plasmons resonances of the nanoparticles by the absorbed light resulting in additional attractive forces among nanoparticles via induced electromagnetic multipolar interactions.

The preliminary results for the production of gold nanoparticles in organic solvents are very promising although that needs a further investigation. In the case of chloroform, our result is remarkably different from what is known for the literature and give us reasons to think it could be possible to produce uncapped gold nanoparticles or core-shell

nanoparticles in chloroform by picosecond laser ablation.

The combined use of the on-line monitoring of the optical transmission at 514.5nm and of the UV-VIS spectroscopy allowed us to conclude that there are two different action mechanisms for the two laser wavelengths. At 1064nm each laser shot fully interacts with the target, while at 532nm a screening occurs due two the onset of gold nanoparticles concentration, whose plasmon resonance frequency almost matches the laser wavelength. The visible wavelength exhibited a lower ablation threshold than the infrared one, and reached early saturation, the number of laser shots necessary to reach the saturation being greatly sensitive to ablating wavelength and energy.

At 1064 nm we can infer an almost linear growth of gold nanoparticles concentration versus the amount of ablated material per shot, explained by analogy with the formation of a precipitate in supersaturated solution. For 532nm, it has been demonstrated that the ablation process is the result of three competing processes:

1. ablation of the target followed by nucleation of the ablated species and growth of the nanoparticles,

2. linear absorption of the laser beam by the existing gold nanoparticles and subsequent reduction of the energy reaching the target, which causes a decrease of the ablation rate and subsequent saturation of the plasmon band,

3. absorption of the laser beam by the existing gold nanoparticles leading to electron ejection from nanoparticles, formation of gold cations and fragmentation of the nanoparticles.

Also the post-irradiation of the colloidal gold nanoparticles with the 532nm wavelength of intense laser beam has been shown to induce multiphoton absorption and subsequent photo-fragmentation of gold nanoparticles, providing a possibility for further control of nanoparticle shape and size. Moreover, it was found an increase by one order of magnitude of the number density of gold nanoparticles in solution after post-irradiation at 532nm.

The size-reduction effect of the 532nm wavelength has been demonstrated to be a two-photon process when picosecond laser pulses are used. It was also shown that by irradiation of the gold nanoparticles with 532nm beam, charged gold clusters are produced, and the origin of resulting gold cations has been attributed to electron ejection due to multiphoton absorption and subsequent charging and disintegration of the nanoparticles.

The photo-fragmentation of PAMAM G5-capped gold nanoparticles was observed either under irradiation with picoseconds pulses at 532nm or with a low power lamp emitting at 254nm. The simultaneous check of absorption and TEM data permitted to distinguish the effects of the different light sources used for photo degradation. The intense laser light at 532nm produces mainly fragmentation with a significant reduction of plasmon absorption, while the UV lamp emitting at 254nm induces a gentle peeling of the nanoparticles by extracting ions from the outer shell and leaves the plasmon band substantially unchanged.

The photo fragmentation effect is accompanied by the growth of an absorption band around 290nm in the electronic spectra of the suspensions. The band at 290nm originates from a ligand to metal charge transfer (LMCT) between gold cations trapped inside inner cavities of PAMAM G5 molecules and the ligand. This band constitutes a reliable tag to carry out new insights about the mechanism of photon induced fragmentation.

The spectroscopic monitoring of charged metal clusters is, in general, very difficult and affected by a large incertitude due to their weak contribution to the absorption spectra [84].We have demonstrated that the use of PAMAM G5 as stabilizing agent of laser produced gold nanoparticles permits easy detection and monitoring of the concentration of charged metal clusters thanks to its ability to enclose the clusters within its inner cavities which leads to the charge transfer band at 290nm.

By using 290nm band as a tag of cation concentration, it has been worked out that the workfunction of PAMAM G5-capped-gold nanoparticles in water is lower than the value of 5.1eV attributed to bulk gold, and it was possible to locate it below 4.6eV. The use of a continuously tunable UV source could permit to measure the workfunction of gold nanoparticles by a simple monitoring of the onset of the absorption band at 290nm.

The absence of the charge transfer band at 290nm for the samples produced by laser ablation with 1064nm suggests that the charged fragments extracted from the target during the ablation coalesce into neutral nanoparticles on a time scale that is fast with respect to the laser repetition rate.

Several interesting questions remain open and could be investigated by further experiments. To mention some, more details on the material ablation and propagation in liquids environment on a time scale closer to the laser pulse duration could give significant information about the picosecond laser ablation mechanism and nanoparticles formation. pH influence on the nanoparticles production and aggregation could be of interest for the biomedical applications of the PAMAM G5-capped nanoparticles.

Moreover, the use of a two wave mixing beam (1064nm and 532nm) for production of colloidal gold nanoparticles in liquids could lead to the one-step preparation of small size colloidal gold nanoparticles with desired nanoparticles concentration and narrow size distribution, as it would combine the effects of the two laser wavelengths (the continuous ablation of the 1064nm and the size-reduction effect of the 532nm).

Great interest is manifested for the nanoparticles functionalized with polymers and their one-step functionalization. For this reason, a future direction in our research is the production and functionalization of gold nanoparticles with polymer molecules in a one-step process.

Acknowledgments

I am deeply grateful to Prof. Francesco Giammanco for his valuable scientific advises and ideas that made this thesis possible.

Many thanks to all the members of the *Intense laser fields and collective effects in plasmas* group, in which I was working in the last four years, a special thanks to Paolo Marsili, for his technical help in laboratory.

I would like to thank also Dr. Emilia Giorgetti from Istituto dei Sistemi Complessi and INSTM, Consiglio Nazionale delle Ricerche Firenze, Dr. Anna Giusti from INSTM and Department of Chemistry and Industrial Chemistry DCCI of Genova University, with whom I had the opportunity to work with, and Dr. Giovanna Giorgetti from Department of Earth Science at the University of Siena for her precious support in TEM analysis.

Finally, I would like to thank all my friends for their support and understanding, specially in the period of writing this thesis.

List of related papers

- *Production of colloidal gold nanoparticles by picosecond laser ablation in liquid*, E. Giorgetti, A. Giusti, **S.C. Laza**, P. Marsili, and F. Giammanco, Phys. Stat. Sol. (a) 204, No. 6, 1693-1698 (2007)
- *Multiphoton fragmentation of PAMAM G5-capped-gold-nanoparticles induced by picosecond laser irradiation at 532nm*, Anna Giusti, Emilia Giorgetti, **Simona C. Laza**, Paolo Marsili, Francesco Giammanco, J. Phys. Chem. - in press
- *Photo degradation of PAMAM G5 stabilized aqueous suspensions of gold nanoparticle*s, Emilia Giorgetti, Anna Giusti, Francesco Giammanco, **Simona C. Laza**, Tommaso DelRosso, Giovanna Dellepiane, Appl. Surf. Sci. - accepted

Bibliography

[1] S. Eustis, M.A. El-Sayed, *Chem. Soc. Rev.*, **35**, 209-217 (2006)

[2] M. Faraday, *Philos. Trans. Royal Soc. London*, **147**, 145 (1857)

[3] U. Kreibig, M. Vollmer, *Optical properties of metal clusters*, Springer-Verlag Berlin Heidelberg, 1995

[4] C.F. Bohren, D. R. Huffman, *Absorption and Scattering of Light by Small Particles*, Wiley New York, 1998

[5] G. Mie, *Ann. d. Physik* (4), **25**, 377 (1908)

[6] R. Gans, *Ann. Physik*, **37**, 881 (1912)

[7] K.L. Kelly, E. Coronado, L.L. Zhao, G.C. Schatz, *J. Phys. Chem. B*, **107**, 668-677 (2003)

[8] R. Narayanan, M.A. El-Sayed, *J. Phys. Chem. B*, **109**, 12663-12676 (2005)

[9] M.-C. Daniel, D. Astruc, *Chem. Rev.*, **104**, 293-346 (2004)

[10] A. Fotik, A. Henglein, *Ber. Bunsenges. Phys. Chem.,* **97**, 252 (1993)

[11] A. Henglein, *J. Phys. Chem.* **97**, 5457 (1993)

[12] J. Nendersen, G. Chumanov, T. Cotton, *Appl. Spectrosc.*, **47**, 1959 (1993)

[13] M. Prochazka, J. Stepanek, B. Vlckova, I. Srnova, P. Maly, *J. Mol. Struct.* **410-411**, 213 (1997)

[14] M. Prochazka, P. Mojzes, J. Stepanek, B.Vlckova, P.-Y. Turpin, *Anal. Chem.* **69**, 5103 (1997)

[15] I. Srnova, M. Prochazka, B. Clckova, J. Stepanek, P. Maly, *Langmuir* **14**, 4666 (1998)

[16] T. Tsuji, K. Iryo, Y. Nishimura, M. Tsuji, *J. Photochem. Photobiol. A*, **145,** 201 (2001)

[17] T. Tsuji, K. Iryo, N. Watanabe, M. Tsuji, *Appl. Surf. Sci.* **202,** 80 (2002)

[18] F. Mafune, J. Kohno, Y. Takeda, T. Kondow, H. Sawabe, *J. Phys. Chem. B* **104**, 9111 (2000)

[19] F. Mafune, J.-Y. Kohno, Y. Takeda, T. Kondow, H. Sawabe, *J. Phys. Chem. B,* **105**, 5114 (2001)

[20] F. Mafune, J.-Y. Kohno, Y. Takeda, T. Kondow, H. Sawabe, *J. Phys. Chem. B,* **105**, 9050 (2001)

[21] F. Mafune, J. Kohno, Y. Takeda, T. Kondow, *J. Phys. Chem. B*, **106**, 7575, (2002)

[22] F. Mafune, J.-Y. Kohno, Y. Takeda, T. Kondow, *J. Phys. Chem. B*, **106**, 8555, (2002)

[23] G. Compagnini, A.A. Scalisi, O. Puglisi, *J. Appl. Phys.*, **Vol.94**, No.12, 7874 (2003)

[24] G. Compagnini, A.A. Scalisi, O. Puglisi, *J. Mater. Res.*, **Vol.19**, No.10, 2795 (2004)

[25] V. Amendola, S. Polizzi, M. Meneghetti, *J. Phys. Chem. B*, **110**, 7232-7237 (2006)

[26] V. Amendola, G.A. Rizzi, S. Polizzi, M. Meneghetti, *J. Phys. Chem. B*, **109**, 23125-23128 (2005)

[27] F. Gröhn, B.J. Bauer, Y.A. Akpalu, C.L. Jackson, E.J. Amis, *Macromolecules*, **33**, 6042-6050 (2000)

[28] M. Zhao, L. Sun, R.M. Crooks, *J. Am. Chem. Soc.,* **120**, 4877-4878 (1998)

[29] K. Esumi, A. Suzuki, A. Yamahira, K. Torigoe, *Langmuir*, **16**, 2604 (2000)

[30] K. Hayakawa, T. Yoshimura, K. Esumi, *Langmuir*, **19**, 5517 (2003)

[31] J.Y. Ye, L. Balog, T.B. Norris, *Appl.Phys.Lett.*, **Vol.80**, No.10, 1713 (2002)

[32] A. Bielinska, J.D. Eichman, I. Lee, J.R. Baker Jr, L. Balog, *J. Nanoparticle Research*, **4**, 395 (2002)

[33] http://en.wikipedia.org

[34] D.A. Tomalia, H. Baker, J.R. Dewald, M. Hall, G. Kallos, S. Martin, J. Roeck, J. Ryder, P. Smith, *Polym. J.* **17**, 117-132 (1985)

[35] A.W. Bosman, H.M. Janssen, E.W. Meijer, *Chem. Rev.* **99**, 1665-1688 (1999)

[36] M. Born, E. Wolf, *Principle of optics*, 7-th ed., Cambridge University Press, 2005

[37] P. Debye, *Ann. d. Physik* (4), **30**, 118 (1909)

[38] http://www.philiplaven.com

[39] U. Kreibig, P. Zacharias, *Z. Physik,* **231**, 128 (1970)

[40] U. Kreibig, B. Schmitz, H.D. Brener, *Phy. Rev. B*, **36**, 5027 (1987)

[41] F. Bassani, G.P. Parravicini, *Electronic states and optical transitions in solids*, Pergamon Press London ,1975

[42] R. Fuchs, *Phys. Rev. B*, **11,** 1732 (1975)

[43] T. Guo, P. Nikolaev, A.G. Rinzler, D. Tomanek, D. T. Colbert, R. E. Smalley, *J. Phys Chem.*, **99**, 10694-1069 (1995)

[44] P.R. Willmot, J.R. Huber, *Rew. Mod. Phys.*, **Vol.72**, No.1, 315 (2000)

[45] G. Petite, P. Martin, R.Trainham, P. Agostini, S. Guinzard, F. Jollet, J.P. Duand, *Laser Ablation - Mechanisms and Applications, Proceedings*, Oak Ridge, TN, USA 1991

[46] S. Amoruso, R. Bruzzese, N. Spinelli, R. Velotta, *J. Phys. B: At. Mol. Opt. Phys.* **32**, R131-R172 (1999)

[47] R. Kelly, A. Miotello, *Appl. Surf. Sci.*, **205,** 96-98 (1996)

[48] K.H. Song, X. Xu, *Appl. Surf. Sci.*, **111**,127-129 (1998)

[49] A. Semerok, C. Chaleard, V. Detalle, J.-L. Lacour, P. Mauchien, P. Meynadier, C. Nouvellon, B. Salle, P. Palianov, M. Perdrix, G. Petite, *Appl. Surf. Sci.* **138-139,** 311(1999)

[50] M. Lenzner, J. Krüger, S. Sartania, Z. Cheng, C. Spielmann, G. Mourou, W. Kautek, F. Krausz, *Phys. Rev. Lett.* **80**, 4076 (1998)

[51] D. Sibold, H.M. Urbassek, *Phys. Fluids A,* **4**, 165 (1992)

[52] R. Kelly, A. Miotello, *Appl. Phys. B: Photophys. Laser Chem.* **57** (1993)

[53] M.J. Shea, R.N. Compton, *Laser Ablation - Mechanisms and Applications, Proceedings*, Oak Ridge, TN, USA 1991

[54] S.I. Dolgaev, A.V. Simakin, V.V. Voronov, G.A. Shafeev, F. Bozon-Verduraz, *Appl. Surf. Sci.*, **186**, 546 (2002)

[55] A.V. Simakin, V.V. Voronov, G.A. Shafeev, R. Brayner, F. Bozon-Verduraz, *Chem. Phys. Lett.*, **348**,182 (2001)

[56] J.F. Ready, D.F. Farson, Eds: *LIA Handbook of Laser Material Processing*, Springer, Heidelberg 2001

[57] D.B. Geohegan, A.A. Puretzky, G. Duscher, S.J. Pennycook, *Appl. Phys. Lett.* **72**, 2987 (1998)

[58] J.-P. Sylvestre, A.V. Kabashin, E. Sacher, M. Meunier, *Appl. Phys. A*, **80**,753 (2005)

[59] A. Vogel, J. Noack, K. Nohen, D. Theisen, S. Busch, U. Porlitz, D.X. Hammer, G.D. Noojin, B.A. Rockwell, R. Birngruber, *Appl. Phys. B* **68**, 271, (1999)

[60] A.V. Kabashin, M. Meunier, *J. Appl. Phys.*, **Vol.94**, No.12, 7941 (2003)

[61] S.M. Klimentov, T.V. Kononenko, P.A. Pivovarov, S.V. Garnov, V.I. Konov, A.M. Prokhorov, D. Breitling, F. Dausingerb, *Quantum Electron.* **31**, 378 (2001)

[62] S. Linkl, M.A. El-Sayed, *J. Phys. Chem. B* **103**, 8410 (1999)

[63] J.L. Gardea-Torresdey, J.G. Parson, E. Gomez, J. Peralta-Videa, H. Troiani, P. Santiago, M. Jose-Yacaman, *Formation and growth of Au nanoparticles inside live Alfaalfa plants*, NanoLetters **2**, 397 (2002)

[64] J. Chandle, T. Gurmin, N. Robinson, *IVD Technology*, **37**, March-April (2000)

[65] J.W. Mullin, *Crystalization*, Butterworth, London, 2001

[66] V.K. La Mer, *J. Phys. and Colloidd Chem.* **52**, 65 (1948)

[67] V.K. La Mer, Wilson, *J. Ind. Hyg. and Toxicol.* **30**, 265 (1948)

[68] H. Reiss, *J. Chem. Phys.* **Vol.19**, No 4, 482 (1951)

[69] O. Sonhnel, J. Garside, *Precipitation*, Butterworth, London, 1992

[70] N.V. Tarasenko, A.V. Butsen, E.A. Nevar, N.A. Savastenko, *Appl. Surf. Sci.,* **252,** 4439 (2006)

[71] Y.-H. Chen, C.-S. Yeh, *Colloids Surf.* **197**, 133 (2002)

[72] T. Tsuji, T. Kakita, M. Tsuji, *Appl. Surf. Sci.* **206**, 314 (2003)

[73] A.V. Kabashin, M. Meunier, C. Kingston, J.H.T. Luong, *J. Phys. Chem. B* **107**, 4527 (2003)

[74] F. Mafune, J.-Y. Kohno, Y. Takeda, T. Kondow, *J. Phys. Chem. B* **107**, 4218 (2003)

[75] F. Mafune, J.-Y. Kohno, Y. Takeda, T. Kondow, *J. Phys. Chem. B* **104**, 8333 (2000)

[76] K. Esumi, A. Suzuki, N. Aihara, K. Usui, K. Torigoe, *Langmuir*, **14**, 3157 (1998)

[77] M. Zhao, R.M. Crooks, *Agew. Chem. Int. Ed.*, **38**, 364 (1999)

[78] K. Esumi, *Top. Curr. Chem.* **227**, 31-52 (2003)

[79] W. Hoheisel, M. Vollmer, F. Trager, *Laser Ablation - Mechanisms and Applications*, Proceedings, Oak Ridge, TN, USA 1991

[80] S. Link, M.A. El-Sayed, *Rev. Phys. Chem.*, **19**, 409-453 (2000)

[81] S. Link, M.A. El-Sayed, *J. Phys. Chem. B*, **103**, 8410-8426 (1999)

[82] S. Link, C. Burda, B. Nikoobakht, M.A. El-Sayed, *J. Phys. Chem. B*, **104**, 6152-6163 (2000)

[83] S. Link, Z.L. Wang, M.A. El-Sayed, *J. Phys. Chem. B*, **104,** 7867- 7870 (2000)

[84] P.V. Kamat, M. Fulmiani, G.V. Hartland, *J. Phys. Chem. B*, **102**, 3123-3128 (1998)

[85] J.-P. Sylvestre, A.V. Kabashin, E. Sacher, M. Meunier, J.H.T. Luong, *J.Am.Chem.Soc.* **126**, 7176 (2004)

[86] A.V. Kabashin, M. Meunier, *J.Photochem. Photobiol. A: Chemistry,* **182**, 330-334 (2006)

[87] Y.H. Yoo, S.H. Joeng, R. Greif, R.E. Russo, *J. Appl. Phys.* **88**, 1638 (2000)

[88] T. Tsuji, Y. Tsuboi, N. Kitamura, M. Tsuji, *Appl. Surf. Sci.* **229**, 365-371 (2004)

[89] M. Quinten, *Doctor Thesis*, Saarbrücken, (1989)

[90] H. Eckstein, U. Kreibig, *Z. Phys. D*, 26, 239-241 (1993)

[91] K. Kimura, *J. Phys. Chem.*, **98**, 11997-12002 (1994)

[92] Y. Takeuchi, T. Ida, K. Kimura, *J. Phys. Chem. B*, 101, 1322-1327 (1997)

[93] R.P. Sperline, Y. Song, H. Freiser, *Langmuir*, **13**(14), 3727-3732 (1997)

[94] L. Balogh, R. Valluzzi, K.S. Laverdure, S.P. Gido, G.L. Hagnauer, D.A. Tomalia, *J. Nanoparticle Research ,* **1**, 353 (1999)

[95] E. Giorgetti, A. Giusti, S.C. Laza, P. Marsili, F. Giammanco, *Phys. Stat. Sol. A*, **204**, No. 6, 1693-1698 (2007)

[96] E. Giorgetti, A. Giusti, F. Giammanco, S.C. Laza, T. DelRosso, G. Dellepiane, *Appl. Surf. Sci.* (accepted)

[97] A. Giusti, E. Giorgetti, S. Laza, P. Marsili, F. Giammanco, *J.Phys.Chem C* (in press)

[98] J.K. Gibson, *Vac. Sci. Technol. A*, 16,653 (1998)

[99] IUPAC Compendium of Chemical Terminology , **67**, 132 (1995)

[100] F. Hache, D. Ricard, C. Flytzanis, U. Kreibig, *Appl. Phys. A*, **47**, 347 (1988)

[101] V. Amendola, G.A.Rizzi, S. Polizzi, M. Meneghetti, *J. Phys. Chem. B*, **109**, 23125-23128 (2005)

[102] M.M. Alvarez, J.T. Khoury, T.G. Schaff, M.N. Shafigullin, I. Vezmar, R. Whetten, *J. Phys. Chem. B*, 101, 3706-3712 (1997)

[103] K. Subramanya Mayya, F. Caruso, *Langmuir*, **19** (17), 6987-6993 (2003)

[104] G. Compagnini, A.A. Scalisi, O. Puglis, *Phys. Chem. Chem. Phys.*, **4**, 2787-2791 (2002)

[105] T. Mortier, T. Verbiest, A. Persoons, *Chem. Phys. Lett.*, Vol.**382**, Issues 5-6, 650-653 (2003)

[106] U. Kreibig, L. Genzel, *Surf. Sci.* **156**, 67 (1985)